

# **DYNAMIC CRUSHING BEHAVIOUR OF CACTUS GEOMETRY INSPIRED CORE STRUCTURE**

**A Thesis Submitted to  
the Graduate School of Engineering and Sciences of  
İzmir Institute of Technology  
in Partial Fulfillment of the Requirements for the Degree of**

**MASTER OF SCIENCE**

**in Mechanical Engineering**

**by  
Ozan BALYA**

**December 2019**

**İZMİR**

## ACKNOWLEDGMENTS

I would like to thank my supervisor Prof. Alper TAŞDEMİRÇİ for his inspiring guidance and encouraging approach during the thesis study. Moreover, my supervisor Prof. Alper TAŞDEMİRÇİ and co-supervisor Prof. Mustafa GÜDEN supervised me to take excessive information acquisition about mechanical behavior and properties of materials via their academic studies and guidances. I would like to especially thank some lecturers; Prof. Dr. Sedat AKKURT, Assoc. Prof. Hatice Seçil ARTEM and Assoc. Prof. Erdal ÇETKİN for their scientific contributions to my educational process in the master of science degree.

Additionally, for their emphatic supports and helps, I own the team of Dynamic Test and Modelling Laboratory a debt of gratitude: Mesut BAYHAN, Semih Berk SEVEN, Ayda RAMYAR, Berika YORULMAZLAR, Muhammet ÇELİK, Mustafa Kemal SARIKAYA, and Burak AKYOL.

Finally, I would like to dedicate enormous gratefulness to my parents' presence due to my all life's material aid and spiritual support.

# ABSTRACT

## DYNAMIC CRUSHING BEHAVIOUR OF CACTUS GEOMETRY INSPIRED CORE STRUCTURE

Cactus geometry inspired core structure was manufactured with the fused deposition modelling method by a 3D printer using Acrylonitrile Butadiene Styrene (ABS) material filament. The characterization of ABS was made by performing compression tests to take some parameters for numerical models. Numerical preliminary studies were carried out by using the areal density concept and direct-impact Hopkinson pressure bar test method to compare the cactus geometry with the conventional ones in point of the specific energy absorption capacity (SEA). It was understood that from the preliminary work, the cactus inspired structure is intriguing to investigate the dynamic crushing behaviour at least. Quasi-static, drop weight and direct-impact Hopkinson pressure bar tests were conducted to comprehend the energy absorption and crushing behavior in all cases, then to investigate the strain rate and inertia effects on the structure. Implicit and explicit numerical models were made by using LS-DYNA software to validate experiments and to set a precedent for future works. It was seen that the result of numerical models is in harmony with that of experiments excluding the non-fracture structure at the quasi-static implicit model. Moreover, although quasi-static compression gave the structure more stable deformation behavior compared to drop weight impact, higher energy absorption capability was observed on drop-weight tests. In addition, the strain rate effect is more forceful in point of loading carrying capacity compared to the inertia effect despite the fact that it provides the development of buckling and damage formation.

## ÖZET

### KAKTÜS GEOMETRİSİNDEN ESİNLENİLMİŞ ÇEKİRDEK YAPININ DİNAMİK EZİLME DAVRANIŞI

Kaktüs geometrisinden esinlenilmiş çekirdek yapı, Akrilonitril Bütadien Stiren (ABS) malzeme filamentini kullanılarak 3 boyutlu yazıcı vasıtasıyla birleştirmeli yığma modelleme metodu ile üretildi. ABS, nümerik modeller için bazı parametreleri elde etmek amacıyla basma testleri gerçekleştirilerek karakterize edildi. Nümerik ön çalışmalar, spesifik enerji emilim kapasitesi bakımından kaktüs geometriyi geleneksel olanlarla kıyaslamak amacıyla alansal yoğunluk kavramı ve Hopkinson doğrudan darbeli basınç bar testlerini kullanarak yürütüldü. Ön çalışmadan, kaktüsten ilham alan yapının en azından dinamik ezilme davranışının incelenmesi amacıyla ilgi çekici olduğu anlaşıldı. Yarı-statik, düşen ağırlık ve Hopkinson doğrudan darbeli basınç bar testleri, tüm durumlarda ezilme davranışını ve enerji emilimini kavramak ve daha sonra yapı üzerinde şekil değiştirme hızı ve atalet etkilerini incelemek amacıyla yapılmıştır. Örtük ve açık sayısal modeller, deneyleri doğrulamak ve gelecek çalışmalar için bir emsal oluşturmak için LS-DYNA yazılımı kullanılarak yapılmıştır. Nümerik modellerin sonucunun, yarı-statik modelde kırılmayan yapı hariç deneyler ile uyum içinde olduğu görülmüştür. Ayrıca, yarı-statik basma yapıya, düşen ağırlık darbesine kıyasla daha kararlı bir deformasyon davranışı vermesine rağmen, düşen ağırlık testlerinde daha yüksek enerji emme kabiliyeti gözlenmiştir. Ek olarak, gerilme hızı etkisinin, burkulma ve hasar oluşumunun gelişmesini sağlamasına rağmen atalet etkisine kıyasla yükleme taşıma kapasitesi açısından daha etkin olduğu görülmüştür.

# TABLE OF CONTENT

LIST OF FIGURES .....	viii
LIST OF TABLES.....	xiii
CHAPTER 1. INTRODUCTION .....	1
1.1. Introduction .....	1
1.2. Literature Survey.....	7
1.3. Preliminary Work.....	30
1.4. Aim and Scope of the Study.....	37
CHAPTER 2. MANUFACTURING AND EXPERIMENTAL.....	39
2.1. Materials and Manufacturing .....	39
2.2. Experimental Details .....	41
2.2.1. Material Characterization and Model Selection of ABS .....	41
2.2.2. Quasi-Static Compression Experiments .....	50
2.2.3. Drop Weight Impact Experiments .....	52
2.2.4. Direct Impact Hopkinson Pressure Bar Experiments .....	53
CHAPTER 3. NUMERICAL STUDIES .....	55
3.1. Crushing Modelling of Cactus Geometry Inspired Core .....	55
3.1.1. Quasi-Static Modelling (Implicit).....	56
3.1.2. Dynamic Impact Modelling (Explicit).....	56
CHAPTER 4. RESULTS AND DISCUSSIONS .....	58
4.1. Crushing Behaviour and Energy Absorption of Cactus Geometry Inspired Structure .....	58
4.2. Inertia Effect and Strain Rate Sensitivity.....	67

CHAPTER 5. CONCLUSIONS .....	74
REFERENCES.....	82

# LIST OF FIGURES

<b><u>Figure</u></b>	<b><u>Page</u></b>
Figure 1.1. Acceleration and pressure measurement set-up for different human body regions.....	2
Figure 1.2. Fused Deposition Modelling Method.....	3
Figure 1.3. The chemical structure of ABS polymer and its monomers .....	4
Figure 1.4. Famous bio-inspired inventions (a) Sunshades on the exterior of the new Minister of Municipal Affairs and Agriculture office (MMAA) in Qatar, (b) The head of the Shinkansen Bullet train, (c) Naval underwater sensors, (d) Boats, Hospitals Don Sharkskin .....	6
Figure 1.5. Crushing force-displacement curve of a typical cruciform structure.....	7
Figure 1.6. Analytical models of crushing cruciforms .....	8
Figure 1.7. The top view of the chiral honeycomb.....	8
Figure 1.8. Buckling modes of the chiral honeycomb for (a) the FEA and (b) experiment.....	9
Figure 1.9. Illustration of (a) semi-hexagonal structure, (b) unidirectional fabric, (c) plain woven fabric, and (d) orthogonal woven fabric .....	10
Figure 1.10. Profiles of tapered tubular structures.....	11
Figure 1.11. HHHs with different orders.....	12
Figure 1.12. Force-strain curves of HHHs with different orders.....	13
Figure 1.13. The sectional view of three different structures: (a) honeycomb structure, (b) <i>C. septempunctata</i> ladybeetle inspired bionic honeycomb-tubular structure (BHTS-1), (c) <i>A. dichotoma</i> beetle inspired bionic honeycomb-tubular structure (BHTS-2).....	13
Figure 1.14. (a) Crushing force-displacement curves of bionic honeycombs, (b) Energy absorption-displacement curves of bionic honeycombs .....	14
Figure 1.15. The collapse modes of multi-cell tubes.....	15
Figure 1.16. The pareto curve of the O-BMCT-6 structure.....	15
Figure 1.17. (a) Woodpecker beak, (b) the sectional view of lower and upper beak, (c) the TEM image of the keratin texture, (d) curvy honeycomb structure, (e) the enlargement image of curvy structure, (f) bio-inspired honeycomb core.....	16

<b><u>Figure</u></b>	<b><u>Page</u></b>
Figure 1.18. (a) Collapse modes of honeycomb sandwich panels (b) Collapse modes at crushing strain of 16% .....	17
Figure 1.19. (a) The unit cell measurements, (b) the design with transverse compression direction, and (c) the design with ribbon compression direction.....	18
Figure 1.20. Efficiency-stress curves of cellular structures made of (a) NinjaFlex, (b) SemiFlex compressed in the ribbon direction, and specimens made of (c) NinjaFlex, (d) SemiFlex compressed in the transverse direction .....	18
Figure 1.21. Specific energy-stress distribution of structures made of (a) NinjaFlex and (b) SemiFlex at different strain rates .....	19
Figure 1.22. (a) Illustrations of filling patterns, and (b) the specimen cross-section exposed to compression .....	19
Figure 1.23. (a) Specific compressive strength and, (b) specific stiffness values of the ABS printed structures.....	20
Figure 1.24. Comparisons of (a) compressive Young's modulus, and (b) compressive strength values varying with printing time per specimen for different samples with a filler percentage of 20,30 and 40%.....	20
Figure 1.25. Sandwich panels consisted of repeating diferent cellular cores .....	21
Figure 1.26. The comparison of the experimental and numerical results of sandwich panels which consisted of alternative core configurations, cell topologies, and cell relative densities in terms of energy absorption.....	22
Figure 1.27. (a) Normalized stress-strain curves, (b) specific stiffness, and (c) energy absorption histograms of regular and hierarchical honeycombs ....	23
Figure 1.28. (a) Aluminium tubes and ABS poly-cell insets and (b) composite structure .....	23
Figure 1.29. (a) The lattice sandwich structure, (b) the triangular cellular core structure and, (c) the hexagonal cellular core structure .....	24

<b><u>Figure</u></b>	<b><u>Page</u></b>
Figure 1.30. (a) The illustration of the boundary conditions of the cellular structure subjected to compression in the numerical analysis, and honeycomb models using different kinds of elements: (b) shells, (c) bricks and (d) beams with varying element sizes .....	25
Figure 1.31. Models with different cellular structures: (a) honeycomb, (b) modified honeycomb, and (c) spiral.....	25
Figure 1.32. First failure locations: (a) FEA and (b) experiment images of the BCC structure, (c) FEA and (d) experiment images of the BCCG structure, (e) FEA and (f) experiment images of the BCCA structure, (g) FEA and (h) experiment images of the BCCV structure .....	26
Figure 1.33. Deformation steps of (a) Type I and (b) Type II structures .....	27
Figure 1.34. (a) The temperature change dependent on varying plastic strain and strain rate, (b) the proportion of flow stress to deformation temperature based on the varying plastic strain and strain rate .....	28
Figure 1.35. Deformed specimens at different strain rates .....	29
Figure 1.36. Fractography images of all ABS and ABSplus specimens .....	30
Figure 1.37. The cactus and bio-inspired core structure.....	31
Figure 1.38. Cactus and other conventional geometry designs for the first method .....	32
Figure 1.39. Deformation behaviour of (a) cactus, (b) hexagon, (c) cylinder, and (d) square designed structures of the first concept subjected to direct impact pressure .....	33
Figure 1.40. (a) Force-displacement, and (b) specific energy absorption comparison results of structures having different diagonal lengths.....	33
Figure 1.41. Cactus and other conventional geometry designs for the second method.....	35
Figure 1.42. Deformation behaviour of (a) cactus, (b) hexagon, (c) cylinder, and (d) square designed structures of the second concept subjected to direct impact pressure .....	35
Figure 1.43. (a) Force-displacement, and (b) specific energy absorption comparison results of structures having same diagonal length.....	36
Figure 2.1. Technical drawing of the cactus geometry inspired core .....	39
Figure 2.2. Stratasys uPrint SE 3D printer.....	40

<b><u>Figure</u></b>	<b><u>Page</u></b>
Figure 2.3. (a) The cactus geometry inspired core and (b) the characterization specimen with support on the print bed .....	41
Figure 2.4. (a) Compression and (b) tension test specimens .....	41
Figure 2.5. Shimadzu universal testing machine with compression apparatus .....	42
Figure 2.6. Shimadzu universal testing machine with tension apparatus .....	42
Figure 2.7. Split-Hopkinson pressure bar .....	43
Figure 2.8. An example of the voltage-time history for ABS polymer .....	44
Figure 2.9. True stress – true strain curves of quasi-static compression characterization tests.....	45
Figure 2.10. True stress – true strain curves of SHPB characterization tests .....	45
Figure 2.11. Determination of C and P parameters .....	48
Figure 2.12. The true plastic stress-strain curve of ABS specimen under quasi-static compression at the strain rate of $10^{-1} \text{ s}^{-1}$ .....	49
Figure 2.13. True stress – true plastic strain curves of quasi-static tensile tests .....	50
Figure 2.14. Quasi-static experimental set-up .....	51
Figure 2.15. Fractovis drop-weight test set-up .....	52
Figure 2.16. The illustration of direct impact Hopkinson bar experimental set-up.....	53
Figure 2.17. Voltage – time curve for ABS cactus geometry inspired core after direct impact Hopkinson bar test .....	54
Figure 3.1. Crushing model of the cactus geometry inspired core .....	55
Figure 3.2. Direct impact model of the cactus geometry inspired core .....	56
Figure 4.1. Experimental force-displacement curves of cactus geometry inspired core; (a) $10^{-1} \text{ s}^{-1}$ , (b) $10^{-2} \text{ s}^{-1}$ , (c) $10^{-3} \text{ s}^{-1}$ , and (d) the comparison of some tests at different strain rates.....	58
Figure 4.2. Experimental and numerical force-displacement curves of the cactus geometry inspired core at quasi-static compression test at the strain rate of $0.1 \text{ s}^{-1}$ .....	60
Figure 4.3. Crushing modes of cactus geometry inspired core for both numerical analysis and experimental quasi-static compression tests at deformation values of (a) 0 mm, (b) 1.25 mm, (c) 3mm, (d) 6mm, (e) 9mm, and (f)12mm .....	61

<b><u>Figure</u></b>	<b><u>Page</u></b>
Figure 4.4. Experimental and numerical force-displacement curves of the cactus geometry inspired core at the drop weight impact test with the striker velocity of 5 m/s.....	63
Figure 4.5. Crushing modes of cactus geometry inspired core for both numerical analysis and experimental drop-weight test at deformation values of (a) 0 mm, (b) 1.43 mm, (c) 4.74 mm, (d) 7.44 mm, (e) 12.38 mm, and (f) 16 mm .....	63
Figure 4.6. Experimental and numerical force-displacement curves of the cactus geometry core at the direct impact test with the impact velocity of 10.71 m/s .....	65
Figure 4.7. Crushing modes of cactus geometry core for both numerical analysis and experimental direct impact test at deformation values of (a) 0 mm, (b) 1.2 mm, (c) 1.75 mm, (d) 2.85 mm, (e) 3.65 mm .....	65
Figure 4.8. The force-displacement curves and deformation modes at certain points for direct impact and quasi-static compression tests .....	67
Figure 4.9. Force-displacement curves of strain rate sensitive models having different impact velocities.....	68
Figure 4.10. Energy absorption-displacement curves of strain rate sensitive models having different impact velocities .....	68
Figure 4.11. Deformation behaviour of cactus geometry inspired core subjected to different impact velocities of (a) 5 m/s, (b) 10 m/s, (c) 15 m/s, (d) 20 m/s, and (e) 25 m/s .....	69
Figure 4.12. Images of numerically deformed cores under different impact velocities of (a) 5 m/s, (b) 10 m/s, (c) 15 m/s, (d) 20 m/s, (e) 25 m/s.....	70
Figure 4.13. The MCF-displacement curves of strain rate active, inactive models and quasi-static test.....	71
Figure 4.14. The percentage effect ratio-displacement curves of strain rate and inertia.....	72
Figure 4.15. Deformation behaviour of cactus geometry inspired core subjected to (a) quasi-static compression test, (b) strain rate inactive direct impact model, and (c) strain rate active direct impact model .....	73

## LIST OF TABLES

<b><u>Table</u></b>	<b><u>Page</u></b>
Table 1.1. Some measurements of core structures for the first method.....	31
Table 1.2. Details of core structures for the second method.....	34
Table 2.1. Material properties of Vascomax C350 bars .....	43
Table 2.2. The characteristic features of the three common use material models for plastics.....	46
Table 2.3. C and P parameters of ABS material .....	49
Table 2.4. Material Parameters of ABS for numerical model .....	50
Table 4.1. Crashworthiness parameters of the cactus geometry inspired core under different loading conditions.....	67

# CHAPTER 1

## INTRODUCTION

### 1.1. Introduction

Thin-walled structures such as shells, arches, plates, and membranes consist of three-dimensional parts in which one dimension is smaller than other two dimensions. These structures are mainly used in buildings, automobiles, ships and store tanks such as silos due to cost-effectivity and lightness in spite of its poor wall depth. In addition, ease of manufacturing of large variety cross-sections for these structures is one of their abilities. As a matter of fact, the different buckling modes and failures in the structure might be observed in the deformation process. Thin-walled structures having different cross-sections made of metallic and composite materials were investigated in axial loading cases (Baroutaji, Sajjia, and Olabi 2017). In some studies, polymers were used to make foam structures that their load-carrying capacity was investigated.

There are many kinds of studies on the importance of blast mitigation to provide better protection systems for occupants (Bosch et al. 2015, Cheng, Dionne, and Makris 2010, Erdik 2019, Krzystała, Mężyk, and Kciuk 2016). It is seen that the acceleration from the source of blast shock wave seriously damages military crew in the case of an explosion. Acceleration and pressure measurement set-up for different human body regions is displayed to comprehend the blast effect in detail, Figure 1.1. Against the terrorist attacks, the crushable cores covering protection systems of sacrificial cladding solution has recently appeared as a safety demand. The steel plate and a Cymat foam core thought as a sacrificial cladding was investigated using analytical and numerical modelling (Karagiozova, Langdon, and Nurick 2010). Another study was carried out glass/polyester tubes to compare with non-sacrificial structures under blast loading (Van Paepegem et al. 2014). Square dome-shape kirigami structure made of the aluminum sheet was numerically subjected to blast loading to observe the blast mitigation capacity of this sacrificial cladding structure (Li, Chen, and Hao 2018).



Figure 1.1. Acceleration and pressure measurement set-up for different human body regions (Source: Krzystała, Mężyk, and Kciuk 2016)

On the other hand, a thin-walled core structure was fabricated as a sacrificial cladding made of a polymeric material by using additive manufacturing because of its non-linear response and crushable (Rebelo et al. 2019).

Additive manufacturing is a contemporary discipline that constructs three-dimensional (3D) parts via a processor controller. First of all, Alain Le Mahaute obtained the patent right for additive manufacturing in 1984. Although the stereolithography technology introduction by C.W. Hull was popular in the 1980s, the first rapid prototyping machine (RPM) is known to be proposed by 3D System Corporation in 1988. In the following period, a whole range of RPM methods came to existence up till today. The most common rapid prototyping techniques are such as selective laser melting (SLM), stereolithography (SLA), laminated object manufacturing (LOM), and fused deposition modeling (FDM). These manufacturing methods were performed in using both mechanical and biology together to obtain some biomechanical complex structures in earlier (Garcia et al. 2018). The FDM, a layer manufacturing technique, is specially introduced with the occasion of some reasons such as the thermoplastics cost-effectivity, the capability of making complex structures. Moreover, this technique manages to obtain 85% of the molded structure strength for 3D printed parts. On the other hand, the confined accuracy and slow progress because of both the high relative viscosity and unpredictable contraction of plastics are some limited problems. The FDM method is briefly applied as follows. After preparing a geometry design in a computer-aided design (CAD) software,

it is converted to stereolithography (STL) file format to make a 3D printer detects the geometry as a solid part. The part is then printed layer by layer with extruding the semi-liquid material particles from a nozzle to the platform, Figure 1.2.

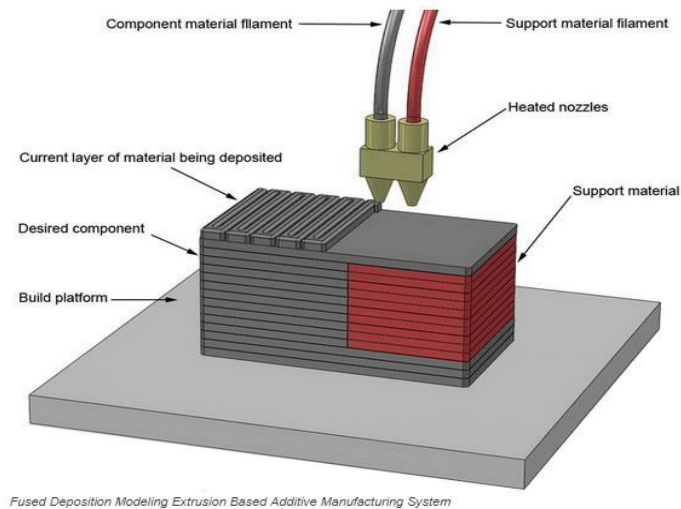


Figure 1.2. Fused Deposition Modelling Method  
(Source: <https://3dprintingearthblog.wordpress.com/author/3dprintingearth/>)

These particles have been usually made of polymeric materials. Both the sample raster angle and building orientation in the process of the FDM have a considerable effect on the mechanical behaviour of the structure. The FDM as one of the additive manufacturing methods influences the mechanical properties of the structure such as tensile, compressive, flexural impact and fatigue strength based on the slicing parameters, building orientations and temperature conditions (Popescu et al. 2018). The current study is conversely performed using constant conditions in the production process, and hence the mechanical characterization change based on the conditions of the production procedure is not the topic. The dynamic crushing behavior and energy absorption of a 3D printed ABS thin-walled structure fabricated based on a constant condition are mainly investigated in this study. The ABS structure composed of three monomers: acrylonitrile, butadiene, and styrene have different roles for the resistance. The chemical structure of these monomers and the ABS polymer are presented in Figure 1.3. While the thermal and chemical support is implemented by acrylonitrile, the machinability and stiffness satisfaction result from styrene. Butadiene, the important monomer for the dynamic

crushing, is the source of impact resistance. Hence, energy absorbing capability of the structure can be investigated in this regard.

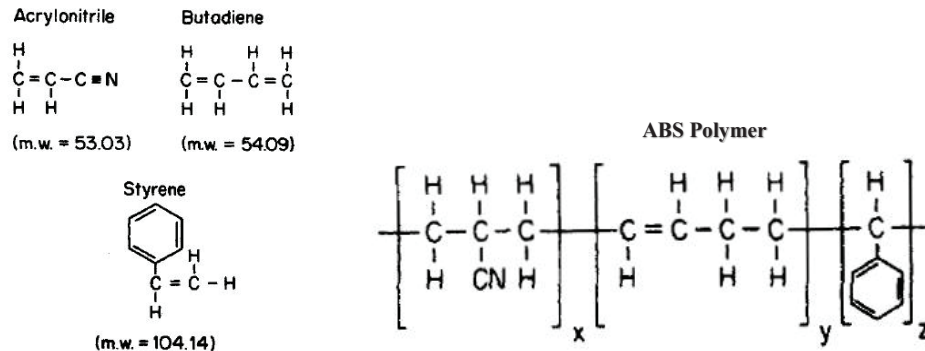


Figure 1.3. The chemical structure of ABS polymer and its monomers (Source: Rutkowski and Levin 1986)

Energy absorbing thin-walled structures are used to protect occupants while transforming a great quantity of kinematic energy to permanent deformation under compression in crash cases. These structures are generally classified in five subheadings: vehicle crashworthiness, road security, guarding against engineering accidents, individual safety, and packaging. When the crashworthiness design of the vehicle is increased, less destruction occurs for both the vehicle and passengers.

Meanwhile, safety barriers components consisted of energy absorbing structures are improved to reduce the traffic road accident risks resulting in injuries and deaths. Moreover, some machines are designed to protect workers from falling objects in dangerous working zones. Bicycle helmets and hard hats as personal safety items also necessitate high energy-absorption ability.

On the other hand, these fields require less cost, higher strength and lower weight structures. The demand has been satisfied with complex and porous core structures produced by additive manufacturing methods recently. Thin-walled structural cores were considered as especially metal and composite materials in the literature reviews because of high energy absorption capacity. However, polymeric materials are lighter relatively compared to metals, the crashworthiness investigation of polymeric structures was initiated in research papers (Tsouknidas et al. 2016).

The brittleness of polymers specially remarks on the importance of the peak impact strength investigation of a structure. A less amount of energy absorption activity is expected, not an efficient property compared to metallic and composite materials. The impact resistance period until a polymeric structure failure might be nevertheless used to prevent the reflected kinetic energy to passengers in armoured vehicles ground footpad systems.

In the current study, the 3D printed ABS thin-walled structure with a novel cross-sectional geometry biologically inspired from the cactus pattern was designed to understand the specific energy absorption capacity.

Bio-inspiration is the mimicking of the geometry, function or behaviour of the living nature objects. The idea under this comes from nature. Some organisms, resisting natural restrictions such as scarcity, disasters or daily challenges appearing like simple tasks, is the inspiration source for the community developed advanced technologies and innovational designs.

When the biological inspiration is examined, the architectural applications of the ancient Egyptian civilization inspired by the lotus plant and the head of the Roman Corinthian column inspired by the acanthus plant, are important anterior proofs of the human and biological inspiration relation (Aziz and El sherif 2016). It is claimed that Otto Schmitt firstly used this modern scientific method for his doctoral research to develop a device by mimicking the nervous system in 1957 (Vincent et al. 2006). He then evaluated this kind of researches within the scope of the term “biomimetic” in an article (Schmitt 1969). Meanwhile, Major Jack E. Steele claimed to discover the term “bionics” in 1958, however, it is formally accepted that thirty participants mentioned bionics in a conference where various scientific people having different branches stood in Dayton, Ohio of 1960 (Roth 1983).

There are different kinds of studies on bio-inspiration beyond the earlier referred researches in recent years. For example, the building design inspired by the cactus structure is presented in Figure 1.4.a. In Qatar's well-known hot and arid climate, the modernized building sunshades were designed inspired by the cactus spines. While the newly designed building explicitly made its employees stay motivated, the other classics wanted for complex and expensive air-conditioner systems. Another instance, it is seen that the head of the Shinkansen bullet train was discovered by mimicking by a Kingfisher bird beak, Figure 1.4.b. Because of the train high speed, atmospheric pressure waves had

created a loud noise at the end of the tunnel and hence they designed the bullet head of the train to prevent the disastrous roaring. Consequently, they managed to reduce the noise using this type of bio-inspired head model. In another study, naval underwater sensors were developed on the basis of the communication systems of dolphins and whales, Figure 1.4.c. The invention made possible to determine the tsunami wave frequency and the ships' direction on their routes. NASA researchers then found out the drag-reducing riblets while imitating the unique shark skin covered with denticles that help reduce drag in another interesting study, Figure 1.4.d. These were used on the hull of the sailboat Stars & Stripes, which won an Olympic Medal. Furthermore, this technology is used to make surface material for hospitals, restaurants and public bathrooms to repel bacteria.

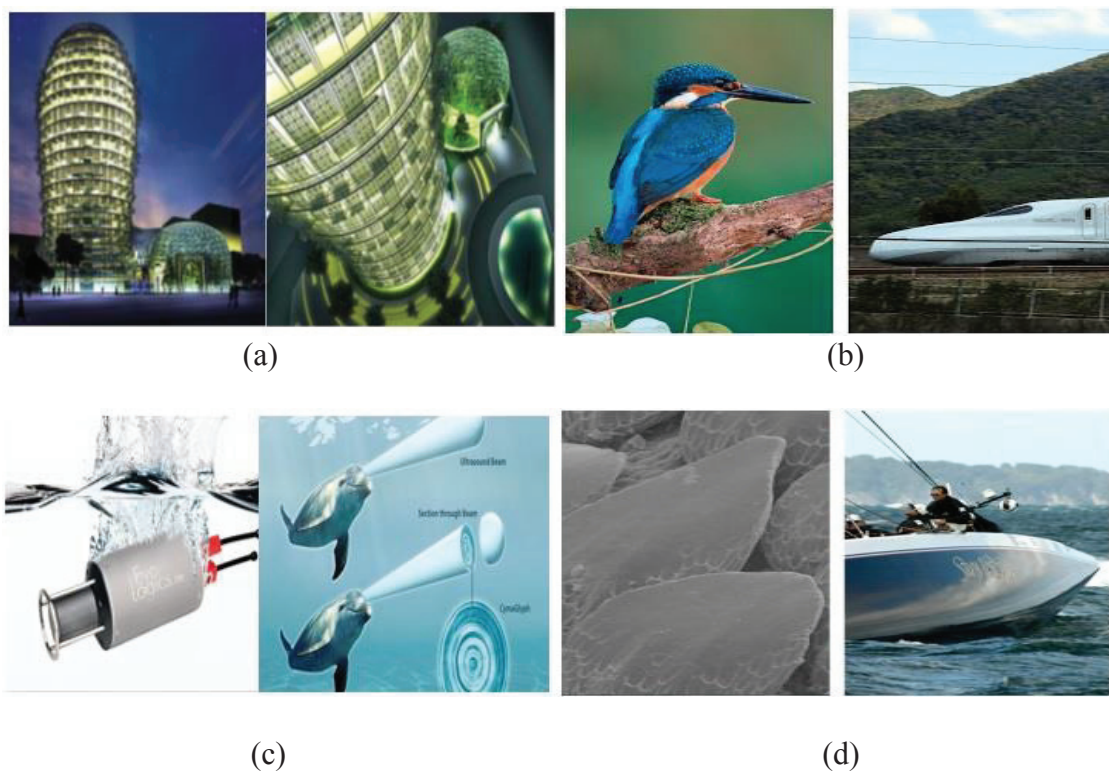


Figure 1.4. Famous bio-inspired inventions (a) Sunshades on the exterior of the new Minister of Municipal Affairs and Agriculture office (MMAA) in Qatar (Source: <https://inhabitat.com/qatar-cactus-office-building/>), (b) The head of the Shinkansen Bullet train (Source: <https://asknature.org/idea/shinkansen-train/>), (c) Naval underwater sensors (Source: <https://asknature.org/idea/evologics-underwater-sensor/#.XKiYNJgzaUk>), (d) Boats, Hospitals Don Sharkskin (Source: <https://www.bloomberg.com/news/photos-essays/2015-02-23/14-smart-inventions-inspired-by-nature-biomimicry>)

Therefore, in the current study, the Acrylonitrile Butadiene Styrene (ABS) thermoplastic polymer thin-walled structure was chosen to investigate the mechanical behaviour, and the additive manufacturing method was preferred to provide cost-effective easy-way-fabrication. The cactus geometry was also preferred to investigate the effect on the crushing behaviour of the structure. Although the structure is columnar, it includes the complex cross-sectional area that is different from conventional tubes such as square, cylinder, triangle or hexagonal sections.

## 1.2. Literature Survey

Energy absorption and deformation mode are significantly affected by the geometrical configuration of a thin-walled structure. The effect of cross-section on the energy absorption capability and deformation mode were firstly investigated in terms of some geometrical parameters such as the profile of the structure and the number of the corner. R. J. Hayduk and T. Wierzbicki investigated the crushing modes of the L-shaped and cruciform structures to understand the effect on the energy absorption process of some geometrical parameters. These structures were manufactured by welding copper sheets. Quasi-static compression tests were made with a velocity of 0.21 mm/s using The Baldwin Testing Machine. It was observed that there is a typical crushing load-displacement behaviour for cruciform structures, Figure 1.5. The structure critical peak force points out the first buckling evolution. It is seen that the first fold formation occurs at the maximum peak force point of the structure. Subsequent fold formations then increase the structure resistance again.

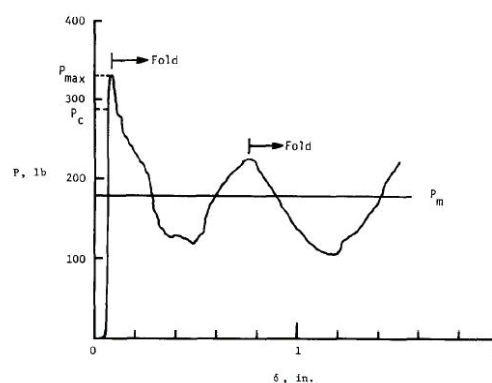


Figure 1.5. Crushing force-displacement curve of a typical cruciform structure (Source: Hayduk and Wierzbicki 1984)

Some combinations of analytical crushing modes such as Mode I/II and Mode I/I which include extensional crushing behaviour were broadly observed during compression tests, Figure 1.6. The extensional mode provides at least 33% of the energy absorption during the deformation process (Hayduk and Wierzbicki 1984).

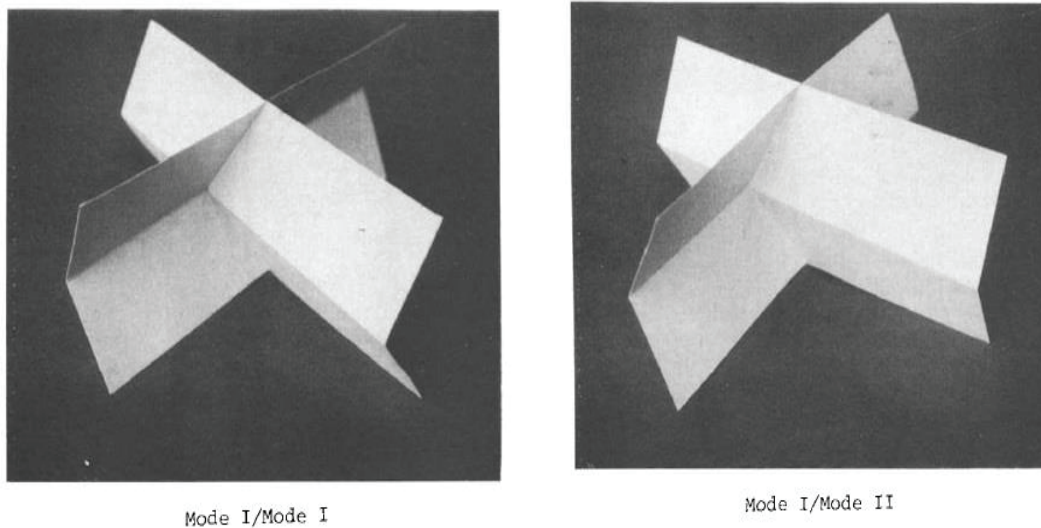


Figure 1.6. Analytical models of crushing cruciforms (Source: Hayduk and Wierzbicki 1984)

F. Scarpa et al. performed compression experiments to understand the contribution to the honeycomb structural strength of both cylinder and ligaments on hexagonal chiral cell honeycombs. The investigated honeycomb type consisted of the junction of circular tangential nodes and straight ligaments, Figure 1.7.

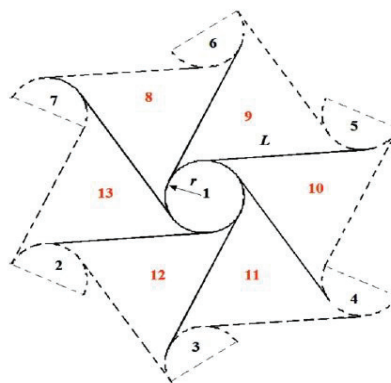
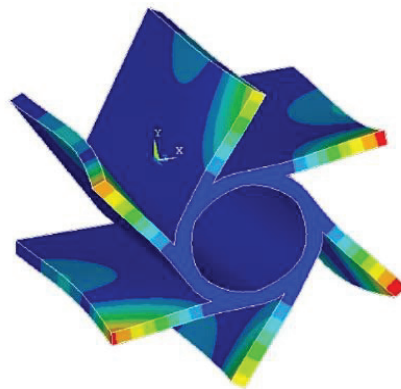
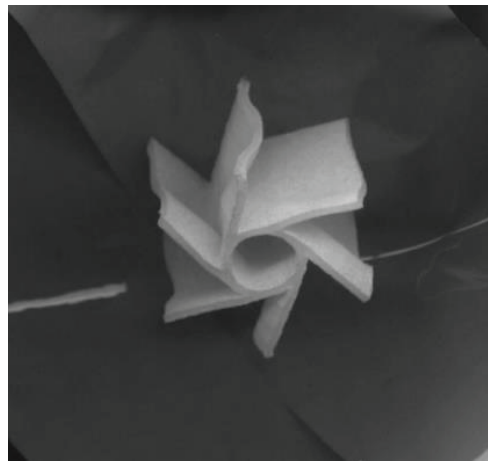


Figure 1.7. The top view of the chiral honeycomb (Source: Scarpa et al. 2007)

In their study, two types of the manufacturing routes: fusion mould deposition and powder stereolithography techniques were used to attain ABS and PA structures respectively. Hexagonal chiral cell honeycomb structures were compressed with a cross-head speed of 0.008 m/s experimentally and numerical analyses were performed to understand the better the behaviour. It was observed that the experiment and numerical analysis deformation mode of the HP-PA powder honeycomb sample have a good correspondance, Figure 1.8.



(a)



(b)

Figure 1.8. Buckling modes of the chiral honeycomb for (a) the FEA and (b) experiment (Source: Scarpa et al. 2007)

It was also detected that the failure formation at the junctions between ligaments and these were also subjected to the flatwise compression. Consequently, although the

cylinder section of the structure supports more compressive load, the ligament section satisfies a partial strength (Scarpa et al. 2007).

The collapse modes of three different types of the semi-hexagonal composite structure were examined by Wu et al. Semi-hexagonal structure and three kinds of woven fabrics profiles are presented in Figure 1.9. These fabrics were manufactured using the 3D orthogonal loom and stacked together with vinyl ester resin to the metal mould to produce semi-hexagonal structures. These were exposed to quasi-static crushing tests with a constant head velocity by a universal testing machine.

Numerical modelling was done to understand the effect of fabrics. Orthogonal woven fabric structures were presented the highest peak force but lowest specific energy absorption capacity with the mode of warp holding and wefts of z-yarns; conversely, unidirectional structures were shown to have the highest specific energy absorption value with the splaying crushing mode of that.

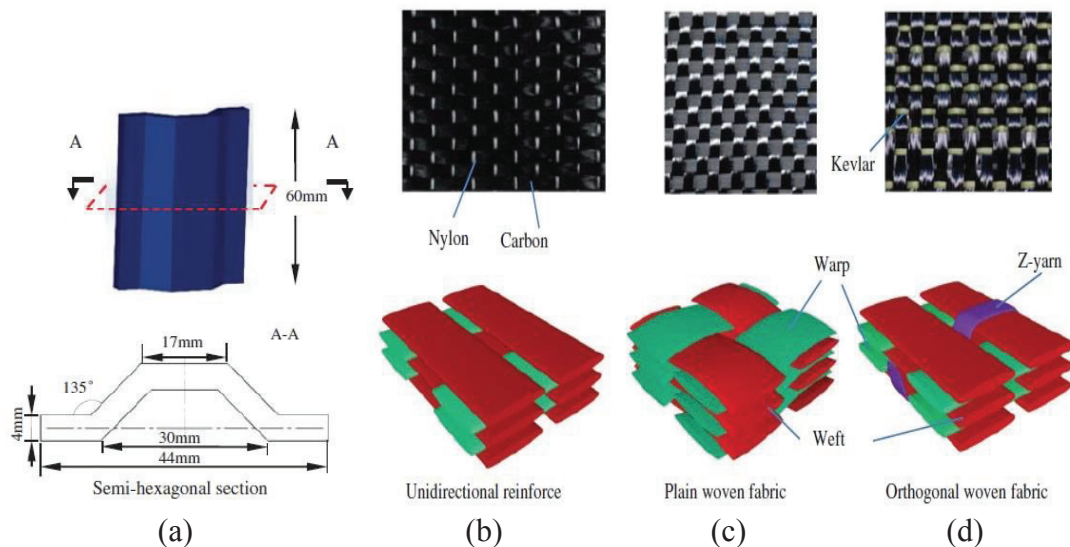


Figure 1.9. Illustration of (a) semi-hexagonal structure, (b) unidirectional fabric, (c) plain woven fabric, and (d) orthogonal woven fabric (Source: Wu et al. 2019)

It was also found that three kinds of crushing behaviours such as splaying mode, buckling mode and mixture mode owing to the fabric reinforcement effect. Furthermore, the structural loading performance of z-yarns was validated with numerical models (Wu et al. 2019).

X. Zhao et al. investigated the crashworthiness of composite tapered tube parameters of cross-section type, tapered angle, and loading angle. Based upon the numerical validation of cylindrical composite structures in drop tests, twenty different tubular structures having five different types of cross-section and four tapered angles were tried in numerical analyses, Figure 1.10. These structures were numerically subjected to compression with a head mass of 320 kg and a striker velocity of 5 m/s at different impact angles ( $0^\circ, 10^\circ, 20^\circ, 30^\circ$ ) until the deformation levels of 70%. The cylindrical tubular structure was found to have the highest energy absorption capability among all of them. All structures excluding the cylindrical one, behaved in favour of the increment of tapered angle in terms of specific energy absorption as the crushing mode of structures became more balanced with that.

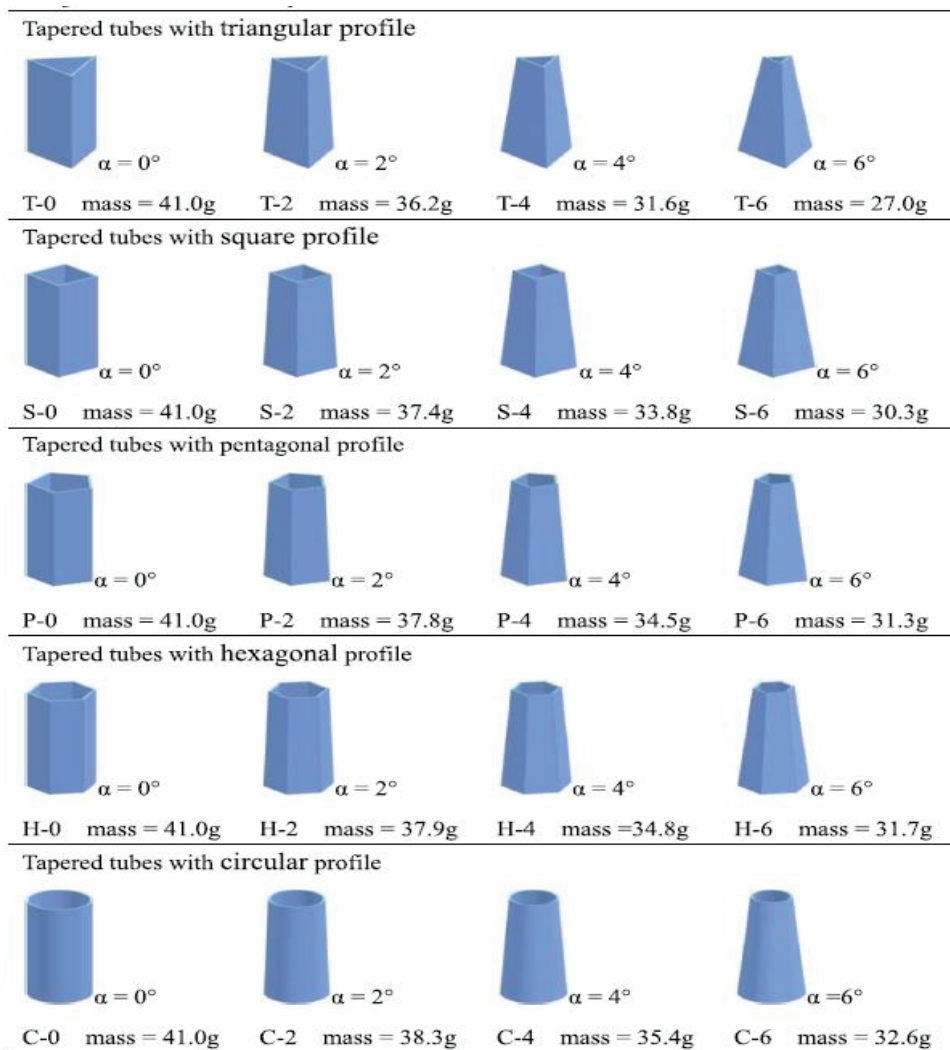


Figure 1.10. Profiles of tapered tubular structures (Source: Zhao et al. 2019)

With the increase of impact angles, all profiles exhibited worse performance in terms of energy absorption. Optimization was performed based on the alteration of fiber orientations and the number of plies. It was found that the hexagonal tubular structure with the taper angle of  $6^\circ$ , 7 layers, and the fiber orientation of  $45^\circ$  is the optimum design with better specific energy absorption capability (Zhao et al. 2019).

Y. Zhang et al. studied energy absorption and crushing behaviour of the bio-inspired systematic hierarchical honeycombs (HHH) with different ordered variations. Materials were exposed to out-of-plane crushing by a striker numerically, Figure 1.11.

It has been revealed that energy absorption capacity increased with the hierarchical order-level enhancement of HHHs. This development creates new bends for each length on the edges. However, non-hierarchical honeycomb forms, which have only the number increment of corners, were not able to attain a good increment in energy absorption. Furthermore, it was noticed that the hierarchization provide to obtain stable load response supporting the crashworthiness, Figure 1.12 (Zhang et al. 2016).

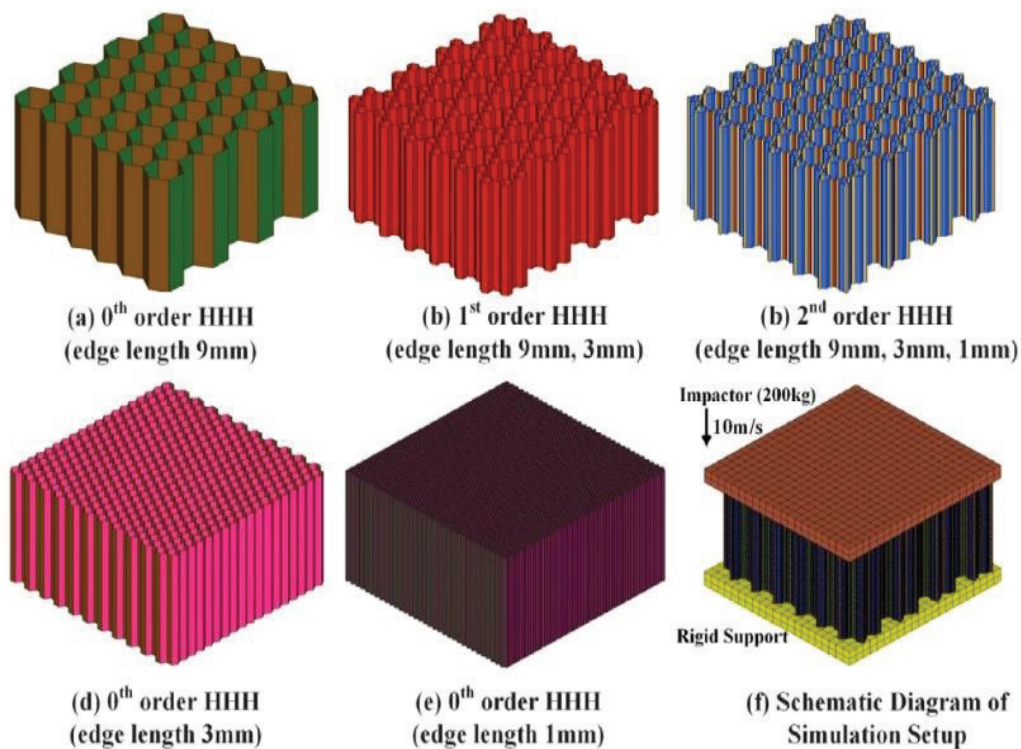


Figure 1.11. HHHs with different orders (Source: Zhang et al. 2016)

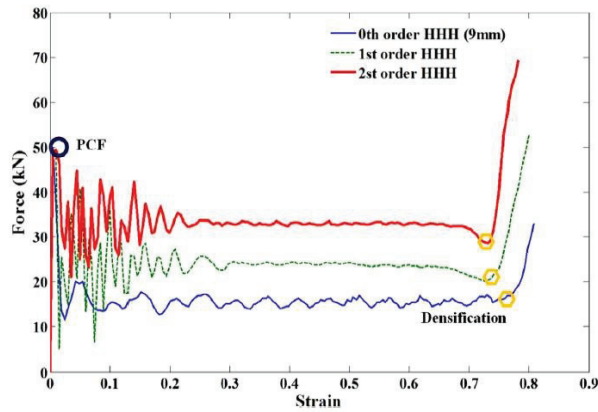


Figure 1.12. Force-strain curves of HHHs with different orders (Source: Zhang et al. 2016)

In a similar way, the biomimetic honeycomb thin-walled structures (BHTSs) were influenced by *C. septempunctata* ladybeetle and *A. dichotoma* beetle external structure, and the energy absorption capacity of the structures under axial dynamic load was numerically researched using a finite element software by Xiang and Du. Two kinds of BHTSs were designed using the software CATIA V5R20 to find out the geometry effect on the energy dissipation capacity, Figure 1.13.

In consequence of numerical analyses, the BHTS-2 has a higher crushing force efficiency than the BHTS-1, therefore the initial peak force of the BHTS-2 is lower than that of the BHTS-1, Figure 1.14.a. The BHTS-2 is a prominent structure in comparison with other configurations in terms of specific energy absorption and crushing force effectiveness, Figure 1.14.b. Furthermore, the increase of the number, thickness, and column diameter affect the specific absorbed energy positively (Xiang and Du 2017).

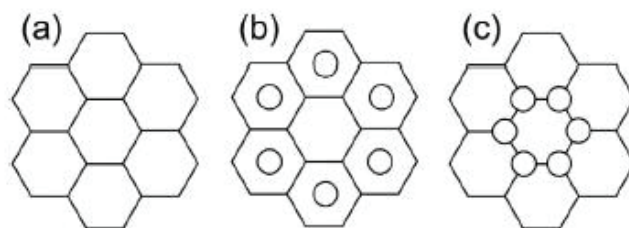


Figure 1.13. The sectional view of three different structures: (a) honeycomb structure, (b) *C. septempunctata* ladybeetle inspired bionic honeycomb-tubular structure (BHTS-1), (c) *A. dichotoma* beetle inspired bionic honeycomb-tubular structure (BHTS-2) (Source: Xiang and Du 2017)

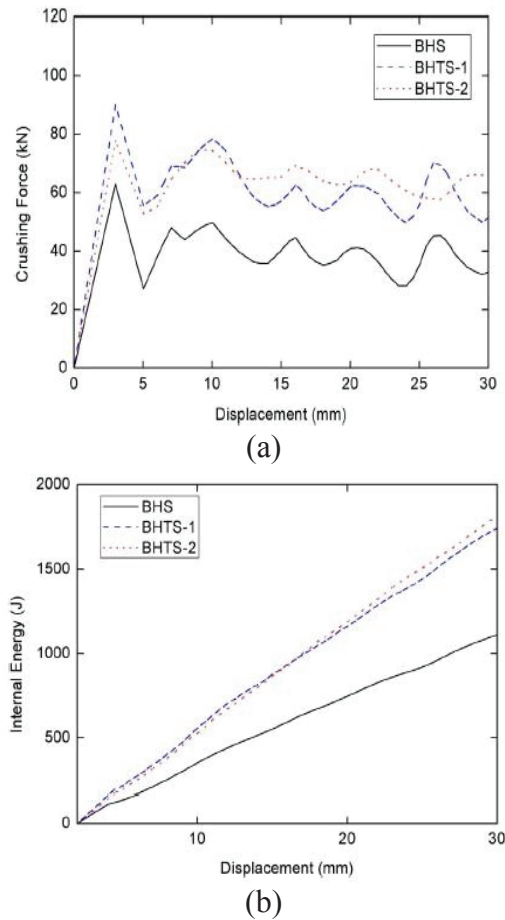


Figure 1.14. (a) Crushing force-displacement curves of bionic honeycombs, (b) Energy absorption-displacement curves of bionic honeycombs (Source: Xiang and Du 2017)

L. Zhang et al. conducted a numerical study on multi-cell tubes (BMCTs) bio-inspired from a beetle wing microstructure resisting different types of impact loads like rain droplets. Numerical analyses were performed with eighteen types of BMCTs having different cross-sectional forms: quadrilateral (Q-BMCTs), hexagonal (H-BMCTs), and octagonal (O-BMCTs) exposed to the axial loading with the constant velocity of 10 m/s, Figure 1.15. The specific energy absorption values of the BMCTs are better than the multi-cell tubes' (MCTs) excluding BMCT-1s due to higher amount of plastic deformation. Especially, Q-BMCT-1 and O-BMCT-1 have an unstable crushing mode since the columns were placed to the MCTs gaps. It was remarked that O-BMCT-6 has the highest specific energy absorption value among all structures in the study.

The optimization study was performed using various criteria such as the column thickness and diameter in order to increase the specific energy absorption, and peak crushing force.

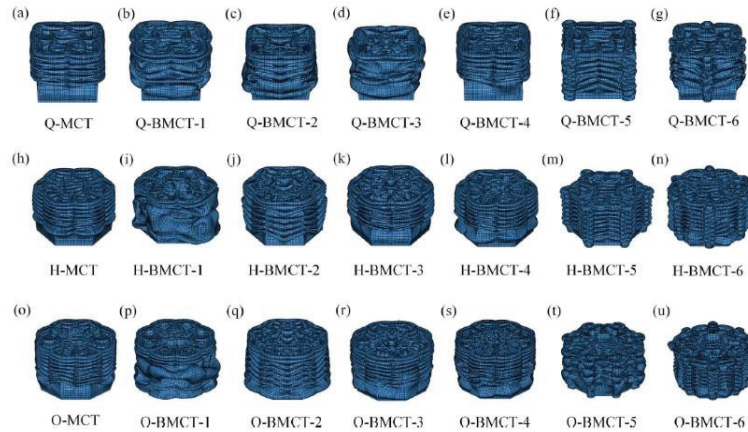


Figure 1.15. The collapse modes of multi-cell tubes (Source: Zhang, Bai, and Bai 2018)

As seen in Figure 1.16, the optimum design of the O-BMCT-6 structure is determined using non-dominated sorting genetic algorithm II and radial basis function metamodels footing the optimum SEA and PCF values (Zhang, Bai, and Bai 2018).

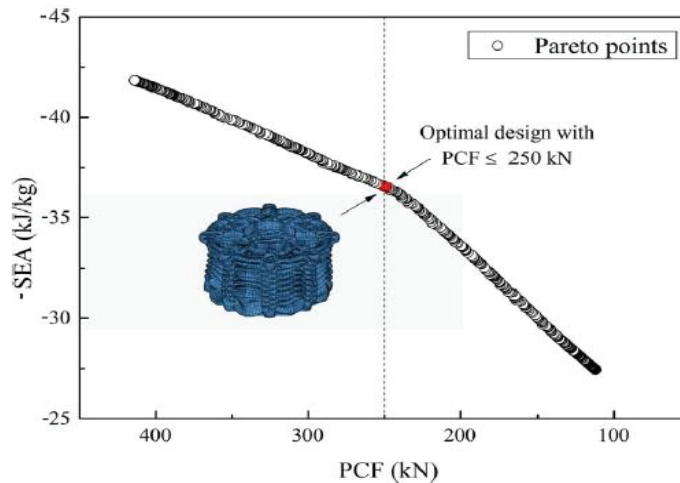


Figure 1.16. The pareto curve of the O-BMCT-6 structure (Source: Zhang, Bai, and Bai 2018)

N.S. Ha et al. studied the energy absorption behaviour of the bio-inspired honeycomb sandwich panel (BHSP) imitating from woodpecker beak internal structure, Figure 1.17. The BHSP and the first model of the conventional honeycomb sandwich panel (CHSP-1) were designed having a similar wall depth and particular core volumes. Unlike, the other model (CHSP-2) was created with the same volume but a dissimilar wall depth. These structures were then numerically subjected to the crushing load having the velocity of 10 m/s in the finite element software ABAQUS.

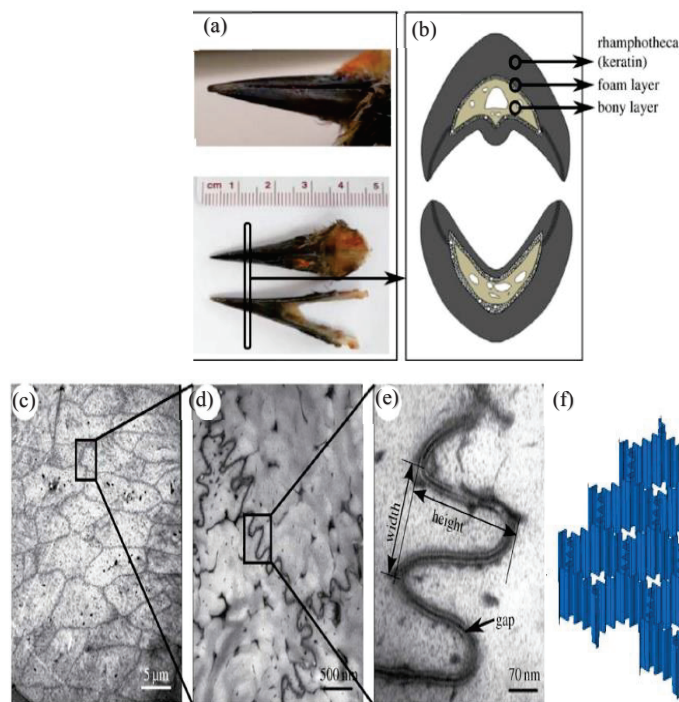


Figure 1.17. (a) Woodpecker beak, (b) the sectional view of lower and upper beak, (c) the TEM image of the keratin texture, (d) curvy honeycomb structure, (e) the enlargement image of curvy structure, (f) bio-inspired honeycomb core (Source: Ha, Lu, and Xiang 2019)

The BHSP has better performance compared to the CHSPs in terms of energy absorption capability with the occurrence of the plastic hinges sourced from the torsional deformation on the cell walls despite the bending deformation of the cell walls, Figure 1.18. Moreover, the corrugated bio-inspired structure was modeled as sixteen different designs with varying wave amplitudes and numbers. It is found out that both wave amplitude and number increased the SEA (Ha, Lu, and Xiang 2019).

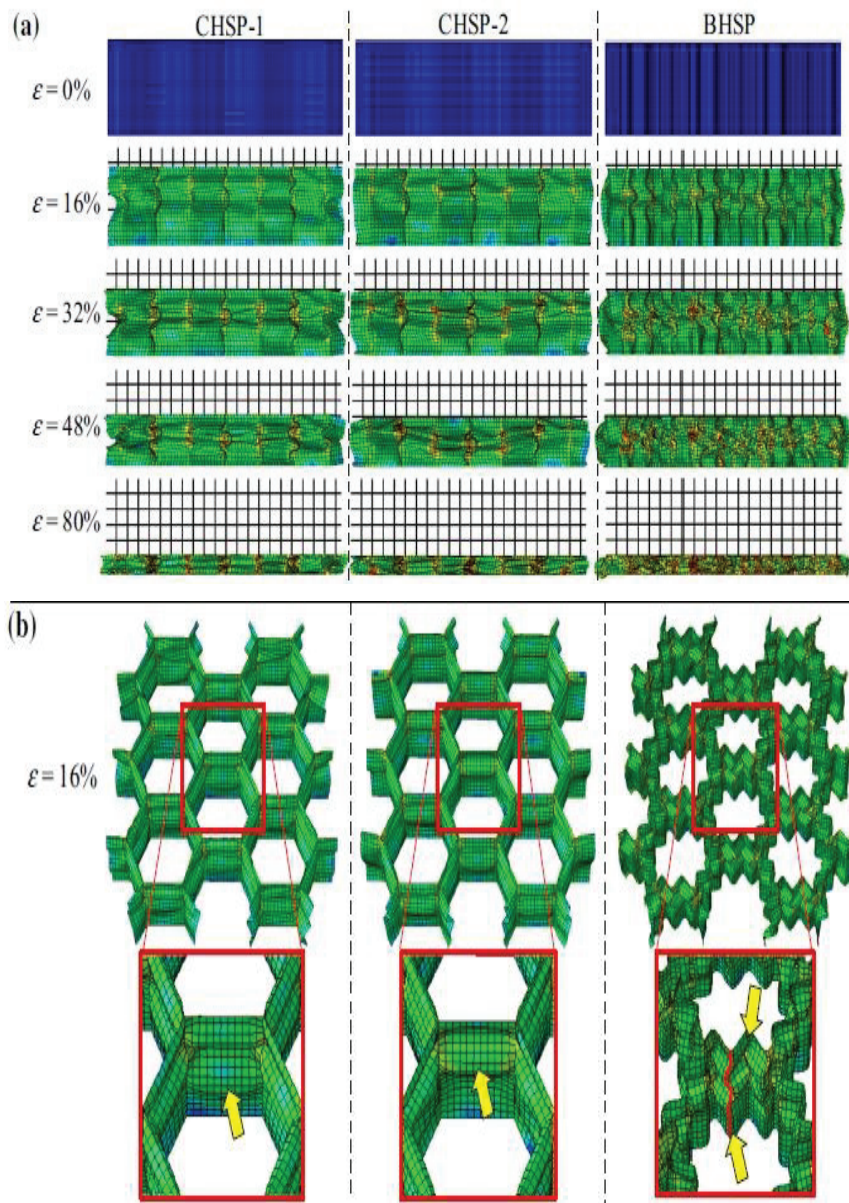


Figure 1.18. (a) Collapse modes of honeycomb sandwich panels (b) Collapse modes at crushing strain of 16% (Source: Ha, Lu, and Xiang 2019)

The study on the energy-absorption and compression behaviour of the additively manufactured polymeric structures was conducted out by S. Bates et al. The cellular structures made of two different thermoplastic polyurethane (TPU): SemiFlex and NinjaFlex having arrays with relative densities were subjected to perpetual compression tests along ribbon and transverse directions. The structures' unit cell model and their designs to compression directions are presented in Figure 1.19.

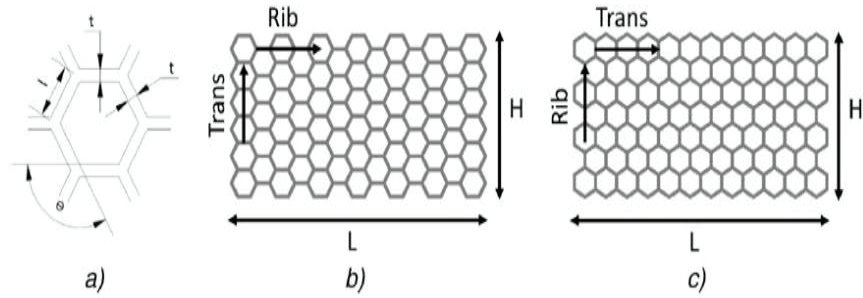


Figure 1.19. (a) The unit cell measurements, (b) the design with transverse compression direction, and (c) the design with ribbon compression direction (Source: Bates, Farrow, and Trask 2016)

It is seen that the energy absorption values per unit cubic measure of the structures crushed in the transverse direction are superior to those crushed in the ribbon direction, Figure 1.20.

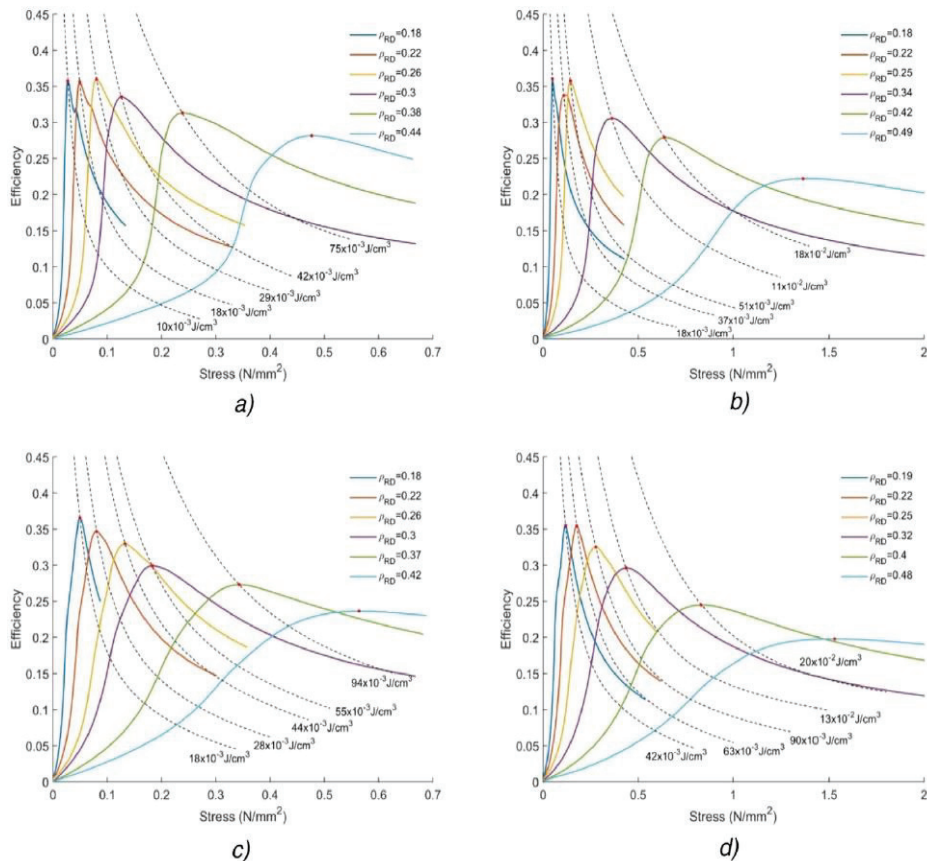


Figure 1.20. Efficiency-stress curves of cellular structures made of (a) NinjaFlex, (b) SemiFlex compressed in the ribbon direction, and specimens made of (c) NinjaFlex, (d) SemiFlex compressed in the transverse direction (Source: Bates, Farrow, and Trask 2016)

Stress and absorbed energy values were increased with increasing strain rates, and even the structure becomes more sensitive to the strain rate as the density increased, Figure 1.21 (Bates, Farrow, and Trask 2016).

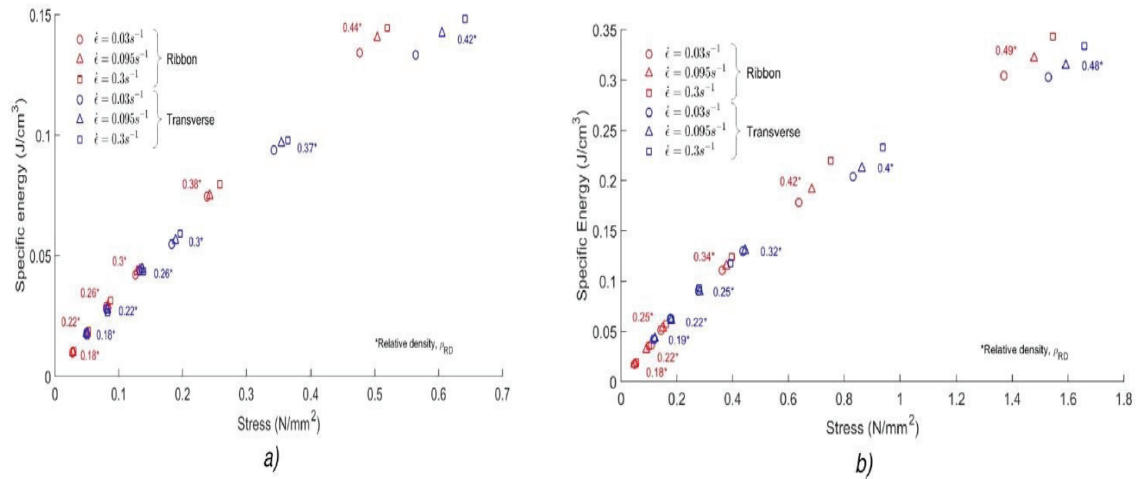


Figure 1.21. Specific energy-stress distribution of structures made of (a) NinjaFlex and (b) SemiFlex at different strain rates (Source: Bates, Farrow, and Trask 2016)

G. Dominguez-Rodriguez et al. investigated the compression of 3D printed ABS structures manufactured with different printing orientations, filler patterns, and densities. Twenty-two types of specimen, which are 25mm length and with a radius of 14.5mm, were manufactured with varying production processes. Different filling patterns and the specimen cross-section are given in Figure 1.22.

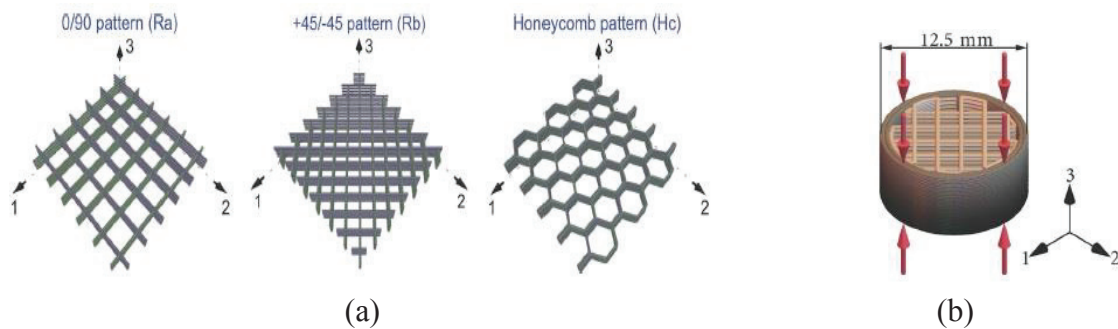


Figure 1.22. (a) Illustrations of filling patterns, and (b) the specimen cross-section exposed to compression (Source: Dominguez-Rodriguez, Ku-Herrera, and Hernandez-Perez 2018)

Solid structures (Ra-3-100% and Ra-12-100%) present higher strength and stiffness than the honeycomb configurations filled in the third direction, Figure 1.23.

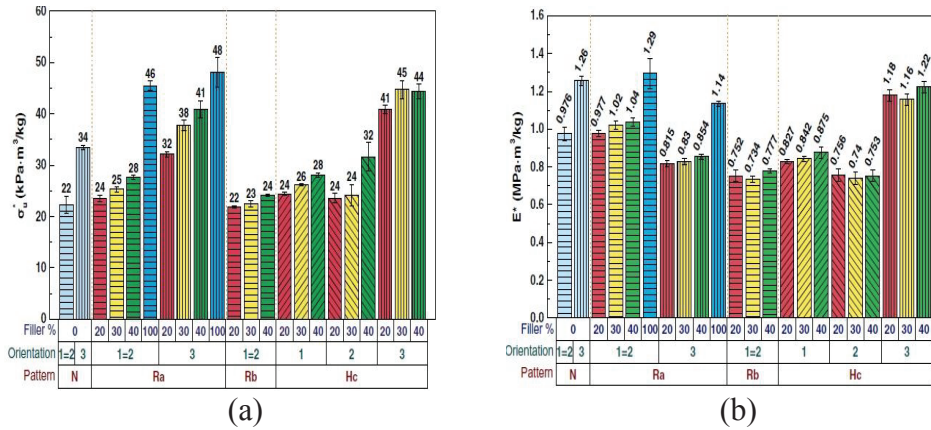


Figure 1.23. (a) Specific compressive strength and, (b) specific stiffness values of the ABS printed structures  
(Source: Dominguez-Rodriguez, Ku-Herrera, and Hernandez-Perez 2018)

Printing time has a strong effect on the mechanical properties of the structure production along with cost-effectivity. Figure 1.24 shows how the young modulus and compressive strength change with increasing printing time (Dominguez-Rodriguez, Ku-Herrera, and Hernandez-Perez 2018).

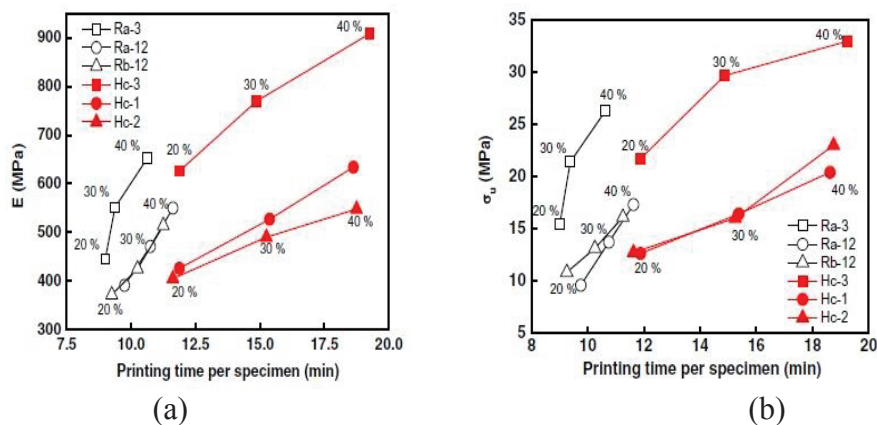


Figure 1.24. Comparisons of (a) compressive Young's modulus, and (b) compressive strength values varying with printing time per specimen for different samples with a filler percentage of 20,30 and 40%  
(Source: Dominguez-Rodriguez, Ku-Herrera, and Hernandez-Perez 2018)

H.Y. Sarvastani et al. studied the effect of the geometry, mass, and material properties on the energy absorption capacity of 3D printed sandwich panels which consisted of repeating cellular cores subjected to low-velocity impact load. Sandwich panels which formed of rectangular, hexagonal and auxetic cellular cores made of polylactic acid (PLA) with fused deposition modelling method were tested by using a drop weight test machine and supported with a numerical model, Figure 1.25.

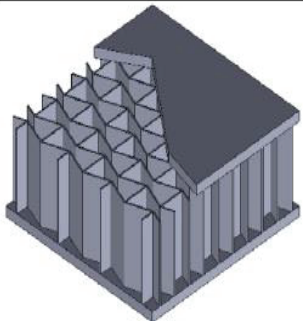
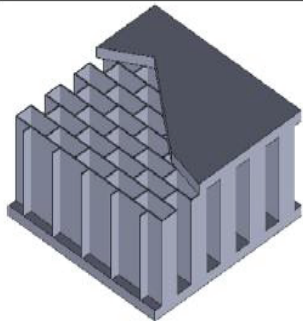
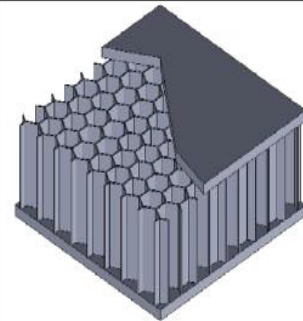
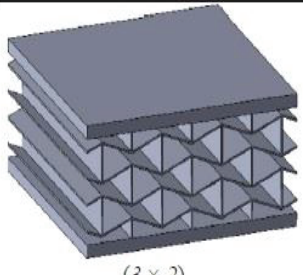
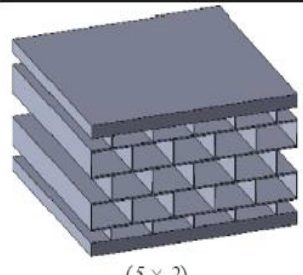
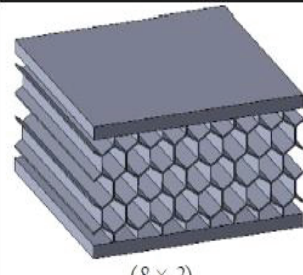
Cell type Cell direction	Auxetic core $\theta = 70^\circ$ ( $N_h \times N_v$ )	Rectangular core $\theta = 90^\circ$ ( $N_h \times N_v$ )	Hexagonal core $\theta = 120^\circ$ ( $N_h \times N_v$ )
In-plane	 ( $5 \times 3$ )	 ( $5 \times 5$ )	 ( $5 \times 8$ )
Out-of-plane	 ( $3 \times 2$ )	 ( $5 \times 2$ )	 ( $8 \times 2$ )

Figure 1.25. Sandwich panels consisted of repeating diferent cellular cores  
(Source: Sarvestani et al. 2018)

The auxetic cellular core having a relative density of 0.1 subjected to the low energy impact (3 J) has a better energy absorption performance compared to other topologies. The auxetic structure having a relative density of 0.7 also operates its function ideally for the high energy impact (66 J), Figure 1.26. As a result, the auxetic core energy absorption supremacy was observed among configurations with various relative density exposed to the different impact energies (Sarvestani et al. 2018).

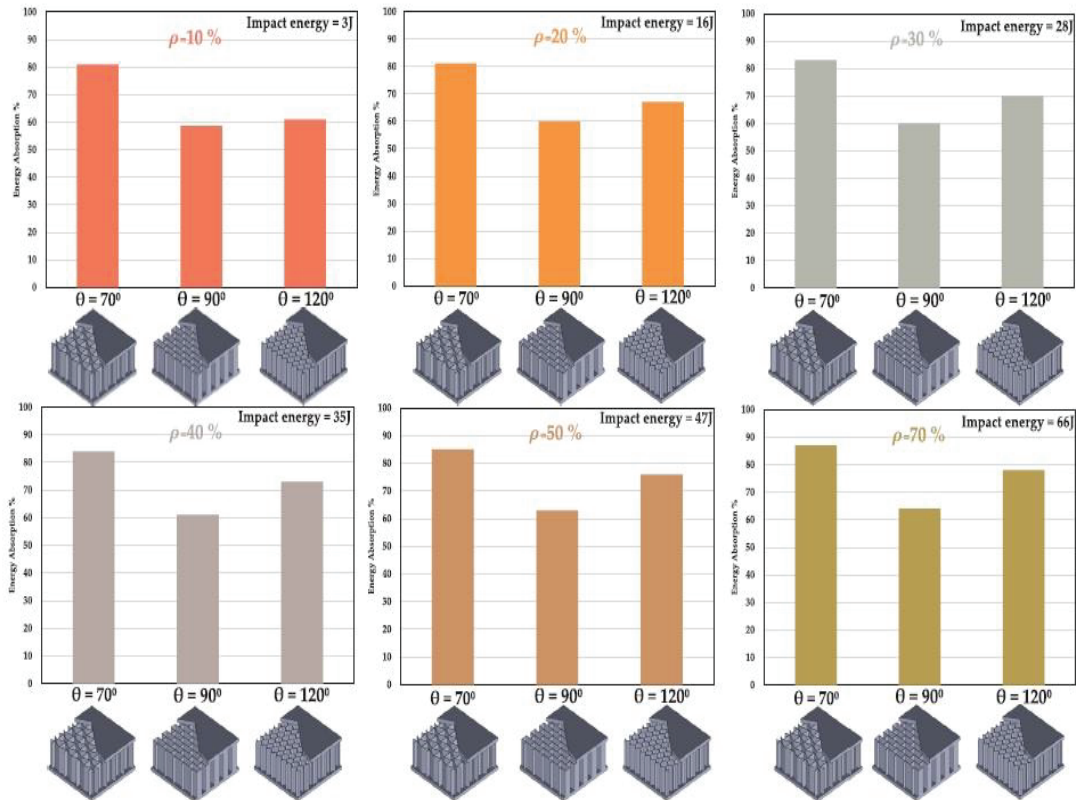


Figure 1.26. The comparison of the experimental and numerical results of sandwich panels which consisted of alternative core configurations, cell topologies, and cell relative densities in terms of energy absorption (Source: Sarvestani et al. 2018)

Y. Chen et al. studied the energy absorption capability of the hierarchical structures in comparison with the regular structures in the large deformation processes. Due to the complexity of structures, these were printed with an Objet Connex260 multi-material 3D printer using VeroWhite (a glassy polymer) material. Uniaxial compression tests were carried out using Shimadzu AGS-X to gather more information about the mechanical response of the hierarchical structures. As a consequence, the catastrophic fracture of the regular honeycombs weakened the energy absorption capability. The progressive buckling behaviour of the hierarchical structures made them the stiffer and better energy-absorber over conventional ones, Figure 1.27. It was observed that the progressive buckling starts from the local buckling and ended with a cell wall crack. The slenderness ratio of the internal triangular lattice structure was found to be another important parameter to alter the buckling behaviour (Chen, Li, et al. 2018).

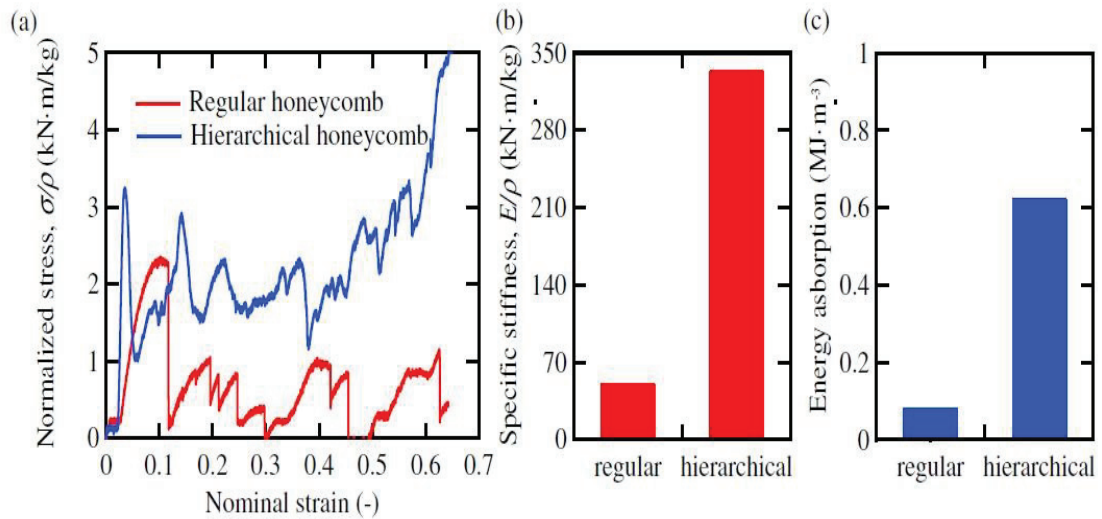


Figure 1.27. (a) Normalized stress-strain curves, (b) specific stiffness, and (c) energy absorption histograms of regular and hierarchical honeycombs (Source: Chen, Li, et al. 2018)

S. Tabacu et al. investigated the crushing behaviour and energy absorption capacity of the composite structures consisting an empty aluminium tube and 3d printed ABS poly-cell inset via experimental tests and numerical analyses. The specimens with different stacking sequences (-45/0/45/90) were manufactured by a 3d printer. The crushing behaviour and energy absorption capacity of the ABS poly-cell inset and aluminium tube were presented as both a separate and a composite structure. The ABS poly-cell inset and aluminium tube were shown in Figure 1.28. The composite structure presented better performance than the separate structures (Tabacu and Ducu 2018).

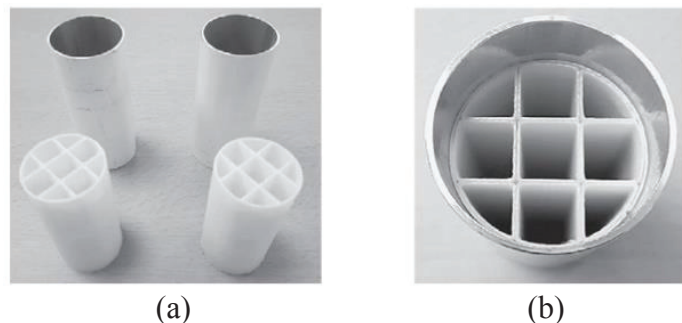


Figure 1.28. (a) Aluminium tubes and ABS poly-cell insets and (b) composite structure (Source: Tabacu and Ducu 2018)

L.Chen et al. carried out a study on the crushing mode and energy absorbing capacity of the 3D printed graded lattice cylindrical structures made of ABS material. Sandwich cylindrical structures and their two different lattice cylindrical cores: triangular and hexagonal were subjected to two different impact loads numerically to understand both the density gradient and relative density effect on the energy absorption capacity. The sandwich structure, triangular and hexagonal cellular core structures are presented in Figure 1.29.

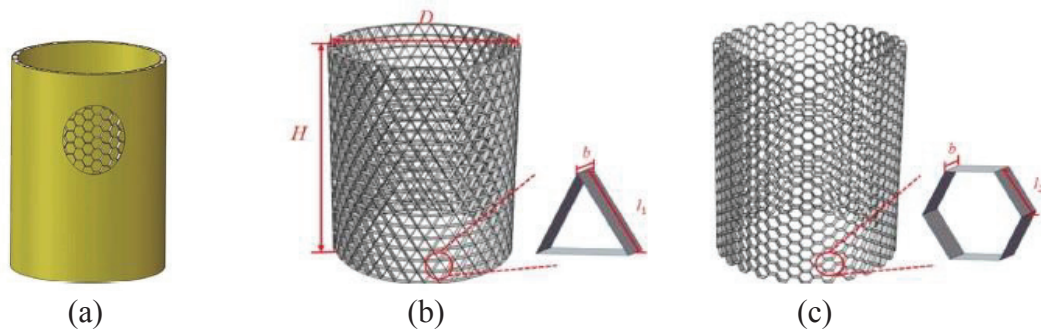


Figure 1.29. (a) The lattice sandwich structure, (b) the triangular cellular core structure and, (c) the hexagonal cellular core structure  
(Source: Chen, Zhang, et al. 2018)

The normalized plastic energy dissipation value increased along with the relative density percentage increment for triangular lattice cylindrical structures exposed to both striker velocities. However, hexagonal lattice cylindrical structures have a little complex situation. While the hexagonal structures having higher relative densities have an advantage over others subjected to the striker velocity of 0.32 m/s, the structures having low relative densities surpass other ones subjected to the striker velocity of 6.35 m/s. The hexagonal cellular structures have a negative effect on the peak crushing force due to the negative density gradient for low impact energy, and meanwhile, triangular structures have the same action for both low and high impact energy (Chen, Zhang, et al. 2018).

M. Kucwicz et al. studied the energy absorption properties of the three different cellular structures made of ABSplus material fabricated using a fused deposition method under the low loading rate with numerical analysis and experiments. In the numerical study, the mesh sensitivity analysis was performed with the honeycomb cellular structure using implicit LS-DYNA code without incorporating the erosion. The models were

created by three types of elements and different mesh densities to investigate the mesh sensitivity, Figure 1.30. While the finer mesh affects negatively the time to run the model, it does not have a significant difference with the structures having the coarse mesh in terms of the average force. Moreover, the model with brick elements has the optimum correspondence with the experiment.

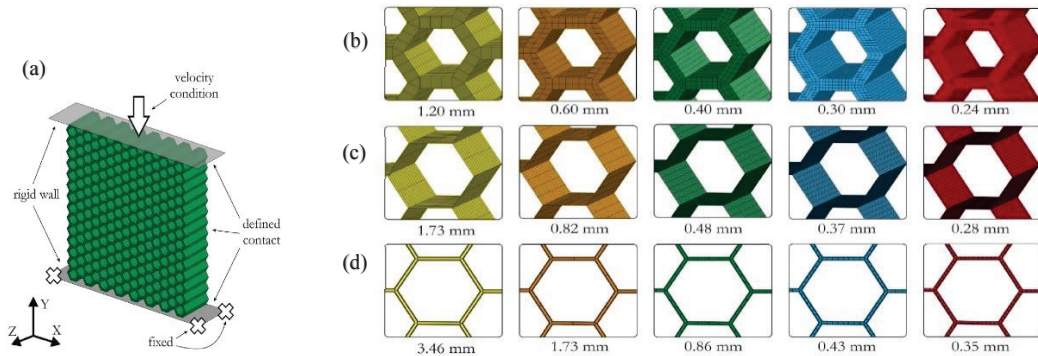


Figure 1.30. (a) The illustration of the boundary conditions of the cellular structure subjected to compression in the numerical analysis, and honeycomb models using different kinds of elements: (b) shells, (c) bricks and (d) beams with varying element sizes (Source: Kuciewicz et al. 2018)

The three different cellular structures were subjected to compression with a low velocity of 1 mm/s numerically using both implicit and explicit methods, Figure 1.31. As a result, the model using the implicit method presented larger energy absorption values than those of experiments due to the non-realization of the element deletion (Kuciewicz et al. 2018).

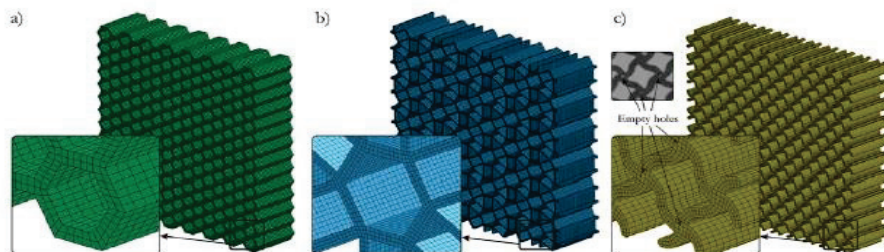


Figure 1.31. Models with different cellular structures: (a) honeycomb, (b) modified honeycomb, and (c) spiral (Source: Kuciewicz et al. 2018)

A. Fadeel et al. investigated the crush response of 3D printed polymer lattice structures having different unit cell configurations both experimentally and numerically. Four kinds of lattice structure: body-centered cubic structure (BCC), body-centered cubic having vertical members (BCCV), body-centered cubic having alternating vertical members (BCCA), and body-centered cubic having gradual alternating vertical members (BCCG), were investigated to understand the role of different vertical members on the energy absorption and stiffness. These ABSplus-P430 thermoplastic polymeric material structures were compressed experimentally and numerically at quasi-static rates.

It was observed that the BCCV structure was stronger than the others due to the buckling of the vertical members. On the other hand, inclined beams only resist bending loads and shear, hence the first fractures, which lead to low energy absorption, were observed in the local regions around these beams, Figure 1.32. As a result, the BCCV displayed better performance among configurations in terms of stiffness and energy absorption in this study (Fadeel et al. 2019).

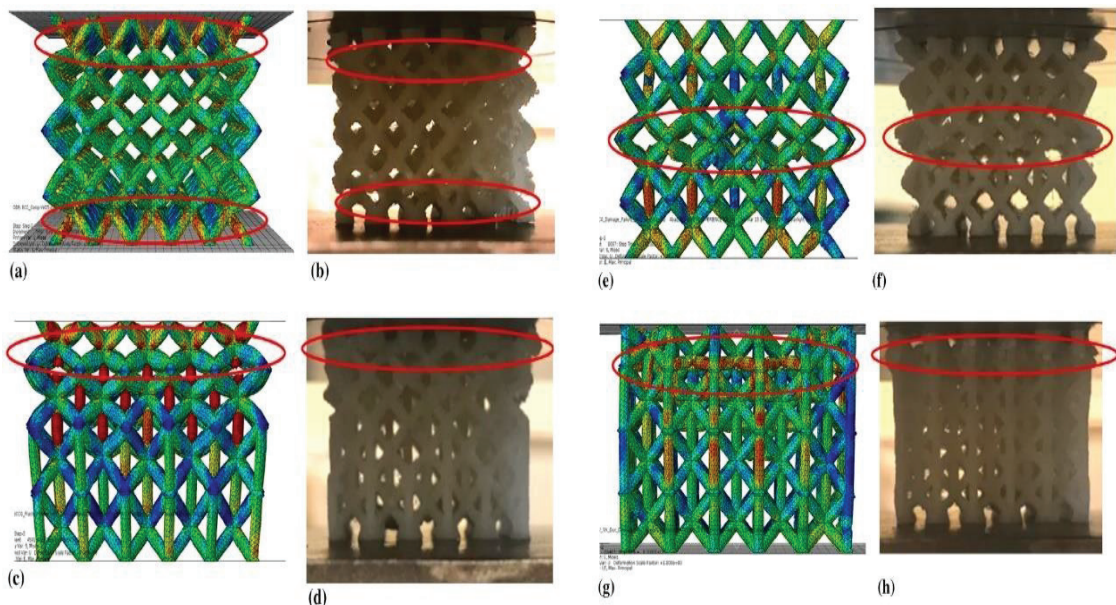


Figure 1.32. First failure locations: (a) FEA and (b) experiment images of the BCC structure, (c) FEA and (d) experiment images of the BCCG structure, (e) FEA and (f) experiment images of the BCCA structure, (g) FEA and (h) experiment images of the BCCV structure (Source: Fadeel et al. 2019)

Moreover, strain rate sensitivity is a material property to make understand the dynamic crushing behaviour change compared to the quasi-static crushing of a structure.

When the material stress response changes with the varying of applying load rates, it might be said that the material is in the effect of strain-rate, inertia or both of them. Firstly, the study on the strain rate and inertia effects of different geometrical structures is presented, and then some researches on the strain rate effect on the structures made of ABS material are investigated to understand the material behaviour specifically.

C.R. Calladine and R.W. English investigated the strain rate and inertia sensitivity on the crush response of the two kinds of structures subjected to unidirectional loading. Mild steel tube (Type I) and two mild steel plates clamped together (Type II) were subjected axial loading in quasi-static tests and made drop-height tests to evaluate the effect of the strain rate and inertia, Figure 1.33. For the same amount of energy absorbing, while Type II specimens underwent the same deflection with Type I in quasi-static tests, the lesser deflection was observed in these structures compared to those of Type I in drop-height tests. Moreover, Type II structures exhibit more sharply declined in direct proportion to increasing velocity in terms of deflection values than with Type I. Therefore, it can be said that Type II structures are more strain rate sensitive. Due to the overly sensitive to the structure geometry of initial peak force, Type I tubes can't have a significant inertia effect compared to Type II plates (Calladine and English 1984).

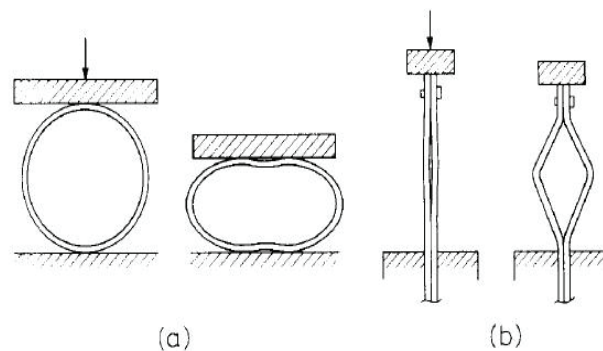


Figure 1.33. Deformation steps of (a) Type I and (b) Type II structures  
(Source: Calladine and English 1984)

S. M. Walley and J. E. Field examined the strain rate dependency of moulding polymeric materials subject to compression at different strain rates. Seventeen kinds of polymers were used to compare their rate dependency while applying compression in the range of strain rate values of  $10^{-2}$  and  $3 \times 10^4 \text{ s}^{-1}$ . While quasi-static tests were performed

by using a conventional screw-driven Instron mechanical testing machine, dynamic compression tests were made with Direct Impact Hopkinson Bar. It is observed that the strain rate dependency of most polymers does not relate too much to the strain or microstructural state. Some polymers, including ABS material, shows more strain rate sensitivity when their strain rate values exceed the value of  $10^3 \text{ s}^{-1}$  (Walley and Field 1994).

W. S. Lee and H. L. Lin implemented a study on the strain rate sensitivity of the ABS copolymer fabricated with moulding. While the yield stress and the elastic modulus became greater with the increment of the strain rate, the reduction of the fracture strain was observed. Furthermore, after the reach of peak stress, the instant decline of the stress was the reflection of the fracture in the specimen at high strain rates. It has appeared that the specimen temperature increases due to the large deformation at high strain rates, Figure 1.34.a.

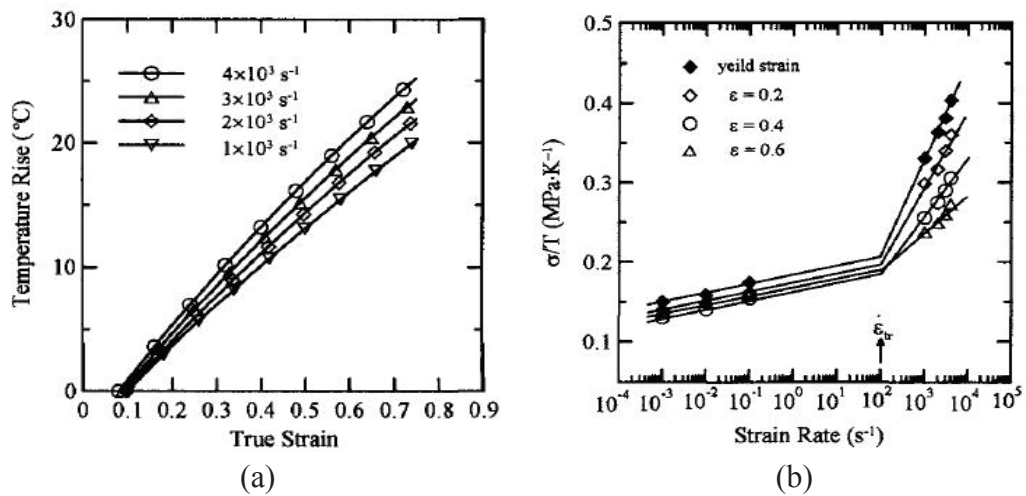


Figure 1.34. (a) The temperature change dependent on varying plastic strain and strain rate, (b) the proportion of flow stress to deformation temperature based on the varying plastic strain and strain rate (Source: Lee and Lin 2003)

As seen in Figure 1.34.b, the strain rate dependency of the ABS specimen is greater at high strain rates compared to the ones at the low strain rates. Furthermore, the strain hardening effect was detected at large strains for strain rates lower than  $10^{-1} \text{ s}^{-1}$ . It might be said that any fracture was not recognized in the specimen under quasi-static compression tests. On the other hand, the random beginning of the damage on the central

line of the cylindrical wall or on the centre zone of the specimen was noticed at high strain impact tests (Lee and Lin 2003).

The response of the ABS material to high strain rate loads to comprehend its advantages on the energy absorption was examined by G. Owolabi et al. First of all, tensile tests were made to understand the behaviour of the material at quasi-static loading rates. From the tensile test results, it was seen that the elastic modulus of the tensile tests at different low strain rates accord with each other. Some dynamic compression tests were then made to reveal the strain rate effect on the 3D printed ABS specimen. It was found out that the multiple pass collapse that may be leading the effective energy dissipation performance occurred in the range of the lower strain rates of 500 to 1000  $\text{s}^{-1}$ . Furthermore, the yield points representative of the maximum stress values demonstrated a sharp change with the increasing strain rate and it doubtless sourced from the variable deformation type. Deformed specimens at different strain rates are illustrated in Figure 1.35 (Owolabi et al. 2016).

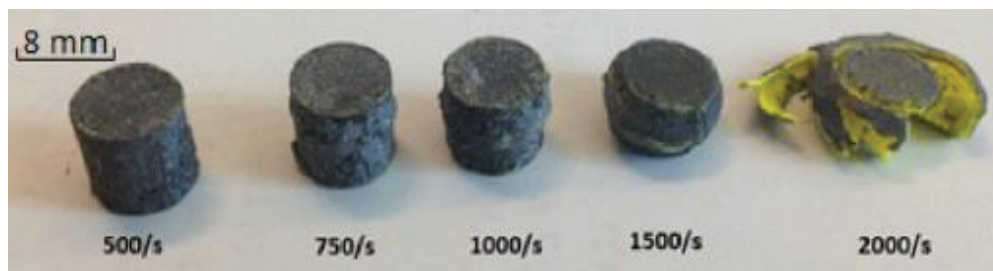


Figure 1.35. Deformed specimens at different strain rates (Source: Owolabi et al. 2016)

In addition, a different study about the strain rate sensitivity based on the tensile strength and elastic modulus of the fused deposition modelling parts printed with ABS and ABSplus material under tension was performed by someones. Tensile tests were performed with three different velocities, 5 mm/s, 10 mm/s, and 20 mm/s by using a Schenck Trebel Co. tensile experiment device. The filament fiber rupture characteristic in different cases was then investigated via Scanning Electron Microscopy (SEM). It was seen that both the tensile stress and the strain values are exhibited a rising by the increase of the strain rate. Other mechanical properties such as elastic modulus and yield strength values also increased with the increment of the strain rate. According to the SEM images,

all specimens approximately broke up from the middle section of the specimen and the brittle fracture was observed on these applications, Figure 1.36 (Vairis et al. 2016).

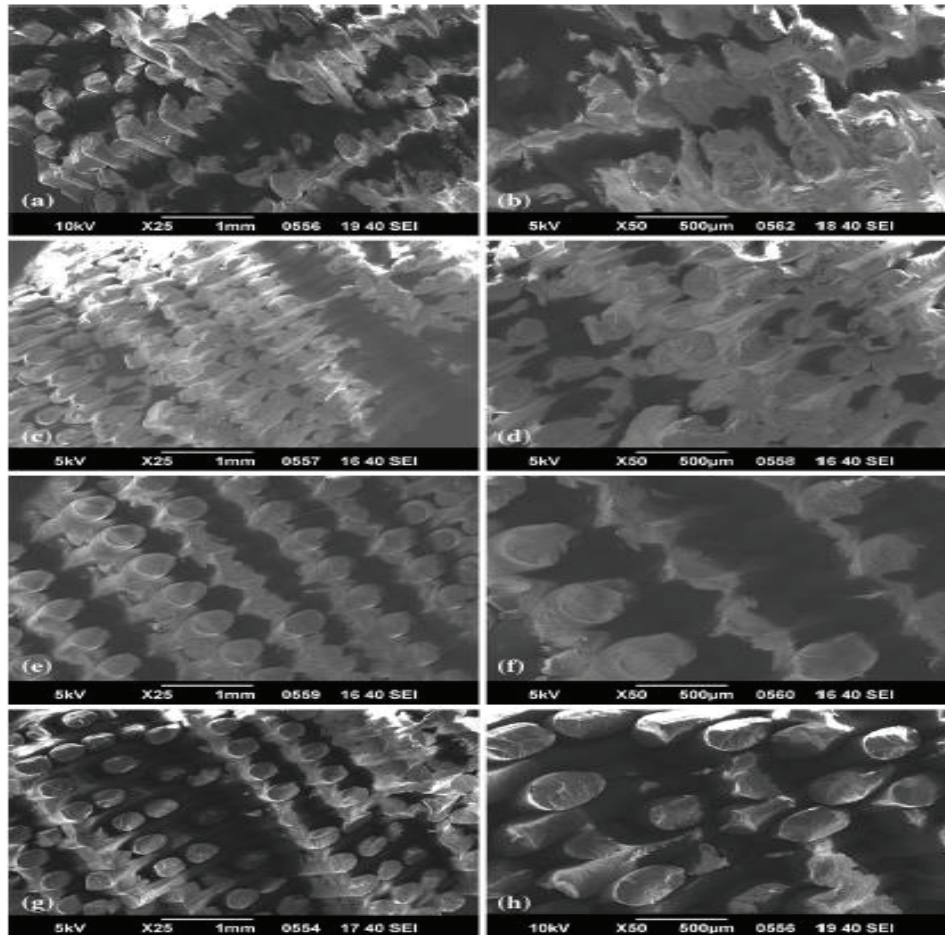


Figure 1.36. Fractography images of all ABS and ABSplus specimens (Source: Vairis et al. 2016)

### 1.3. Preliminary Work

First of all, the core geometry was determined by mimicking *Vatricania Guentheri* that is a column type of cacti from South America. The cactus grows in both hot and dry conditions, which have to survive in severe weather conditions like storms and flooding. These kinds of conditions exposes the cactus plant different types of loadings in different directions. Hence, the sectional geometry of the cactus was considered to be resistant to axial loading by folding or buckling of its ribs. Especially, this kind of cacti has certain ribs along its body. The mimicked cross-section was designed by considering these ribs

along with a tubular shell like structure. The cactus plant and the inspired core structure are presented in Figure 1.37.

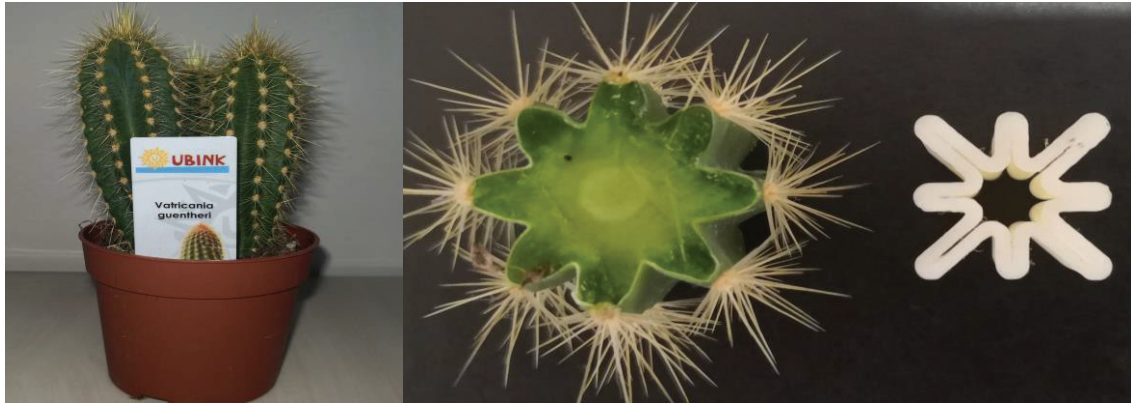


Figure 1.37. The cactus and bio-inspired core structure

In the current study, the energy absorption capacity of the cactus geometry inspired structure was investigated with other conventional structures such as cylinder, square and hexagonal numerically under dynamic loadings. To this comparison, two different methods based on the areal density was followed. The mass per cross-sectional area for all the structures compared should have the same values plus the height and thickness were also taken into account. Some required structure measurements according to the first method are presented in Table 1.1.

Table 1.1. Some measurements of core structures for the first method

Core Type	Diagonal Length (mm)	Core Mass (g)	Cross-sectional Area (mm <sup>2</sup> )	Areal Density (g/mm <sup>2</sup> )
Cactus	20	1.95	95.61	0.0203
Hexagon	33.8	2	98.12	0.0203
Cylinder	31.4	1.95	95.63	0.0203
Square	35.2	1.95	95.6	0.0203

In the first method, each of the structures has particular diagonal lengths without breaking the concept rule, Figure 1.38.

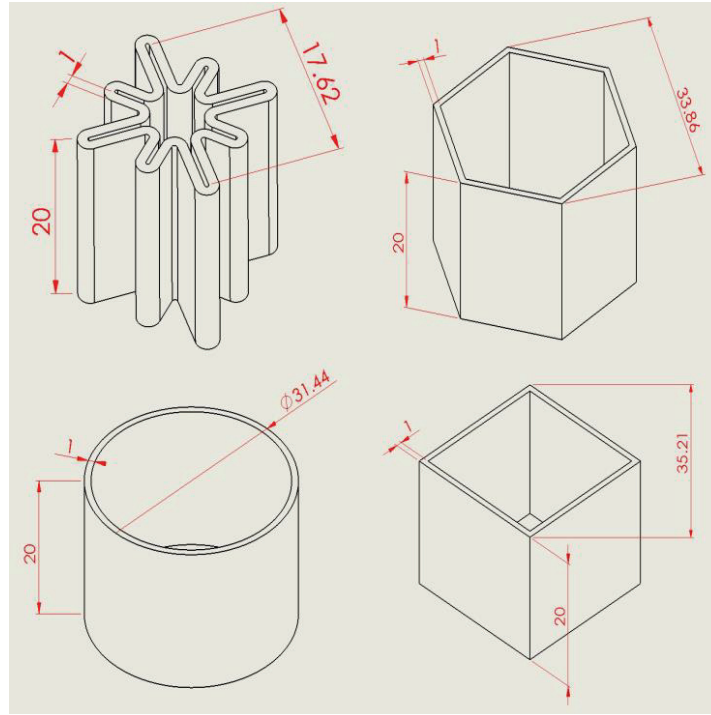


Figure 1.38. Cactus and other conventional geometry designs for the first method

These structures were subjected to direct impact pressure test with an initial striker velocity of 10 m/s to compare their specific energy absorption capability till the fracture occurs. It must be noted that the comparison is effective along the cases investigated here. It is seen that from Figure 1.39, buckling is a common instability mode for structures excluding the cylinder. On the other hand, the multiple-fold formation was observed in crushing of the cylinder. The edge splitting also had an active role in the reduction of the load-carrying capacity for both the square and hexagon. Moreover, the multiple-folding formation led to low level mean crushing forces for the cylinder. The force-displacement and specific energy absorption-displacement comparison curves are presented following the Figure 1.40.

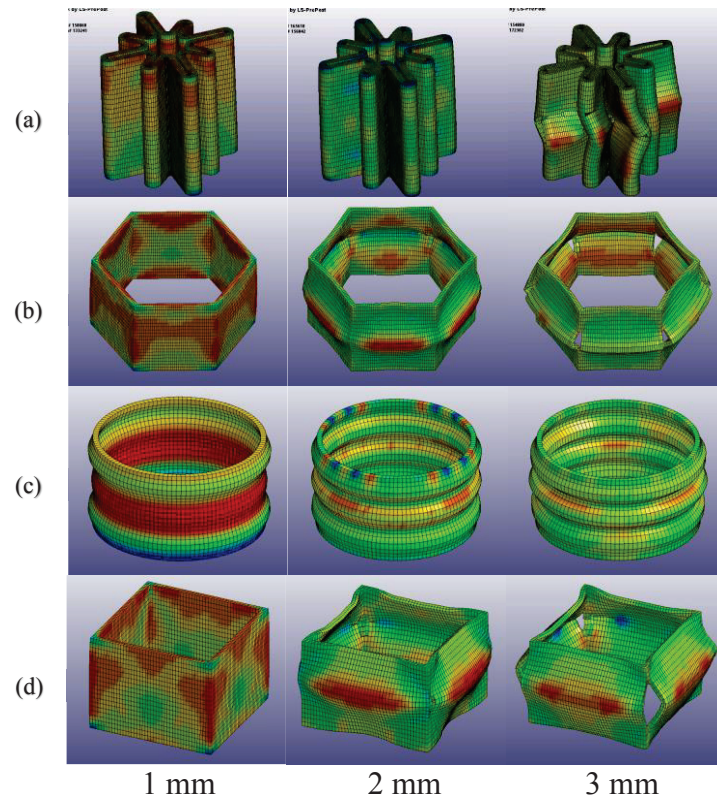


Figure 1.39. Deformation behaviour of (a) cactus, (b) hexagon, (c) cylinder, and (d) square designed structures of the first concept subjected to direct impact pressure

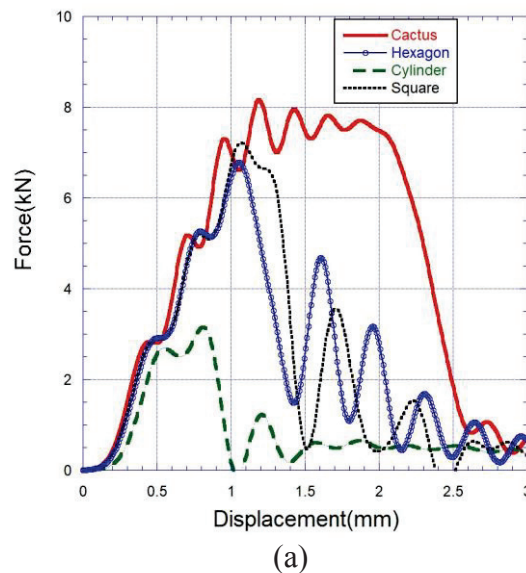
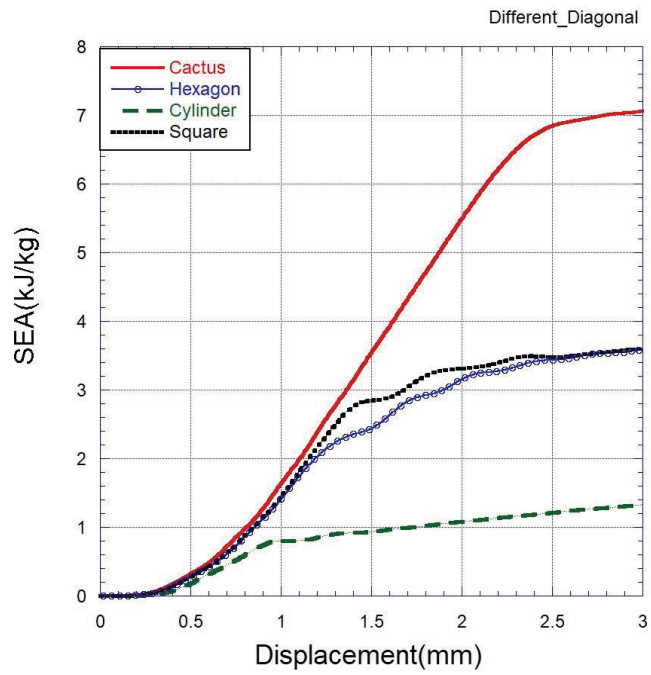


Figure 1.40. (a) Force-displacement, and (b) specific energy absorption comparison results of structures having different diagonal lengths

(cont. on next page)



(b)

Figure 1.40 (cont.)

The cactus inspired structure presented good energy absorption capability and dissipated 48% more energy than the square and hexagon competitors.

In the second comparison method, the structures having the same diagonal length, but different masses and cross-sectional areas were chosen, Figure 1.41. Details of the structures for the second method are presented in Table 1.2.

Table 1.2. Details of core structures for the second method

Core Type	Diagonal Length (mm)	Core Mass (g)	Cross-sectional Area (mm <sup>2</sup> )	Areal Density (g/mm <sup>2</sup> )
Cactus	20	1.95	95.61	0.020395
Hexagon	20	1.01	49.36	0.020462
Cylinder	20	1.22	59.69	0.020438
Square	20	0.78	38	0.020526

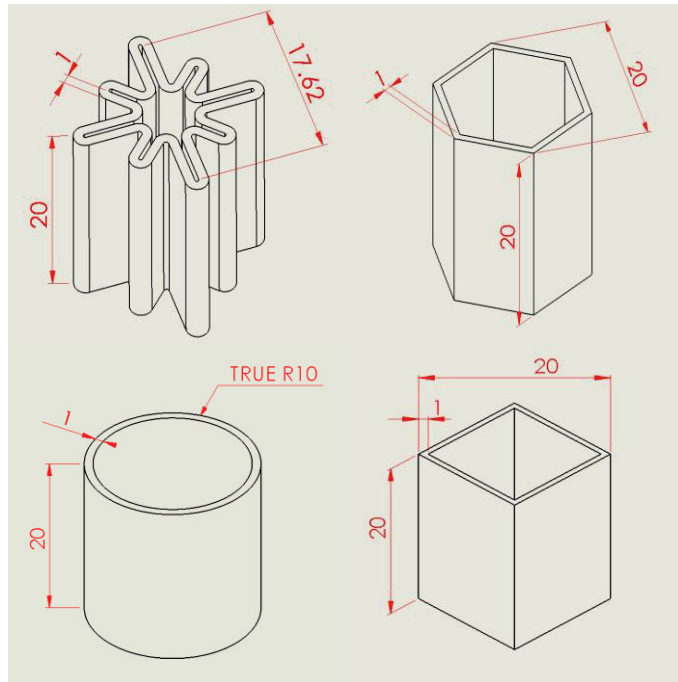


Figure 1.41. Cactus and other conventional geometry designs for the second method

These geometries were also exposed to dynamic crushing numerically with a striker velocity of 10 m/s, Figure 1.42. It is clearly seen that the hexagon and square presented inward buckling formation during the deformation till the failure. However, edge splitting was not observed for these structures, and, the load-carrying capability is a function of the number of edges. The structures having a higher number of edges have a better load resistance. Furthermore, the fold formation was observed in the cylinder but not multiple.

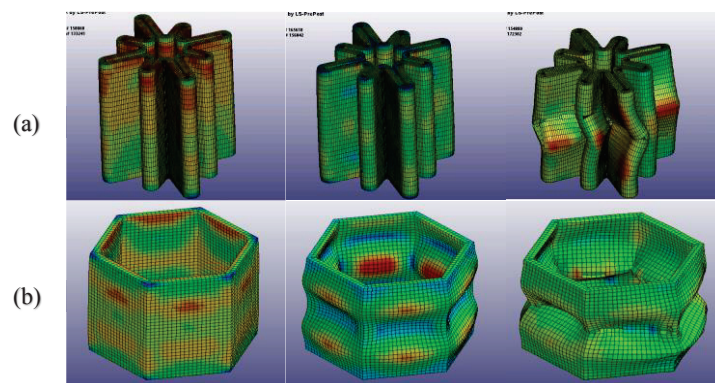


Figure 1.42. Deformation behaviour of (a) cactus, (b) hexagon, (c) cylinder, and (d) square designed structures of the second concept subjected to direct impact pressure

(cont. on next page)

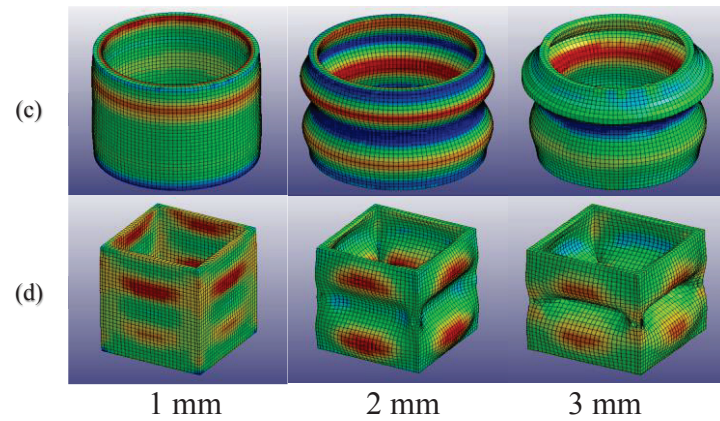
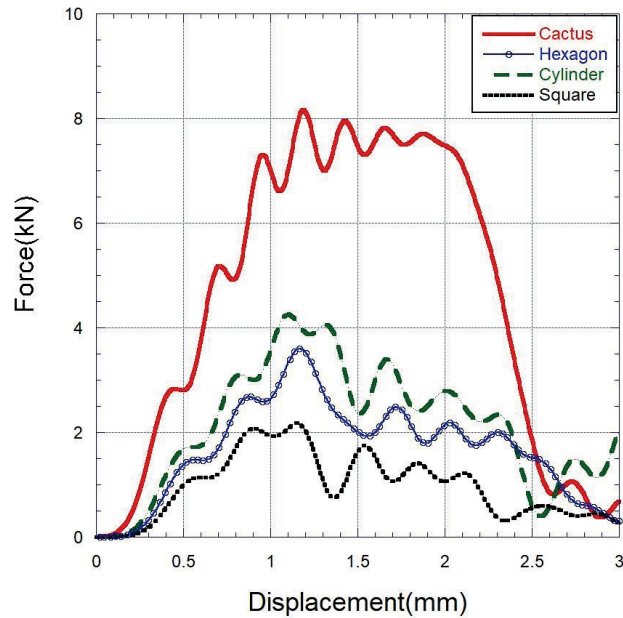


Figure 1.42 (cont.)

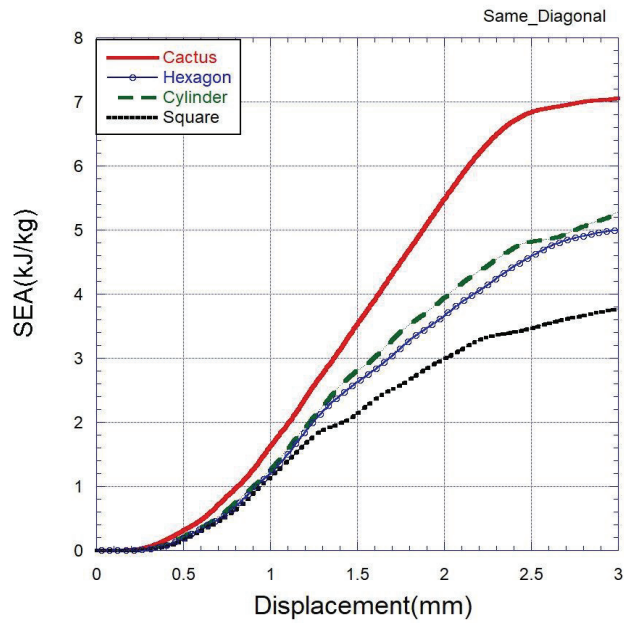
Specific energy and force displacement graphs with the same diagonal length are given in Figure 1.43. It is seen that the cactus inspired geometry presented good results in terms of specific energy absorption till it fractures. The specific energy absorption difference with the cylinder, is around 24%.



(a)

Figure 1.43. (a) Force-displacement, and (b) specific energy absorption comparison results of structures having same diagonal length

(cont. on next page)



(b)

Figure 1.43 (cont.)

## 1.4. Aim and Scope of the Study

There are several studies published on the energy absorbing capacity of the additive manufactured structures due to the ease-manufacturing feasibility of the method in complex structures. However, there is no comprehensive work done on the crushing behaviour of the structures similar to the cactus geometry studied in this thesis to the author's knowledge. In the present study, the cactus geometry made of ABS polymeric material was subjected to axial loading at various strain rates experimentally and numerically to evaluate the crushing behaviour. Both crushing behaviour mode and energy absorption capability investigation in addition to the strain rate and inertia effect research of the cactus inspired structure might be said to contribute to the literature. In the initial first chapter, a brief summary additive manufacturing of thin-walled structure, energy absorption capacity, and bio-inspiration concept were respectively given at a fundamental level. Later, the brief summary of the studies on the cross-sectional geometries were given. Researches on the crashworthiness of several bio-inspired structures were presented later on. In detail, the investigations on the crushing behaviour, energy absorption, and inertia and strain rate sensitivity of the 3D printed structures were

presented as well. In the second chapter, the printing method, the characterization of the ABS material and the test methodology were described in detail. In the third chapter, numerical analyses of the core structure subjected to both quasi-static and dynamic loadings with material properties and model parameters were given. In the fourth chapter, test and numerical results were given at static and dynamic strain, and then the strain rate and inertia effects were investigated by further using the experimental and numerical results. In the last chapter, conclusions were drawn, and for the future, the possible studies were mentioned.

## CHAPTER 2

### MANUFACTURING AND EXPERIMENTAL

In this chapter, there is information about the construction phase of the bio-inspired cactus core. The fabrication method of the cactus geometry inspired core structures are explained in detail in the first subpart of the chapter. In the second subpart, the characterization and material model selection studies in addition to experimental studies to understand the crushing behaviour of ABS are presented.

#### 2.1. Materials and Manufacturing

Bio-inspired cactus geometry cores were fabricated using Acrylonitrile Butadiene Styrene (ABS) thermoplastic polymeric material in terms of high impact resistance and low cost in comparison with the other thermoplastics. The design of the cactus inspired novel structure was developed embracing limitations such as thickness, diameter, and length of the structure, Figure 2.1. SOLIDWORKS 3D design software was used in the design process.

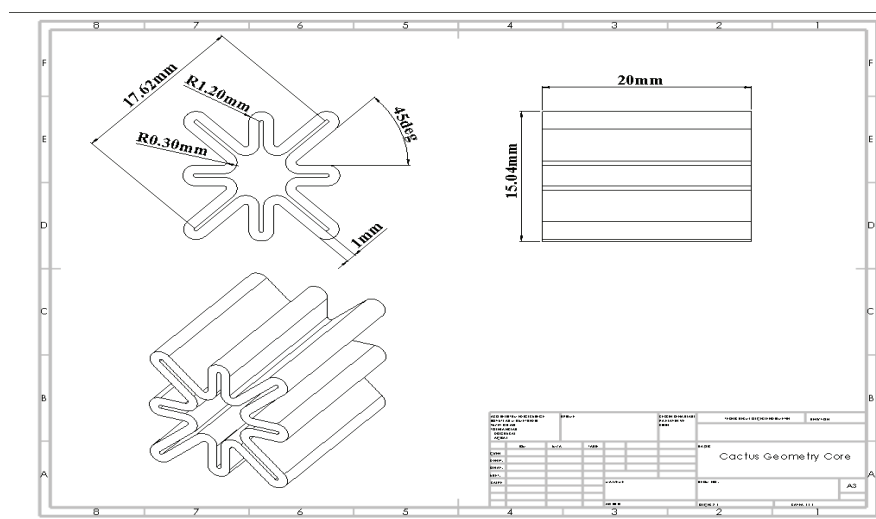


Figure 2.1. Technical drawing of the cactus geometry inspired core

Then, the technical drawing of the structure was converted to a stereolithography file format to be able to transfer into the 3D printer. The cactus geometry inspired cores were fabricated using the fused deposition technique by a Stratasys uPrint SE 3D printer, Figure 2.2.



Figure 2.2. Stratasys uPrint SE 3D printer

Specimens were uniformly printed with the layer thickness of 0.25 mm, the raster angle of  $[+45/-45]$  and the vertical build direction to the platform in this research. The building volume on the print bed is 200mm x 150mm x 150mm. Semi-liquid filaments were printed by the nozzle having a print-head with 300 °C, and deposited layer-by-layer on to the table, then these solidified almost instantly. The chamber temperature was 70 °C in this process. Printing time changed with the complexity of the specimen, and so the request time for a cactus geometry inspired core was a printing time of 13 min. However, the printing of a characterization specimen required 4 min. ABS-P430TM XL model (ivory) and SR30TM XL soluble support are the brand name of respectively ABS and support material used in the manufacturing process. The cactus geometry inspired core and the characterization specimen are illustrated with support on the print bed in Figure 2.3. The support removal was performed after waiting 3 or 4 hours in a chamber filled with a chemical solvent.



Figure 2.3. (a) The cactus geometry inspired core and (b) the characterization specimen with support on the print bed

## 2.2. Experimental Details

### 2.2.1. Material Characterization and Model Selection of ABS

Material characterization allows to understand the material structure and properties. In the current study, the characterization process helps decide on the acceptable material model and parameters. Material characterization tests of ABS polymer were carried out at both quasi-static and high strain rates, as the inertia and strain rate effect numerical studies of the cactus core required the material model parameters. Compression specimens were prepared in 8mm long and 8mm diameter, Figure 2.4.a (Owolabi et al. 2016). The tension test specimens were produced taking account to the tensile test standards of plastics (International 2015), Figure 2.4.b. However, these were altered to obtain a repeatable accuracy in characterization study.

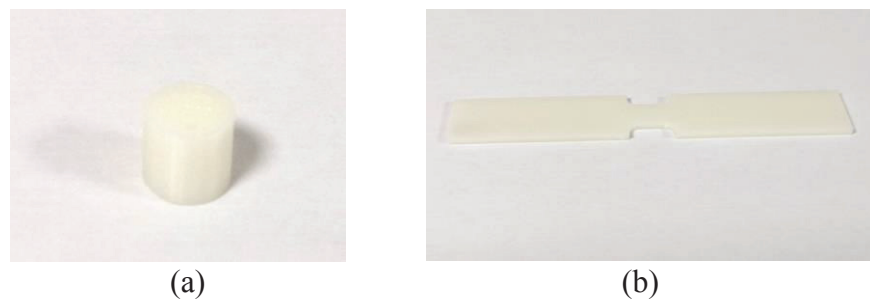


Figure 2.4. (a) Compression and (b) tension test specimens

Shimadzu universal test machine was employed for quasi-static compression with strain rates of  $10^{-1}, 10^{-2}, 10^{-3} \text{ s}^{-1}$ , Figure 2.5. It was also performed for tension tests at the strain rate of  $10^{-3} \text{ s}^{-1}$  to determine an effective failure plastic strain value, Figure 2.6.



Figure 2.5. Shimadzu universal testing machine with compression apparatus



Figure 2.6. Shimadzu universal testing machine with tension apparatus

Furthermore, the Split-Hopkinson pressure bar was preferred for achieving different high strain rates in impact tests, Figure 2.7.



Figure 2.7. Split-Hopkinson pressure bar

Gas gun, striker (35cm length), incident (200cm length) and transmitter (180cm length) bar are components of the Split-Hopkinson pressure bar mechanism. The specimen is placed applying a thin layer of vaseline at both surfaces between incident and transmitter bars made of Vascomax C350 material. The material properties of these bars are given in Table 2.1.

Table 2.1. Material properties of Vascomax C350 bars

$\rho$ (kg/m <sup>3</sup> )	E (GPa)	$\nu$
8100	180	0.3

The mechanism is activated by triggering the striker by the gas gun, and then, the striker hits the incident bar that generates a compression wave throughout the incident

bar. The wave disseminates all through parts, however, the specimen has different material and geometrical properties compared to bars. Hence, some part of the wave is dissipated through specimen and transmitter bar and the other part of the wave is reflected back to the incident bar. Strain gauges are utilized to record stress waves on the specific points on the incident and transmitter bars. The recording stress wave process is performed using an oscilloscope device, and stress wave is processed as electrical voltage values with regards to the time in the impact period. For example, the voltage-time history graph obtained from the oscilloscope for a Split-Hopkinson pressure bar test of ABS is presented in Figure 2.8.

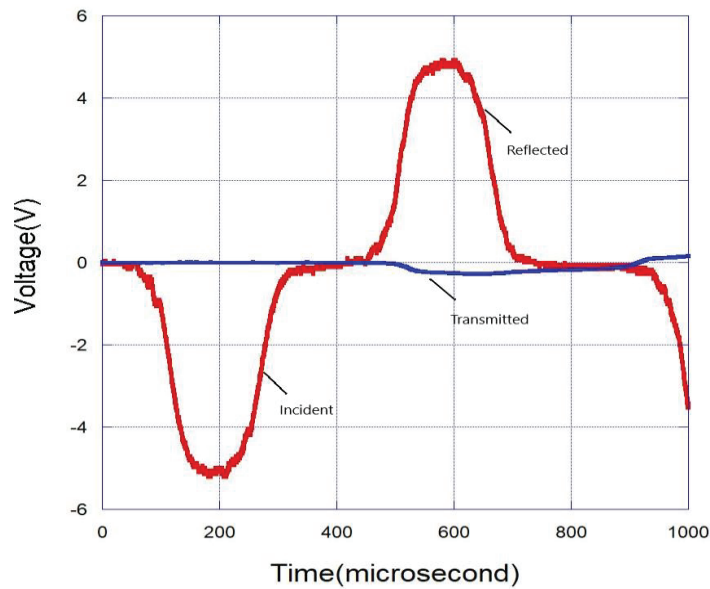


Figure 2.8. An example of the voltage-time history for ABS polymer

Then, voltage-time data were turned into the stress and strain data of the specimen using the following equations.  $GF$ ,  $K_{gain}$ , and  $V_{exc}$  are respectively the abbreviation of gage factor, gain and excitation factor in Equation 2.1.

$$\varepsilon(t) = \frac{2.V(t)}{GF \cdot K_{gain} \cdot V_{exc} \cdot (1+\nu)} \quad (2.1)$$

$$\varepsilon_s(t) = -\frac{2.C_b}{L_s} \int_0^t \varepsilon_r(t) dt \quad (2.2)$$

$$\sigma_s(t) = \frac{E_b \cdot A_b}{A_s} \varepsilon_t(t) \quad (2.3)$$

In Equation 2.2,  $C_b$  and  $L_s$  stand for the wave speed of bar and length of the specimen respectively. Meanwhile,  $E_b$  typifies the elastic modulus of the bar while  $A_b$  and  $A_s$  representing the cross-section areas of the bar and specimen separately. Consequently, some average true stress - true strain curves were obtained from both quasi-static and SHPB tests, Figure 2.9 and Figure 2.10.

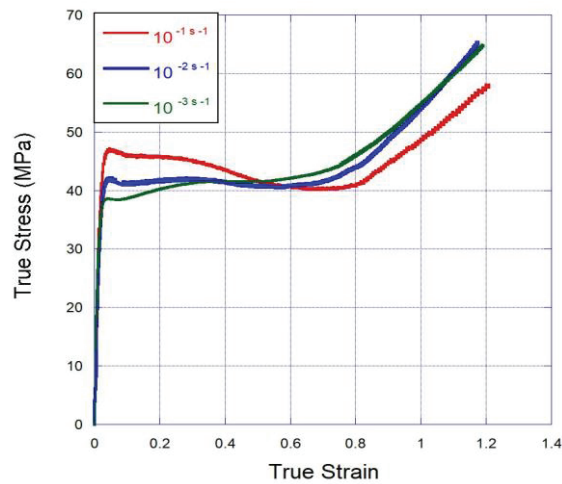


Figure 2.9. True stress – true strain curves of quasi-static compression characterization tests

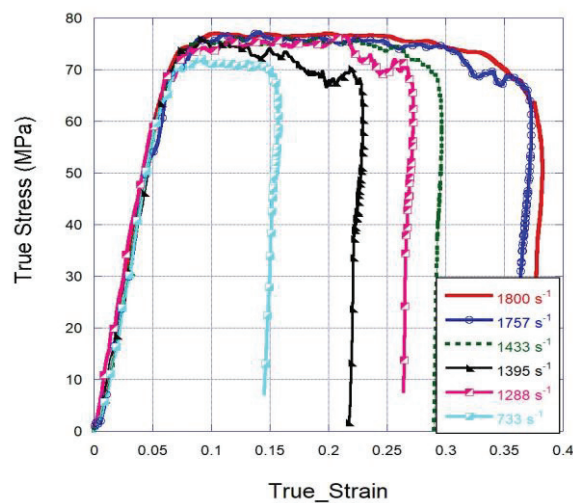


Figure 2.10. True stress – true strain curves of SHPB characterization tests

Mildly strain rate sensitivity was observed in quasi-static test results, unlike the strong strain rate sensitivity between the quasi-static and dynamic test results. The selection of the appropriate material model was made taking into account the strain rate dependence in the numerical study. Some studies on the literature were utilized to decide on the material model selection (Marangoni and Massaroppi Junior 2017, Reithofer and Fertschej 2016, Appelsved 2012, Xu et al. 2016). In LS-DYNA software, some material models such as MAT\_19, MAT\_24, MAT\_81, MAT\_89, MAT\_124, and MAT\_187 are material model options for thermoplastic structures (LSTC 2007). MAT\_24, MAT\_124, and MAT\_187 are commonly used numerical models to obtain good agreement with experiments. The characteristic features of these models are presented in Table 2.2.

Table 2.2. The characteristic features of the three common use material models for plastics

<b>Material Model</b>	<b>Viscoelasticity</b>	<b>Viscoplasticity</b>	<b>Poisson's Ratio</b>
<b>MAT_24</b>	Non-use	Available	0.5
<b>MAT_124</b>	Available	Available	0.5
<b>MAT_187</b>	Available	Available	Available

However, MAT\_187 and MAT\_124 are complex material models required complex test inputs, and their results were not correct compared to MAT\_24 elasto-viscoplastic model in the preliminary modelling study.

\*MAT\_PIECEWISE\_LINEAR\_PLASTICITY as an elastoplastic material model was chosen to achieve comparable results with the consideration of the strain rate sensitivity (Hallquist 2006). Furthermore, the equation of state is not operated and deviatoric stresses ( $s_{ij}$ ) are assigned by providing the yield function in this material model, Equation (2.4).

$$\emptyset = \frac{1}{2} s_{ij} s_{ij} - \frac{\sigma_y^2}{2} \leq 0 \quad (2.4)$$

where

$$\sigma_y = \beta \left[ \sigma_0 + f_h (\varepsilon_{eff}^p) \right] \quad (2.5)$$

where  $f_h$  is the representation of the hardening function and the linear hardening of the form is presented in the Equation 2.6.

$$f_h (\varepsilon_{eff}^p) = E_p (\varepsilon_{eff}^p) \quad (2.6)$$

It is supposed that  $E_p$  and  $\varepsilon_{eff}^p$  are the symbol of the plastic hardening modulus and the effective plastic strain, respectively. The material parameter  $\beta$  is the representation for the strain rate effects, Equation 2.7. Moreover, yield stress versus strain rate curves as a defined table may be identified for different ranks of effective strain rates.

$$\beta = \left[ 1 + \left( \frac{\varepsilon_{eff}^p}{c} \right)^{1/p} \right] \quad (2.7)$$

Deviatoric stresses are elastically updated, and then the providing yield function enables the deviatoric stresses. If the yield function does not satisfy the deviatoric stresses, the increment in the plastic strain is calculated:

$$\Delta \varepsilon_{eff}^p = \frac{\left( \frac{3}{2} s_{ij}^* s_{ij}^* \right)^{1/2} - \sigma_y}{3G + E_p} \quad (2.8)$$

where  $G$  is the shear modulus and the trial deviatoric stress state  $s_{ij}^*$  is scaled back:

$$s_{ij}^{n+1} = \frac{\sigma_y}{\left( \frac{3}{2} s_{ij}^* s_{ij}^* \right)^{1/2}} s_{ij}^* \quad (2.9)$$

Above-mentioned equations are used to solve for the normal strain increment, for shell elements, even that, the stress component in vertical direction to the mid surface of the shell element converge to zero.

In this material model, there are three options to reveal the strain rate effect of the material under high strain rates. The Cowper-Symonds model was preferred to account for strain rate sensitivity. Because the other options gave inconsistent and incompatible

results in the preliminary modelling study. The Cowpers-Symonds equation is given in Equation 2.10.

$$\sigma_y^d(\varepsilon_{eff}^p, \dot{\varepsilon}_{eff}^p) = \sigma_y^s(\varepsilon_{eff}^p) \left[ 1 + \left( \frac{\dot{\varepsilon}_{eff}^p}{C} \right)^{1/P} \right] \quad (2.10)$$

where  $\sigma_y^d$  and  $\sigma_y^s$  are represented the dynamic yield and static yield stress values.  $\varepsilon_{eff}^p$ , plastic strain and,  $\dot{\varepsilon}_{eff}^p$ , plastic strain rate are also used in the calculation. C and P are material parameters that will be used in the numerical model to reflect the rate sensitivity. Firstly, it was taken the logarithm of both sides of Equation 2.10. New equation is acceptable with an allowable R-squared value and it is presented below, Equation 2.11. In this equation, R means the ratio of dynamic yield stress to static yield stress. Based on Equation 2.11, a linear curve was fitted using obtained yield stress values from characterization tests at different strain rates, Figure 2.11.

$$\log_{10} \dot{\varepsilon}_{eff}^p = \log_{10} C + P \log_{10}(R - 1) \quad (2.11)$$

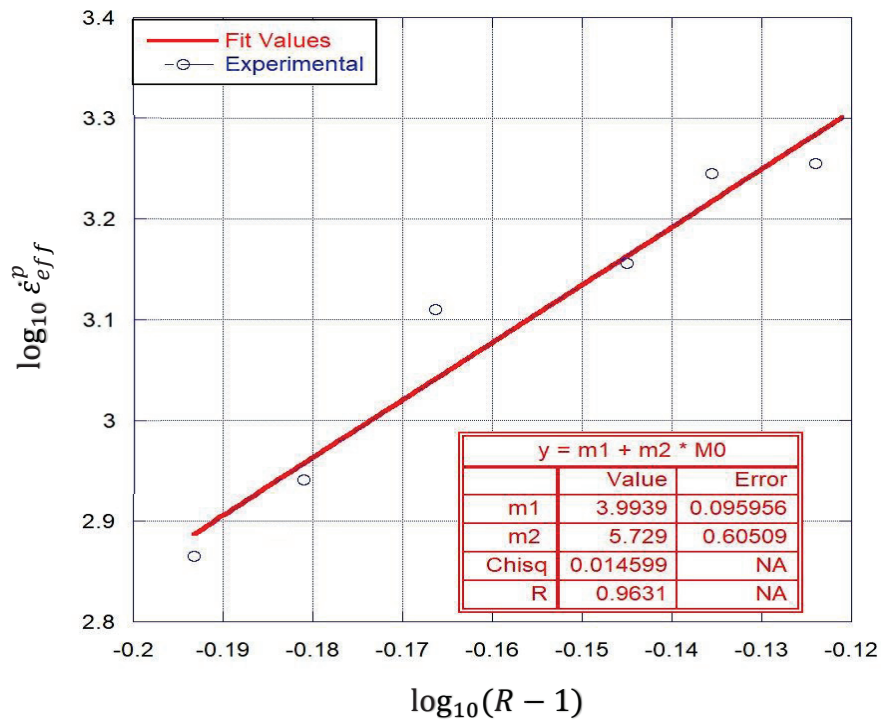


Figure 2.11. Determination of C and P parameters

C and P parameters obtained from this curve are presented in Table 2.3. M.Xu et al. made use of a similar way to find these strain rate effect parameters of two different polymeric specimens in another study (Xu et al. 2016).

Table 2.3. C and P parameters of ABS material

Material	C	P
ABS	9080.9	5.7

The effective stress - plastic strain curve obtained from quasi-static characterization test was defined as an input of the load curve ID card, Figure 2.12. Moreover, failure flag parameter was determined as an effective failure plastic strain value by using quasi-static tension test data to provide the failure occurrence on the structure, Figure 2.13.

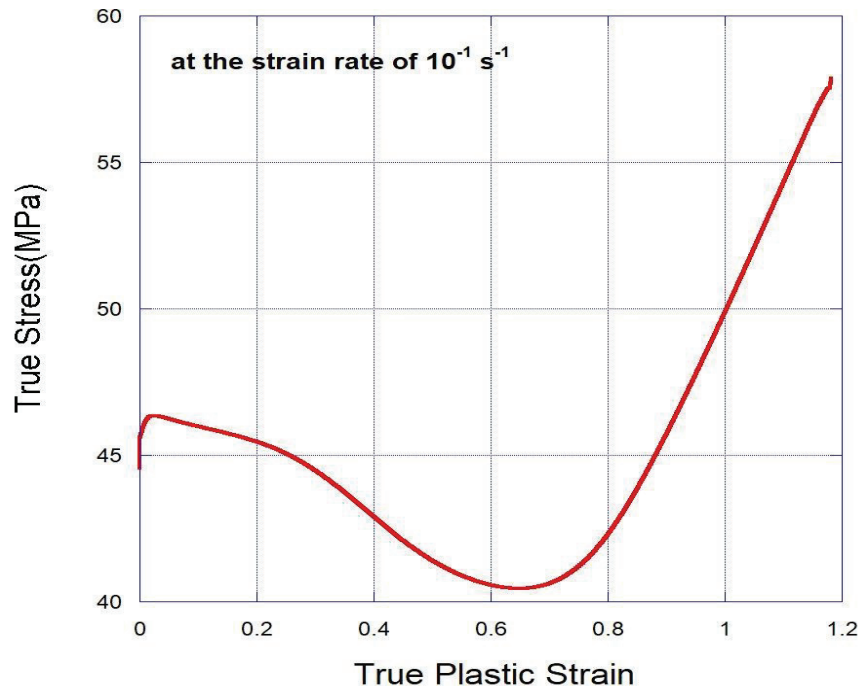


Figure 2.12. The true plastic stress-strain curve of ABS specimen under quasi-static compression at the strain rate of  $10^{-1} \text{ s}^{-1}$

Consequently, the material model parameters were obtained from material characterization tests, Table 2.4.

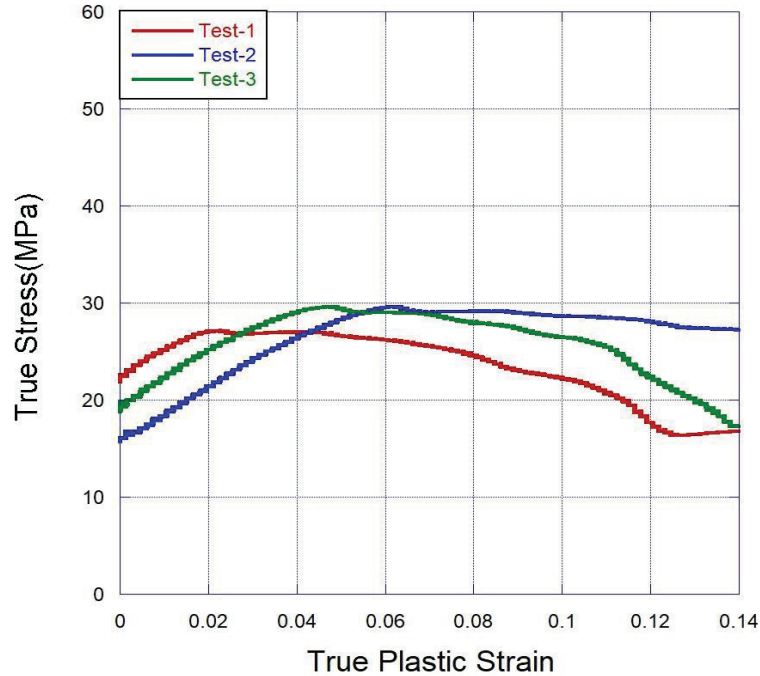


Figure 2.13. True stress – true plastic strain curves of quasi-static tensile tests

Table 2.4. Material Parameters of ABS for numerical model

$\rho$ (kg/m <sup>3</sup> )	E (GPa)	$\nu$	$\sigma_y$ (MPa)	$\epsilon_{eff}^p$
933	1.3	0.35	44.5	0.14

### 2.2.2. Quasi-Static Compression Experiments

The quasi-static compression tests were performed using a Shimadzu AG-X universal testing machine. The mechanism was presented in the previous subheading, Figure 2.5. This machine had a loading capacity of 300kN and a maximum loading rate of 1 s<sup>-1</sup>. It consists the crosshead, bottom plate, and video extensometer. While the crosshead was moving with a constant velocity, the bottom plate was fully constrained.

The crosshead speed was controlled based upon the demanded loading rate and specimen length, Equation 2.12.

$$V_{cr} = \dot{\epsilon} \times L \quad (2.12)$$

where  $V_{cr}$  is the crosshead velocity,  $\dot{\epsilon}$  is the strain rate term, and  $L$  is the length of the specimen. A video extensometer was also used to determine the displacement of the specimen in addition to the machine stroke. In this process, gage markers were used in terms of the identification of the deformation history with the video extensometer, Figure 2.14.

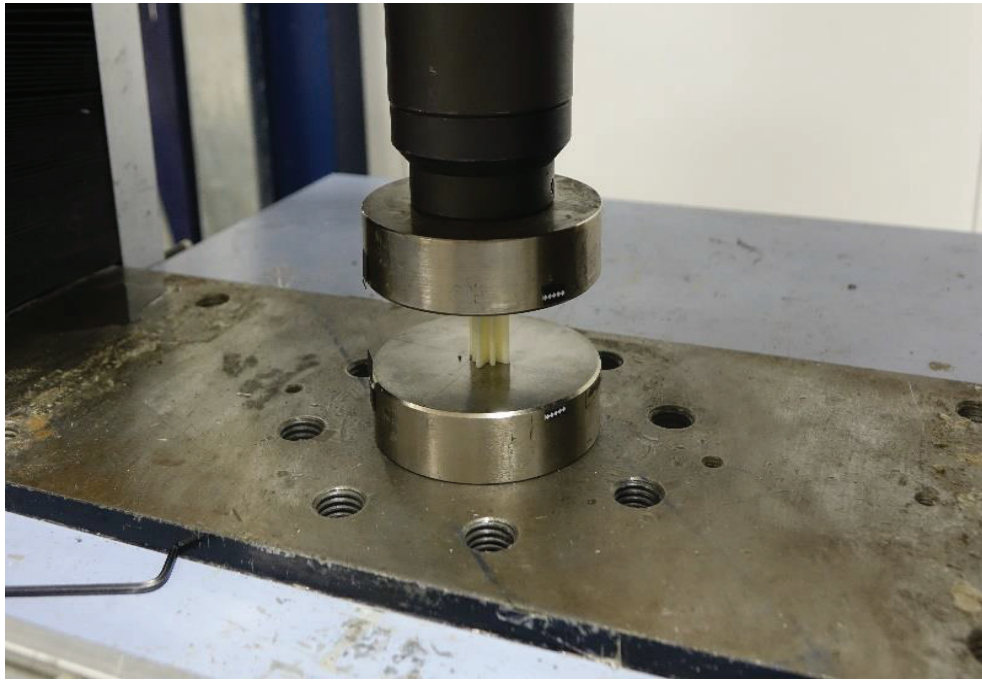


Figure 2.14. Quasi-static experimental set-up

The TRAPEZIUM X software connected with the test machine was used to control the test conditions. In the software, test type and mode were firstly arranged to single compression. Then, stroke and speed of the crosshead were defined in the testing window. The constant cross-head speed was selected as 0.02 mm/s for a resulting strain rate of  $10^{-3} \text{ s}^{-1}$ . The stroke limit was determined as 16 mm to reach the requested

deformation value for understanding the energy absorption capacity of the specimen. The gage length value was also used as an input.

### 2.2.3. Drop Weight Impact Experiments

Dynamic impact tests were carried out with Fractovis drop weight tester to understand the dynamic behaviour of the cactus geometry at moderate strain rates. The drop weight test set-up is given in Figure 2.15.



Figure 2.15. Fractovis drop-weight test set-up

Drop weight tester comprises striker, striker tip, weights, bottom platen, and velocity sensor, Figure 2.15. The striker tip with a diameter of 70 mm, and the striker with a 90 kN strain-gauge sensor were used in tests. In these tests, the specimen is placed on the fixed bottom platen which can move up and down to set up its position on the basis of the striker dropping height. These were determined for the impact velocities of 3.5 and 5 m/s in the software. Force-displacement data were recorded with DAS 16000 data

acquisition system. Photron Fastcam high-speed camera was also used to record the deformation history of the specimen.

#### 2.2.4. Direct Impact Hopkinson Pressure Bar Experiments

Direct impact Hopkinson pressure bar tests were performed to comprehend the dynamic crushing behaviour of the cactus geometry at high strain rates. The illustration of direct impact test set-up for dynamic crushing of cactus geometry is given in Figure 2.16. In this method, the specimen was placed on the front side of the transmitter bar using a thin layer of vaseline.

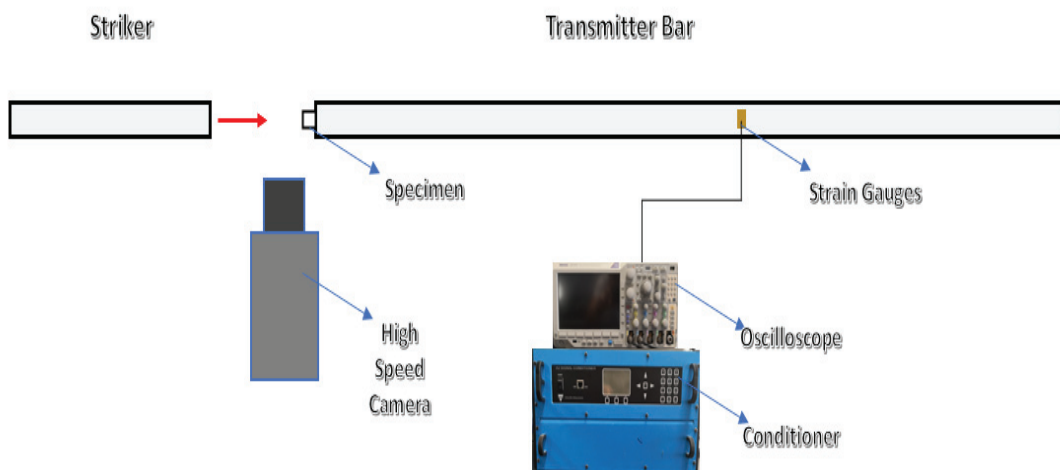


Figure 2.16. The illustration of direct impact Hopkinson bar experimental set-up

Different from SHPB tests, striker impacts directly to the specimen and the resulting stress propagates through the specimen and transmitter bar. The strain gauge was only placed on the middle of the transmitter bar. The voltage-time curve recorded by the oscilloscope can be seen in Figure 2.17. This recorded voltage-time curve was turned into the stress history by using Equation 2.3, and meanwhile, displacement history was obtained by the high-speed camera records.

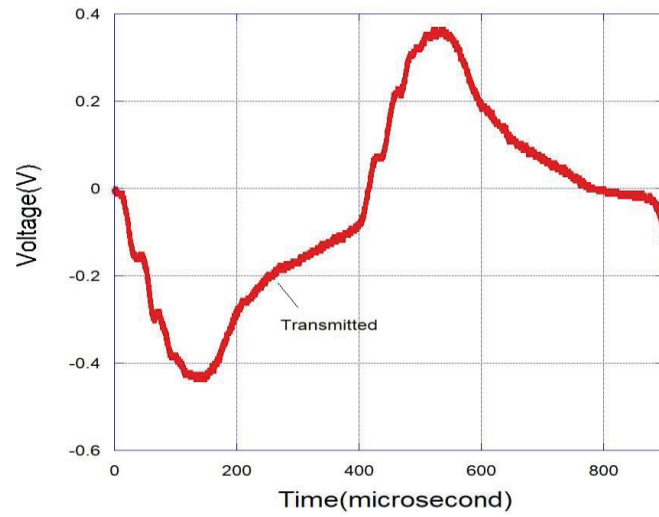


Figure 2.17. Voltage – time curve for ABS cactus geometry inspired core after direct impact Hopkinson bar test

## CHAPTER 3

### NUMERICAL STUDIES

Numerical modelling was performed to understand the deformation behaviour better. The finite element method (FEM) is one of numerical tools to solve complex engineering problems. In this study, the crushing behavior, strain rate sensitivity and inertia effects for the bio-inspired cactus geometry core structure were investigated numerically. This helped to understand the crushing behaviour and energy absorption of the cactus structure at different boundary conditions and deformation rates. LS-DYNA finite element program was used for this purpose (LSTC 2007).

#### 3.1. Crushing Modelling of Cactus Geometry Inspired Core

The crushing deformation of the cactus geometry was modeled with two different schemes; implicit and explicit. The crushing model is presented in Figure 3.1. Top and bottom plates were assigned for both quasi-static and dynamic compression modelling. The top plate was allowed to move in the direction of loading, whereas, the linear and rotational movements of the bottom plate was constrained in all axes. In both models, the constant stress solid element formulation was used for both plates and cactus core. In contact cards, the static and dynamic friction coefficients were chosen as 0.3 and 0.2 in all models, respectively.

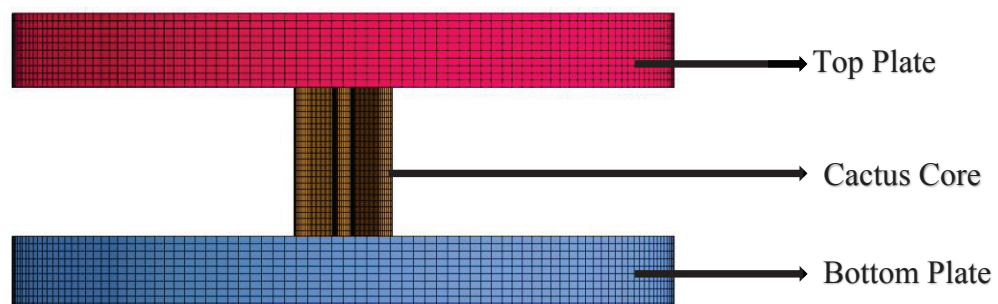


Figure 3.1. Crushing model of the cactus geometry inspired core

### 3.1.1. Quasi-Static Modelling (Implicit)

The number of load or time steps of the implicit method is less than that of the explicit (LSTC 2007). Non-linear problems, which include large deformations, can be stably solved with this method. Therefore, the implicit method was used for the modelling of the quasi-static crushing test. In order to obtain the quasi-static compression, the displacement-time curve with the constant crosshead velocity in the experiment was defined for the top plate. The two types of contact definitions containing MORTAR, were preferred in the contact card; `AUTOMATIC_SINGLE_SURFACE_MORTAR` for preventing the interpenetration in cactus geometry inspired core structure, and `AUTOMATIC_SURFACE_TO_SURFACE_MORTAR` for preventing penetration between plates and the core.

### 3.1.2. Dynamic Impact Modelling (Explicit)

The explicit solver was used in modelling the dynamic impact tests such as drop weight and direct impact test with higher impact velocities than quasi-static ones. Drop tower test simulation was modeled with a top plate having initial impact velocity and a fixed bottom plate. Unlike the quasi static model, `ERODING_SINGLE_SURFACE` and `ERODING_SURFACE_TO_SURFACE` contact types are used. The direct impact tests were also modeled on the basis of experimental set-up, Figure 3.2.

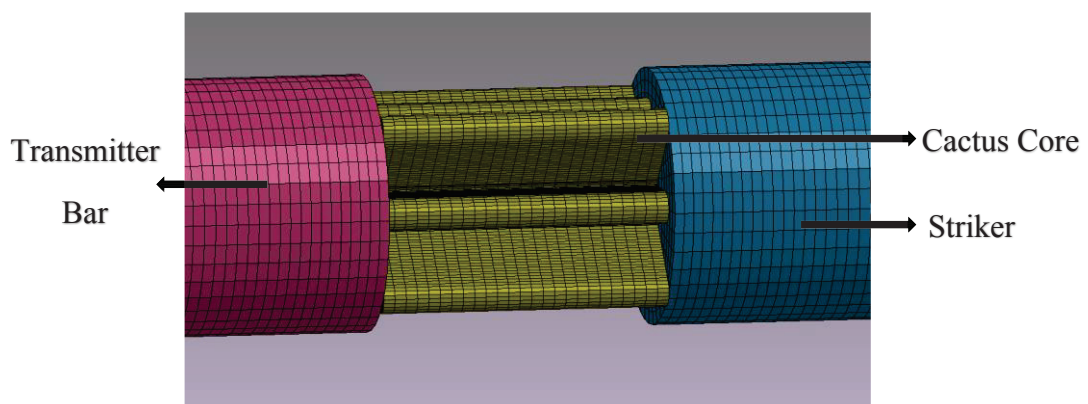


Figure 3.2. Direct impact model of the cactus geometry inspired core

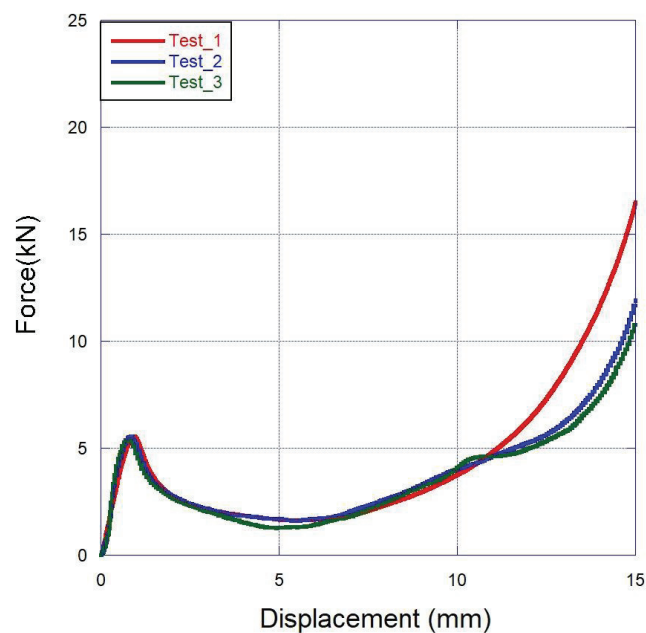
Based on the experimental data, the initial impact velocity of the striker was described by using `*INITIAL_VELOCITY_GENERATION` in this numerical model. Vascomax C350 bar is modeled using `*MAT_ELASTIC` material model. `AUTOMATIC_SINGLE_SURFACE` card was also chosen for the contacts among all parts.

## CHAPTER 4

### RESULTS AND DISCUSSIONS

#### 4.1. Crushing Behaviour and Energy Absorption of Cactus Geometry Inspired Structure

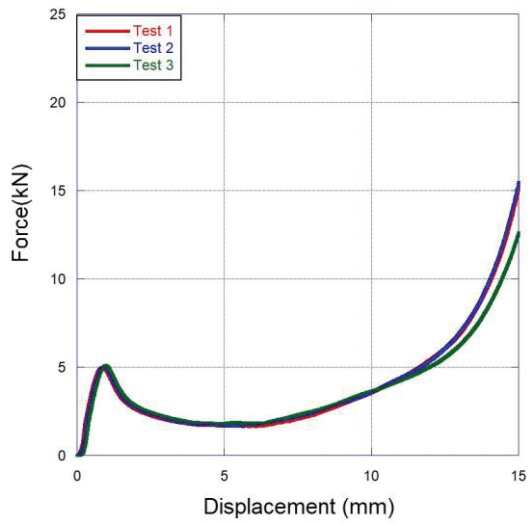
Quasi-static compression tests were performed with the Shimadzu AG-X test machine to understand the crushing behavior of the cactus geometry at different strain rates ranging from  $10^{-1}$ ,  $10^{-2}$ , and  $10^{-3}$   $s^{-1}$ . In order to observe the repeatability of the tests at different strain rates, three compression tests were performed for each loading rate. Test results as force-displacement curves are given in Figure 4.1.



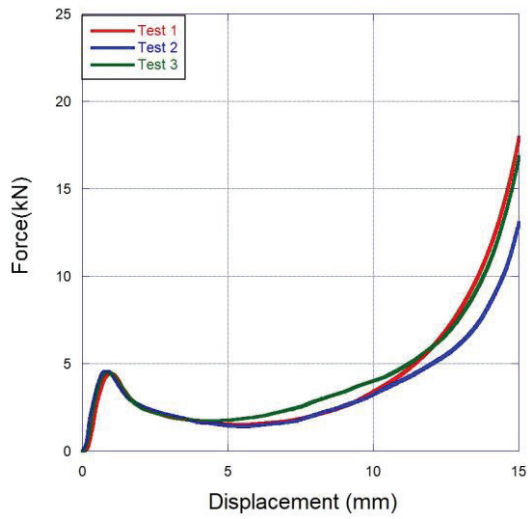
(a)

Figure 4.1. Experimental force-displacement curves of cactus geometry inspired core; (a)  $10^{-1}$   $s^{-1}$ , (b)  $10^{-2}$   $s^{-1}$ , (c)  $10^{-3}$   $s^{-1}$ , and (d) the comparison of some tests at different strain rates

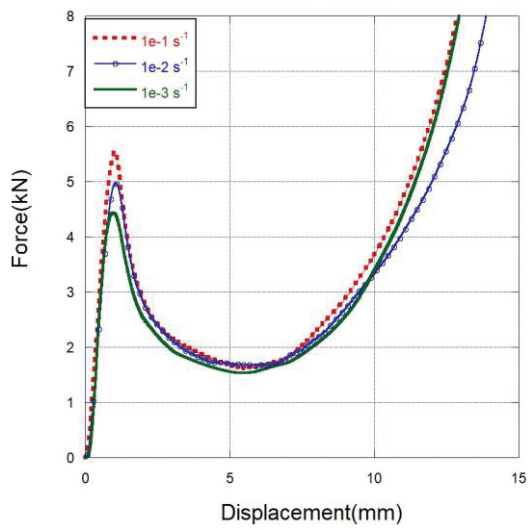
(cont. on next page)



(b)



(c)



(d)

Figure 4.1 (cont.)

It is clearly seen that the test results show a good correlation in among themselves for each strain rate. When the strain rate changed from  $10^{-3}$  to  $10^{-1} \text{ s}^{-1}$ , only the initial peak force was increased, but in the rest of the deformation process including the densification section, the force-displacement curve exhibited a similarity at different strain rates. Similar findings were revealed in another study on the investigation of the compression of the phenolic hexagonal honeycomb structures, the initial peak stress exhibited a significant increase compared to the load response at the rest of the deformation when the strain rate was increased from 10 to  $50 \text{ s}^{-1}$  (Heimbs et al. 2007). In the current study, the initial peak force increased by nearly 18% for the strain rate variation from  $10^{-3}$  and  $10^{-1} \text{ s}^{-1}$  under quasi-static compression.

In Figure 4.2, the comparison of the force-displacement curves obtained from experiment and numerical model is given. In addition, deformation model of discrete displacement levels from both experimental and numerical analyses, is presented for the comparison purposes, Figure 4.3.

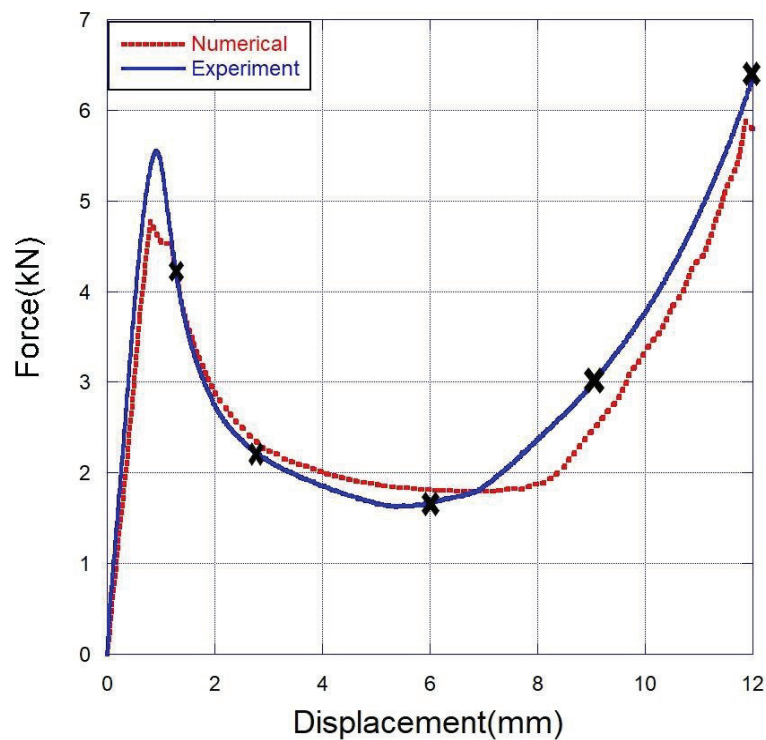


Figure 4.2. Experimental and numerical force-displacement curves of the cactus geometry inspired core at quasi-static compression test at the strain rate of  $0.1 \text{ s}^{-1}$

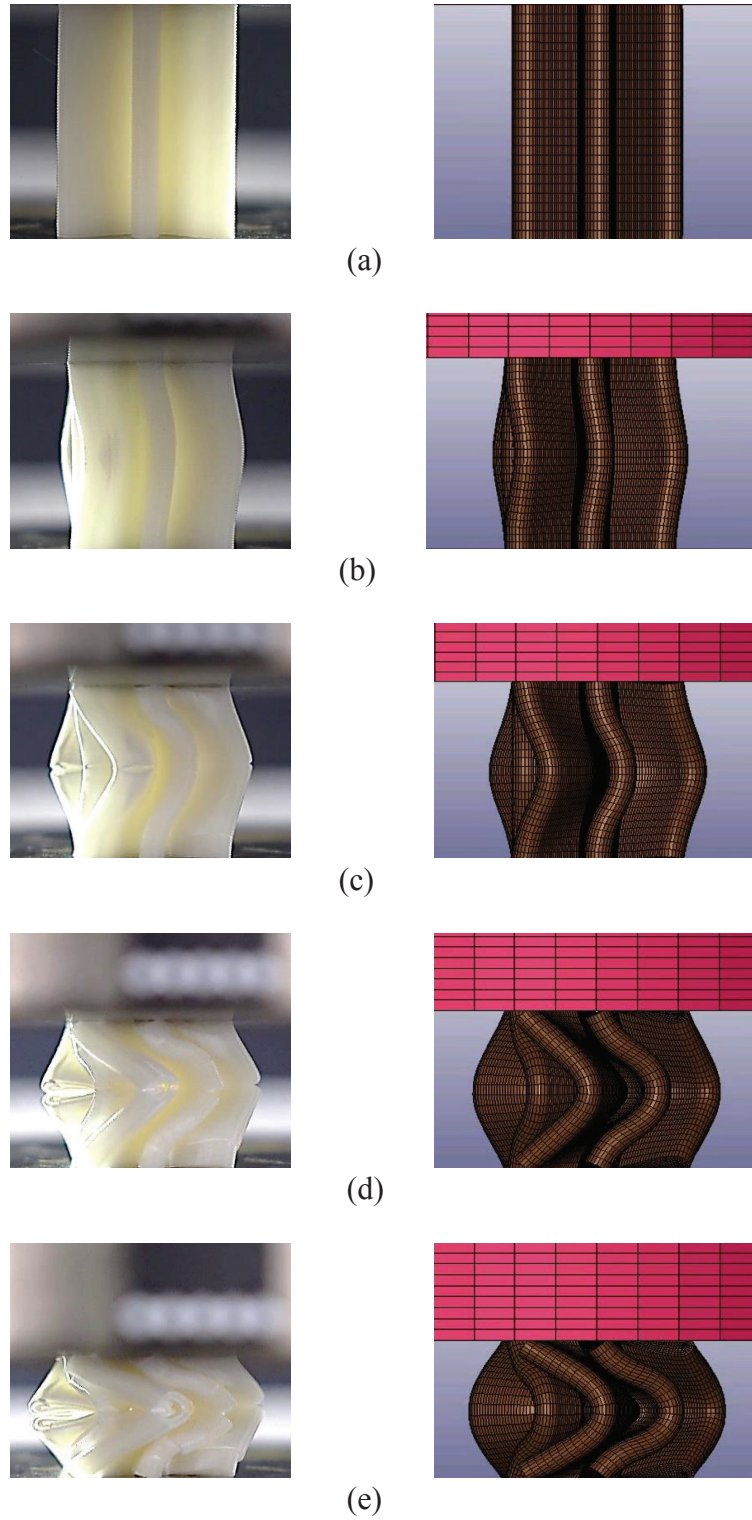
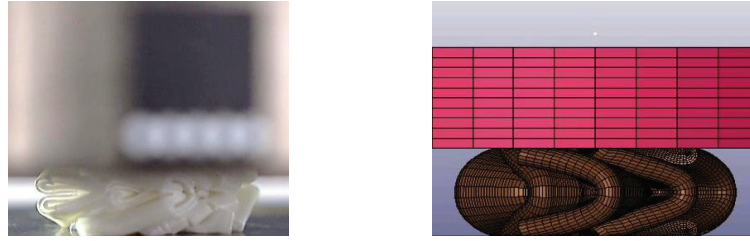


Figure 4.3. Crushing modes of cactus geometry inspired core for both numerical analysis and experimental quasi-static compression tests at deformation values of (a) 0 mm, (b) 1.25 mm, (c) 3mm, (d) 6mm, (e) 9mm, and (f)12mm

(cont. on next page)



(f)

Figure 4.3 (cont.)

It is observed that the buckling initiates on each rib of the structure, and this is reflected as the occurrence of the initial peak force point. Furthermore, the formation of a buckle-fold caused a certain instability in the same rotational direction for all of the ribs, and later leads to failure in the layers of the fold along the middle section of the structure. The failure is observed during the development of fold at a certain deformation level in the experiment. As a matter of fact, the cactus geometry was produced by adding layer by layer with the 3d printing device. It was observed that the additive manufacturing of the structure led to delamination around the weak zones by the separation of layers in the quasi-static test. On the other hand, the separation of layers could not be observed due to the suffering from the convergence problem of the implicit method in the quasi-static compression model. After the fold formation and the delamination around the middle section of the structure, the crushing force decreases until the densification region along the rest of the deformation. The major part of the deformation and energy absorption occurs in this period. The total energy absorption capacity reaches at ahead of 60% deformation level, then the densification starts at this point. At the end of the deformation, it is seen that in the middle section of the structure there is a buckle-fold formation in addition to rotation in the same direction of the ribs. An axially symmetrical deformation mode is also observed.

Subsequently, drop weight impact tests were performed with the Fractovis test machine and the crushing behavior of the core structure was investigated at moderate strain rates. The dynamic impact test having an impact velocity of 5 m/s was chosen to attain the total energy absorption capacity of the core structure. Both experimental and numerical force-displacement curves obtained from the drop weight test having the striker impact velocity of 5 m/s are given in Figure 4.4. As can be seen from Figure 4.4, the force-displacement curves obtained from experimental and numerical studies show a

notable correspondance until the buckling. However, at the following deformation period, this good correspondance was not observed in numerical and experimental. Each deformation history obtained from both the experiment and the numerical analysis also gives idea on the damage formation, Figure 4.5. It is also seen that the result obtained for the drop-weight impact test presents a force response increase till the buckling formation likewise the quasi-static test result. After this point, a jagged curve occurs due to the failure events in the local sections of the structure.

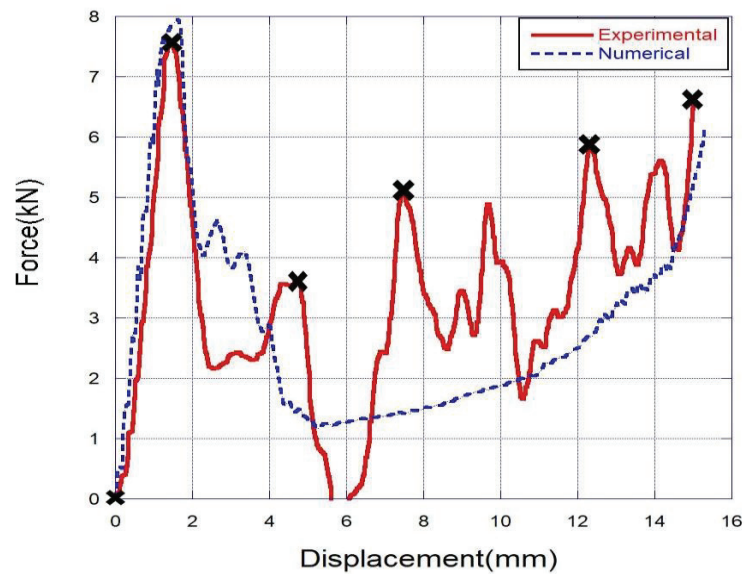


Figure 4.4. Experimental and numerical force-displacement curves of the cactus geometry inspired core at the drop weight impact test with the striker velocity of 5 m/s

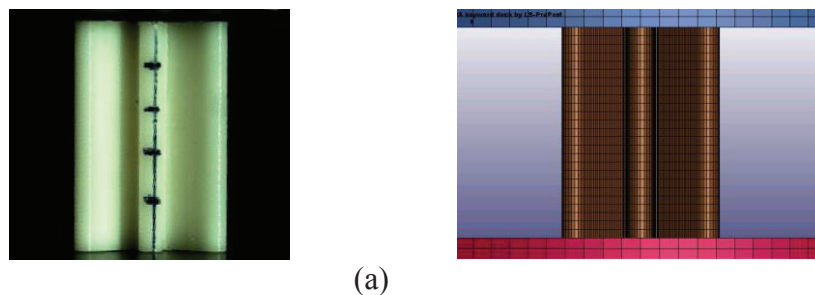
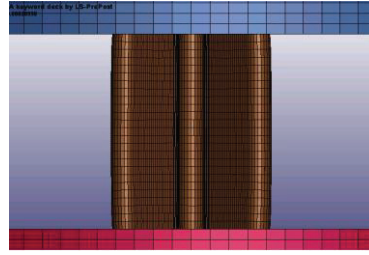
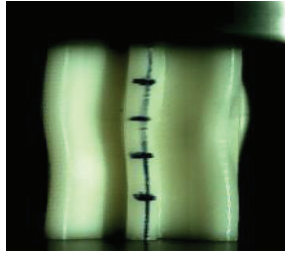
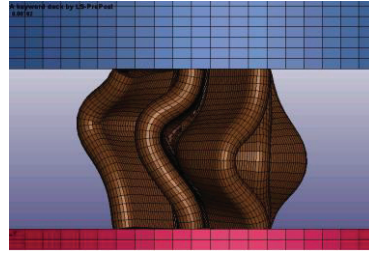
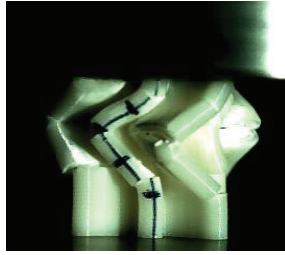


Figure 4.5. Crushing modes of cactus geometry inspired core for both numerical analysis and experimental drop-weight test at deformation values of (a) 0 mm, (b) 1.43 mm, (c) 4.74 mm, (d) 7.44mm, (e) 12.38mm, and (f) 16mm

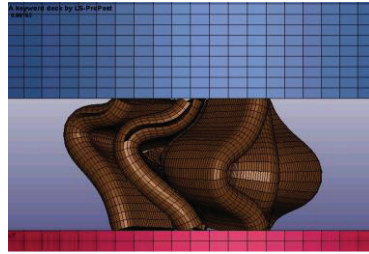
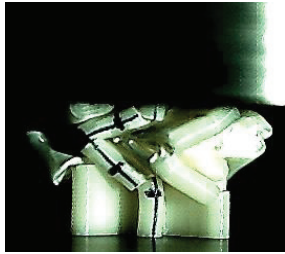
(cont. on next page)



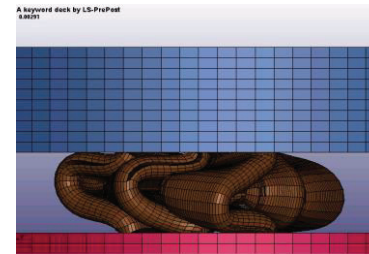
(b)



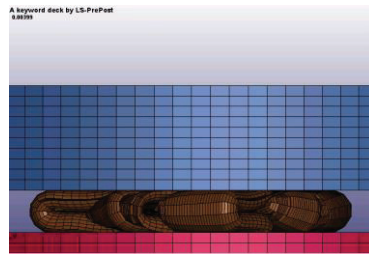
(c)



(d)



(e)



(f)

Figure 4.5 (cont.)

Direct impact tests were also carried out to examine the dynamic crushing behaviour at higher strain rates. The comparison of experimental and numerical results obtained for the direct impact test having the impact velocity of 10.71m/s is given in Figure 4.6. As can be seen from Figure 4.6, the force-displacement curves of the numerical and experimental studies are in good agreement. Each deformation history obtained from both the experiment and the numerical analysis were also given in Figure 4.7.

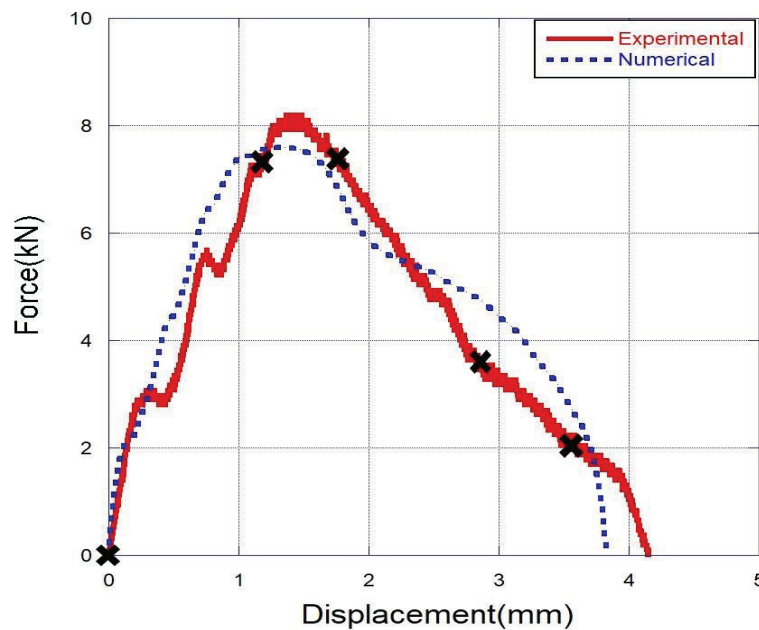
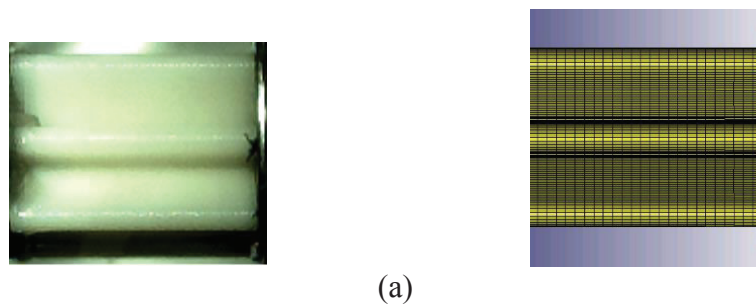


Figure 4.6. Experimental and numerical force-displacement curves of the cactus geometry core at the direct impact test with the impact velocity of 10.71 m/s



(a)

Figure 4.7. Crushing modes of cactus geometry core for both numerical analysis and experimental direct impact test at deformation values of (a) 0 mm, (b) 1.2 mm, (c) 1.75 mm, (d) 2.85 mm, (e) 3.65 mm

(cont. on next page)

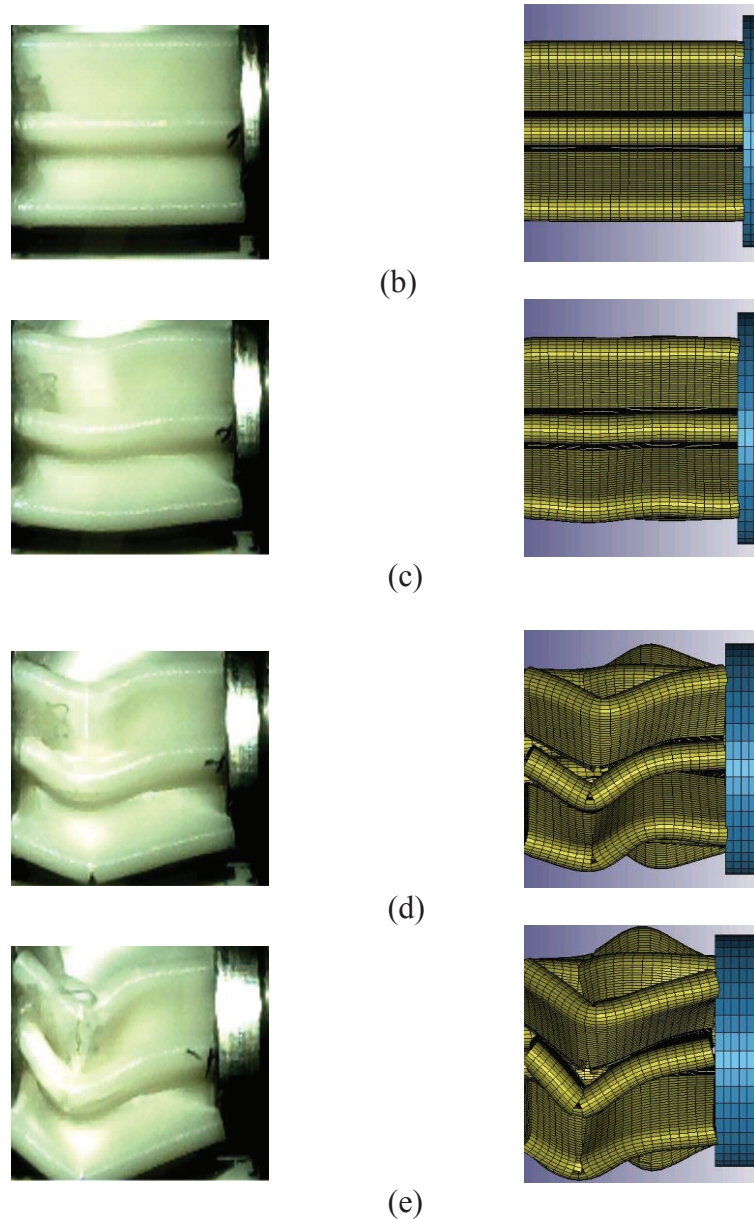


Figure 4.7 (cont.)

The summary of the test results of the cactus geometry is given in Table 4.1. In this table,  $P_i$  and  $P_{\text{mean}}$  represent the initial peak force and mean crushing force respectively. The initial peak force of the drop-weight test has a higher value than that of quasi-static. The achievement of a higher peak force in the drop weight testing led to failure events in the local sections of the structure. As a result, the force response was fluctuated at the following deformation period, and the fluctuation thus reduced the total energy absorption capacity of the drop-weight test. However, the drop-weight test is still superior to the quasi-static in terms of the total energy absorption capacity.

Table 4.1. Crashworthiness parameters of the cactus geometry inspired core under different loading conditions

Test Type	$P_i$ (kN)	$P_{mean}$ (kN)	Absorbed Energy @12 mm (J)	SAE @12 mm (kJ/kg)
Quasi-Static	5.5	2.6	34.5	17.7
Drop-Weight	7.6	3.2	36.2	18.6

## 4.2. Inertia Effect and Strain Rate Sensitivity

According to the quasi-static and dynamic tests, it was observed that the buckling formation is associated with the initial peak force response of the structure. A similar result was also obtained in another study on the collapse modes of the structural members in the literature (Hayduk and Wierzbicki 1984). Moreover, the buckling formation affects the crushing behaviour of the structure. As a result, the delay of the buckling formation with increasing strain rate is observed in Figure 4.8.

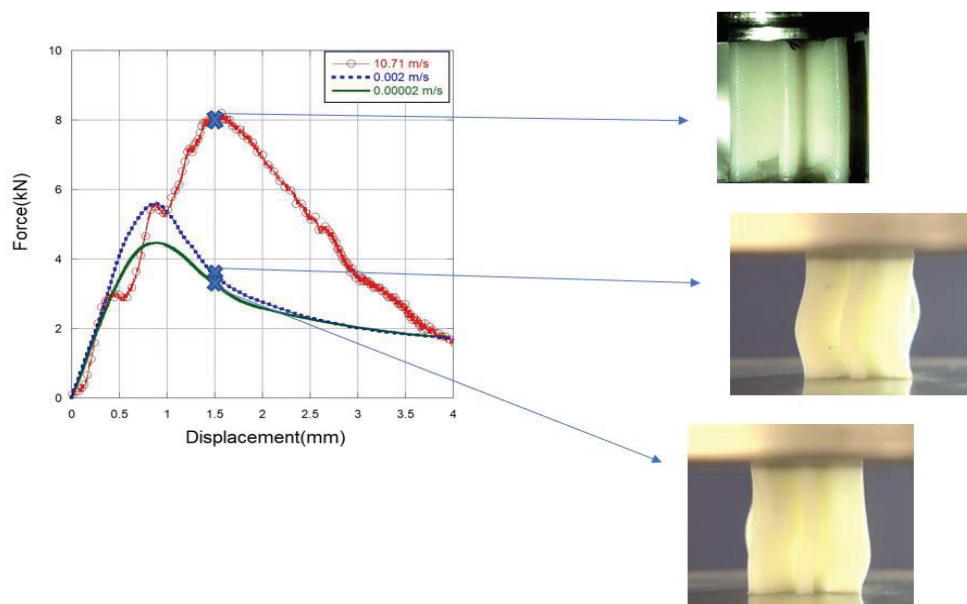


Figure 4.8. The force-displacement curves and deformation modes at certain points for direct impact and quasi-static compression tests

Numerical analyses were performed to investigate the effect of the strain rate and inertia on the crushing behaviour and the energy absorption capability of the cactus geometry. The strain rate sensitivity of the structure was investigated by comparing the models with different impact velocities, Figure 4.9.

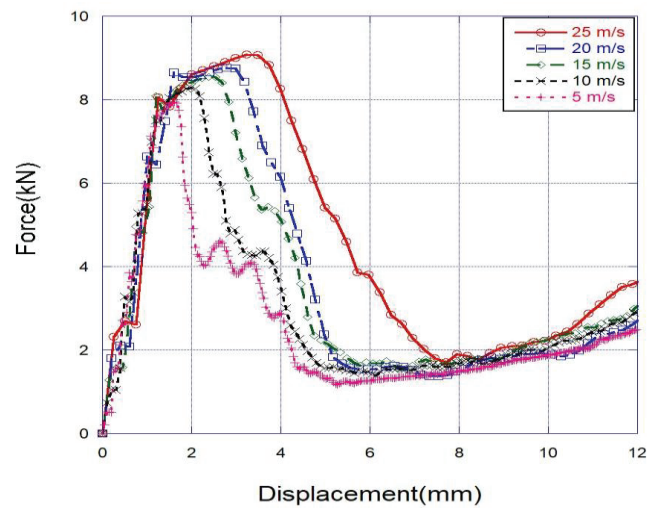


Figure 4.9. Force-displacement curves of strain rate sensitive models having different impact velocities

The energy absorption capacity increased along with the loading rate increment due to the strain rate sensitivity of the ABS polymeric material, Figure 4.10.

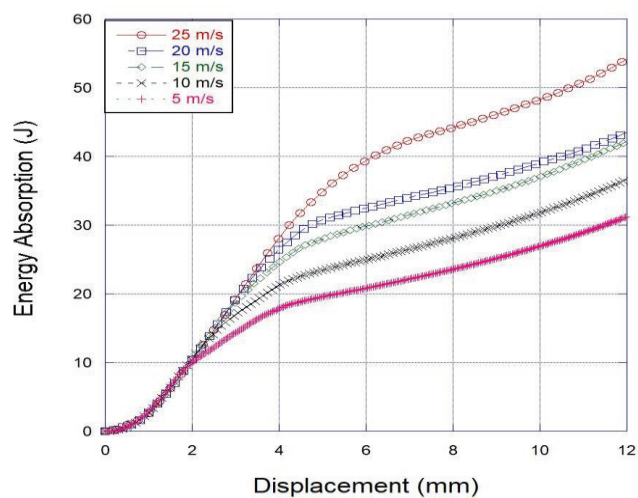


Figure 4.10. Energy absorption-displacement curves of strain rate sensitive models having different impact velocities

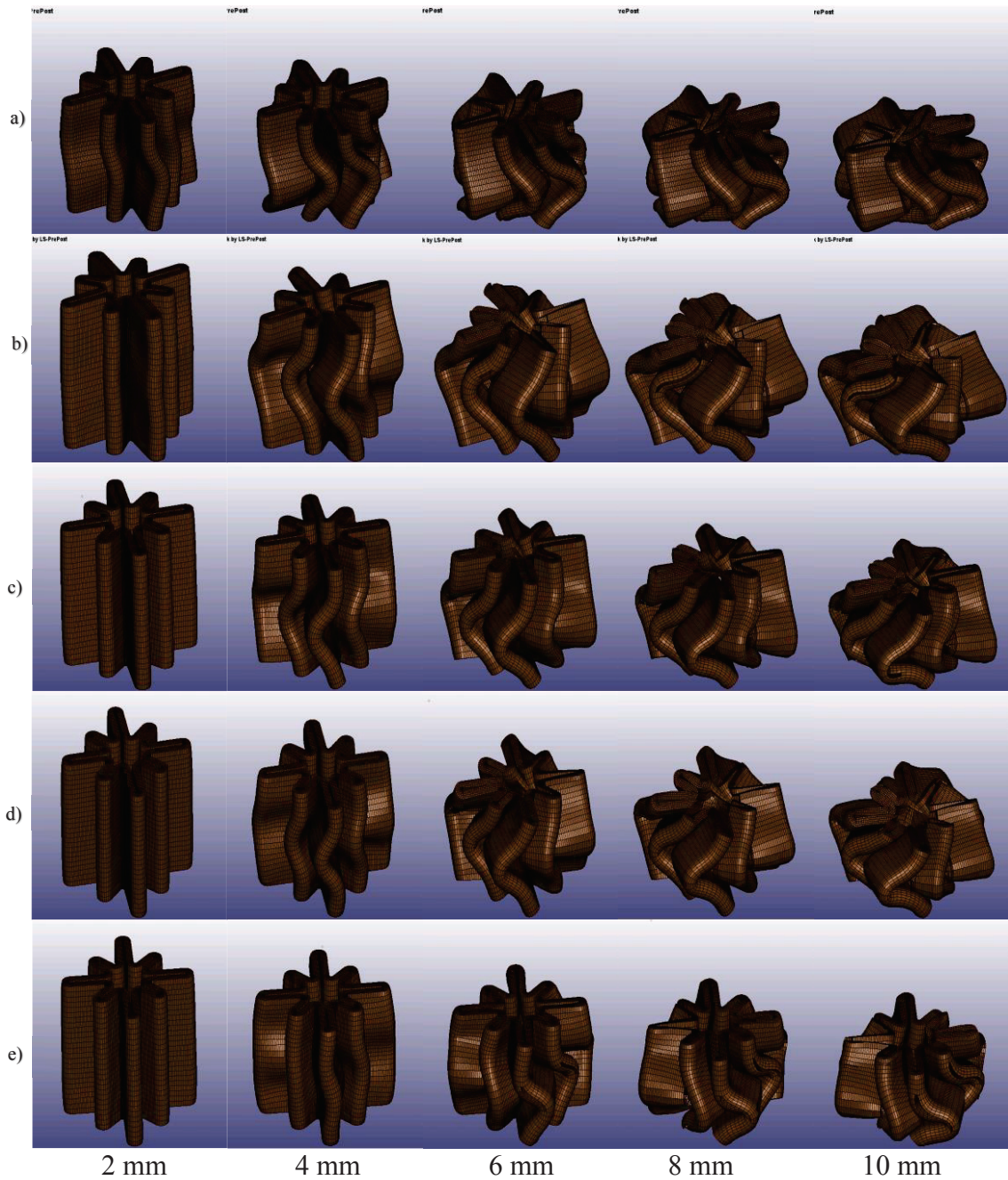


Figure 4.11. Deformation behaviour of cactus geometry inspired core subjected to different impact velocities of (a) 5 m/s, (b) 10 m/s, (c) 15 m/s, (d) 20 m/s, and (e) 25 m/s

As seen in Figure 4.11, the buckling formation of the cactus geometry corresponds to the initial peak force of the response. Therefore, the buckling formation was clearly observed on structure subjected to the impact velocity of 5 m/s at the deformation displacement of 2 mm. As a matter of fact, the initial peak force firstly occurs around the deformation displacement of 1.4 mm on the structure subjected to the impact velocity of

5 m/s. The delay of the initial peak force with the increment of the impact velocity was also observed in the test results. When all structures subjected to different impact velocities at a common displacement of 4 mm, it is observed that the earlier fold formation was prevented with increase of the initial impact velocity.

As a consequence, the energy absorption capacity of the structure increased with increasing strain rate because of the delay of the initiation stage of buckling. Deformed cores reached the energy absorption capacity at 60% deformation level are presented in Figure 4.12. Axially symmetric deformation mode was the dominant crushing behaviour of the cactus geometry for all impact velocities investigated.

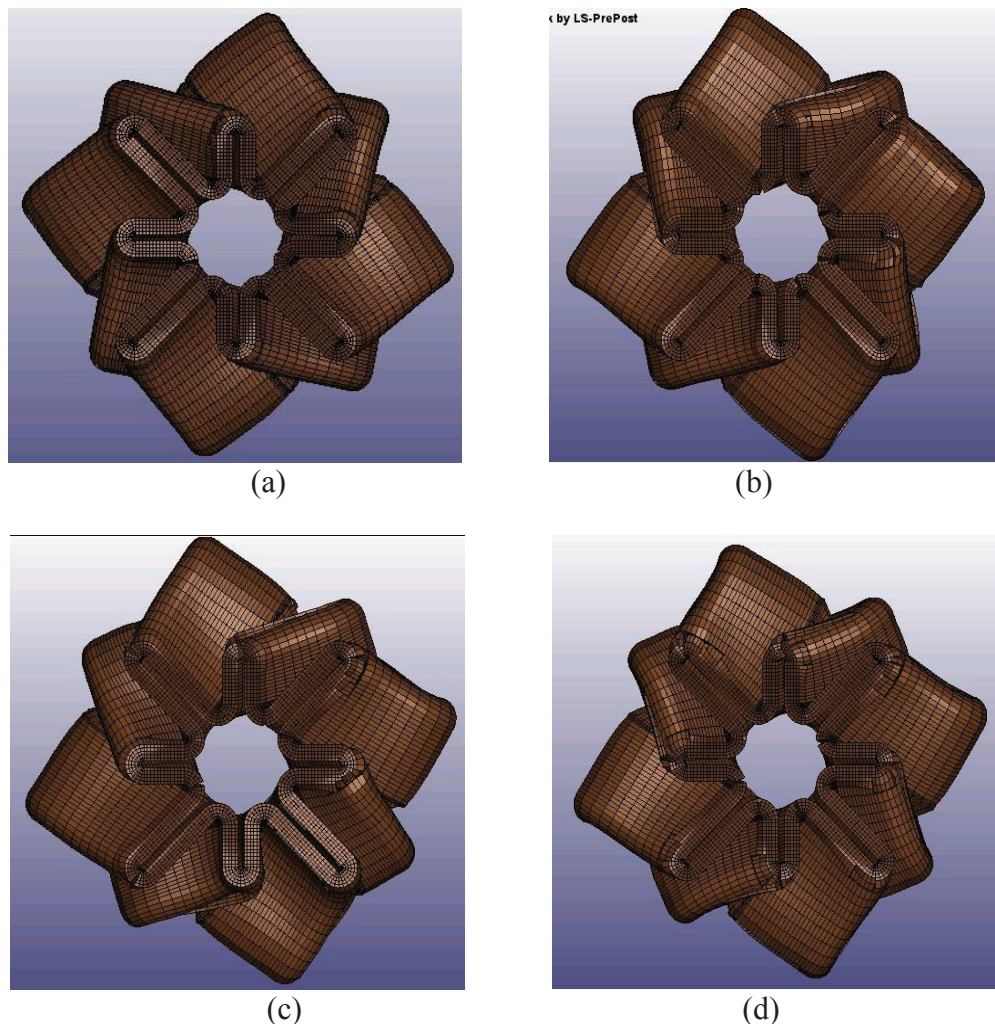
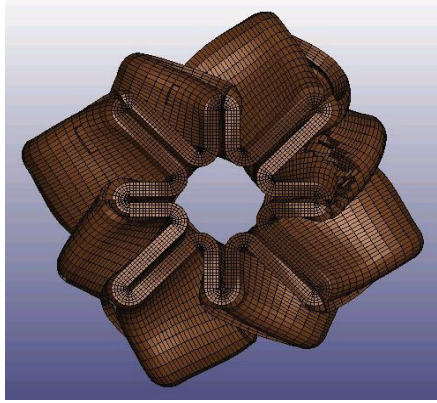


Figure 4.12. Images of numerically deformed cores under different impact velocities of (a) 5 m/s, (b) 10 m/s, (c) 15 m/s, (d) 20 m/s, (e) 25 m/s

(cont. on next page)



(e)

Figure 4.12 (cont.)

Direct impact tests were numerically modeled to understand the strain rate and inertia effects on the structure at higher strain rates. The direct impact test model was run with strain rate sensitivity parameters active and inactive. Another study on the strain rate and inertia sensitivity of combined shell structures were carried out by a similar method (Tasdemirci, Sahin, et al. 2015). Sandwich structures with these combined geometries were also studied to investigate the strain rate and inertia effect in the literature (Tasdemirci, Kara, et al. 2015). The mean crushing force (MCF)–displacement curves of both strain rate active and inactive models, and that of the quasi-static test are presented in Figure 4.13.

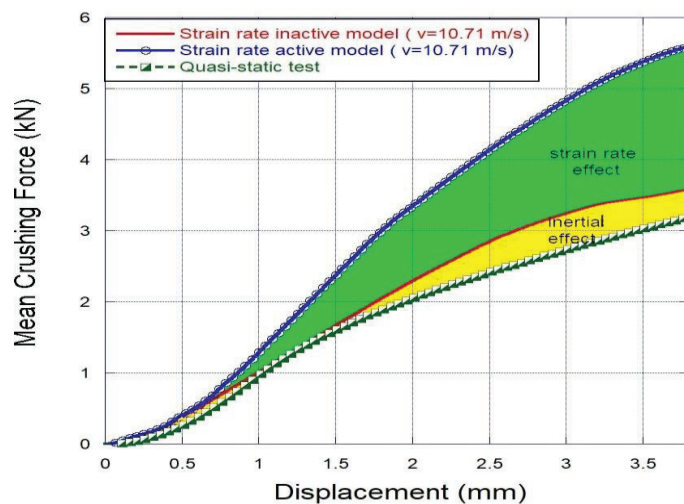


Figure 4.13. The MCF- displacement curves of strain rate active, inactive models and quasi-static test

It is clearly seen that the inertia effect corresponds to the MCF-displacement area between the strain rate inactive model and the quasi-static test. On the contrary, the strain rate effect is represented as the MCF-displacement area between the strain rate active and inactive models. The percentage change in the strain rate and the inertia effect is also plotted against the displacement in Figure 4.14.

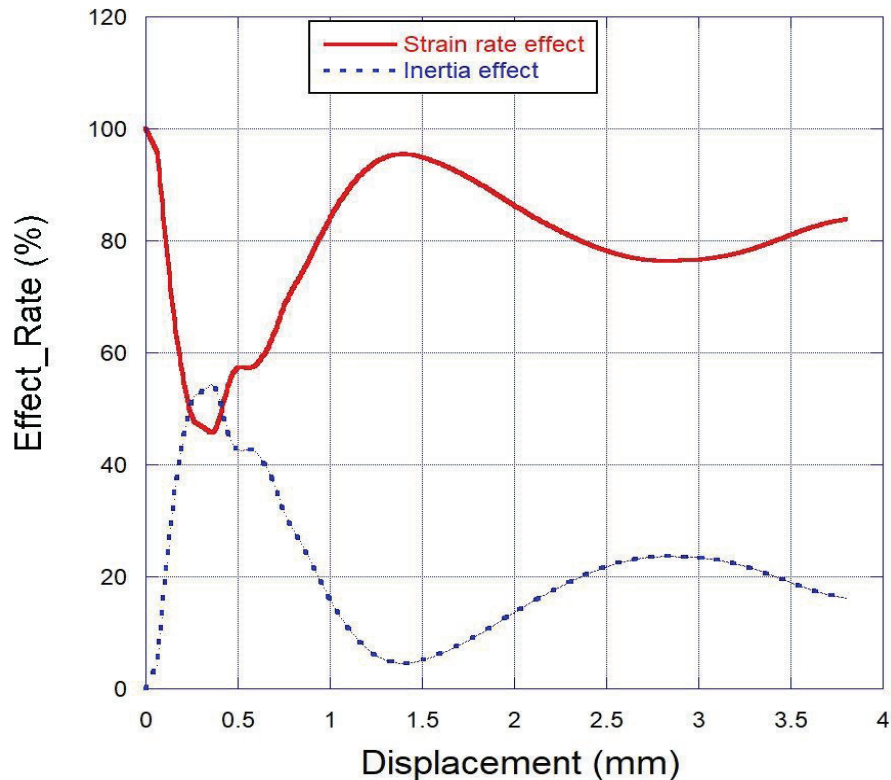


Figure 4.14. The percentage effect ratio-displacement curves of strain rate and inertia

It is understood that the inertia and strain rate have a similar effect in the initiation stage of buckling, however, after that, the strain rate effect increases up to the average ratio of 80%, and is approximately retained at the ratio of this percentage.

The different deformation modes observed based on whether Cowper-Symonds parameters are utilized or not in a direct impact model, Figure 4.15. The buckling formation is not observed at both quasi-static and dynamic strain rates until the displacement of 0.5 mm, and the inertia has a similar effect with strain rate in this stage.

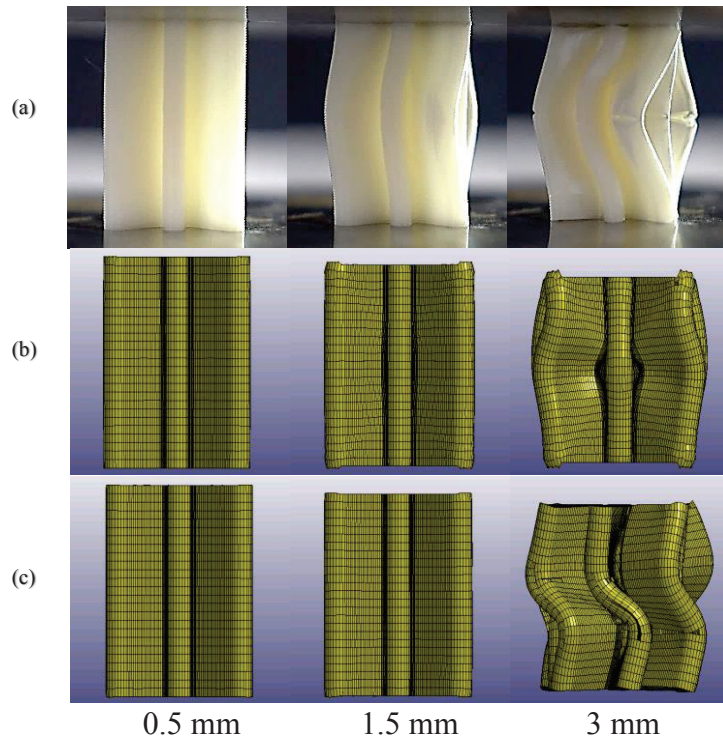


Figure 4.15. Deformation behaviour of cactus geometry inspired core subjected to (a) quasi-static compression test, (b) strain rate inactive direct impact model, and (c) strain rate active direct impact model

After this point, the strain rate active model reveals the significance of the rate-sensitivity. When the deformation is performed until the displacement of 1.5 mm, the buckling formation on the structure subjected to the quasi-static test is observed, unlike the direct impact models. It is seen that the quasi-static test and direct impact models have different deformation modes at the displacement of 3mm. The structure subjected to the quasi-static test presents a buckle-fold in the middle section of the ribs, however, the buckle-folds and local delaminations occur on two sections of the ribs for the structure of the strain rate active model. On the other hand, the asymmetric deformation is observed in the structure of the strain rate inactive model.

## CHAPTER 5

### CONCLUSIONS

In the current study, the cactus geometry was designed to present a novel alternative to conventional cross-sectioned structures (hexagon, square, cylinder and etc.) in terms of energy absorption capability. The ABS cactus structure was produced using FDM by a 3D printer. Cactus geometry was subjected to quasi-static compression and dynamic impact both experimentally and numerically in order to investigate the crushing behaviour and energy absorption. Furthermore, the strain rate and inertia effects of the structure were observed using validated numerical models in LS-DYNA software. The following conclusions were obtained based on the numerical and experimental studies:

- The cactus geometry was understood to have potential in terms of its better specific energy absorption capability due to its complex cross-section properties. ABS material is also both lightweight and cost-effective to produce structures using in research activities. Therefore, the novel structure could be easily produced with a rapid prototyping technique.
- Numerical validations were performed with LS-DYNA software. Force-displacement curves of both experiments and numerical analyses are in good agreement. However, the failure was not taken into account in implicit analysis due to the convergence problem of the model under quasi-static compression. Therefore, the separation of layers on the structure was not observed numerically. On the other hand, the crushing behaviour of the structure was similar in both experimental and numerical studies.
- The structure presented a lower initial peak force in quasi-static compression tests compared to drop-weight tests, and reached axisymmetrical crushing.
- The displacement level where first fold formation is inversely proportional to the increase of the strain rate, as it is delayed with increasing strain rate. Therefore, the total energy absorption capacity increased with the loading rate increase.

- Both strain rate and inertia effects on the crushing behaviour of the structure were investigated comparing the quasi-static test result with the numerical models of direct impact test where strain-rate parameters active and inactive. In the initiation stage of buckling, the inertia effect increased at around of %55, while the strain rate effect decreased to the ratio of %45. In the stage until the displacement of 1.5 mm, the structure of the only quasi-static test has a buckle-fold, and the strain rate effect reached the rate of %95 approximately. After, in the deformation period until the fracture occurrence, the strain rate effect decreased to the average ratio of %80 gradually. As the buckle-folds and local delaminations occurred on the structure of the strain rate active model, on the other hand, the asymmetrical deformation was observed on the structure of the strain rate inactive model.

The following recommendations were extracted from the current study for future works:

- The crushing behaviour investigation of the cactus geometry structures manufactured from the metal or composite material using additive manufacturing techniques can be more effective for the defense and automobile industry.
- Crushing behaviour and energy absorption of the tapered manufactured cactus geometry with or without the oblique loading method can be also examined to compare with the current study.
- The effect on the energy absorption efficiency of using fillers, confinements and triggers might be studied for this structure.
- With dynamic blast loading tests, the strain rate and inertia effect on the sandwich structures, prepared by using cactus geometry inspired cores, might be researched to comprehend much better these parameters.

## REFERENCES

- Appelsved, Peter. 2012. "Investigation of Mechanical Properties of Thermoplastics with Implementations of LS-DYNA Material Models." Independent thesis Advanced level (degree of Master (One Year)) Student thesis.
- Aziz, Moheb Sabry, and Amr Y. El sherif. 2016. "Biomimicry as an approach for bio-inspired structure with the aid of computation." *Alexandria Engineering Journal* 55 (1):707-714. doi: <https://doi.org/10.1016/j.aej.2015.10.015>.
- Baroutaji, Ahmad, Mustafa Sajjia, and Abdul-Ghani Olabi. 2017. "On the crashworthiness performance of thin-walled energy absorbers: Recent advances and future developments." *Thin-Walled Structures* 118:137-163. doi: <https://doi.org/10.1016/j.tws.2017.05.018>.
- Bates, Simon R. G., Ian R. Farrow, and Richard S. Trask. 2016. "3D printed polyurethane honeycombs for repeated tailored energy absorption." *Materials & Design* 112:172-183. doi: <https://doi.org/10.1016/j.matdes.2016.08.062>.
- Bosch, Kelly, Katrina Harris, David Clark, Risa Scherer, and Joseph Melotik. 2015. *Blast Mitigation Seat Analysis: Assessment of the Effect of Personal Protective Equipment on the 5 th Percentile Female Anthropomorphic Test Device Performance in Drop Tower Evaluations*.
- Calladine, C. R., and R. W. English. 1984. "Strain-rate and inertia effects in the collapse of two types of energy-absorbing structure." *International Journal of Mechanical Sciences* 26 (11):689-701. doi: [https://doi.org/10.1016/0020-7403\(84\)90021-3](https://doi.org/10.1016/0020-7403(84)90021-3).
- Chen, Liming, Jian Zhang, Bing Du, Hao Zhou, Houchang Liu, Yongguang Guo, Weiguo Li, and Daining Fang. 2018. "Dynamic crushing behavior and energy absorption of graded lattice cylindrical structure under axial impact load." *Thin-Walled Structures* 127:333-343. doi: <https://doi.org/10.1016/j.tws.2017.10.048>.
- Chen, Yanyu, Tiantian Li, Zian Jia, Fabrizio Scarpa, Chun-Wei Yao, and Lifeng Wang. 2018. "3D printed hierarchical honeycombs with shape integrity under large compressive deformations." *Materials & Design* 137:226-234. doi: <https://doi.org/10.1016/j.matdes.2017.10.028>.
- Cheng, Ming, Jean-Philippe Dionne, and Aris Makris. 2010. "On drop-tower test methodology for blast mitigation seat evaluation." *International Journal of*

*Impact Engineering - INT J IMPACT ENG* 37:1180-1187. doi: 10.1016/j.ijimpeng.2010.08.002.

- Dominguez-Rodriguez, G., J. J. Ku-Herrera, and A. Hernandez-Perez. 2018. "An assessment of the effect of printing orientation, density, and filler pattern on the compressive performance of 3D printed ABS structures by fuse deposition." *International Journal of Advanced Manufacturing Technology* 95 (5-8):1685-1695. doi: 10.1007/s00170-017-1314-x.
- Erdik, Atil. 2019. "Investigation of dynamic response of a mannequin in a vehicle exposed to land mine blast." 23:382-389. doi: 10.16984/saufenbilder.440643.
- Fadeel, Abdalsalam, Ahsan Mian, Mohammed Al Rifaie, and Raghavan Srinivasan. 2019. "Effect of Vertical Strut Arrangements on Compression Characteristics of 3D Printed Polymer Lattice Structures: Experimental and Computational Study." *Journal of Materials Engineering and Performance* 28 (2):709-716. doi: 10.1007/s11665-018-3810-z.
- Garcia, Justine, ZhiLin Yang, Rosaire Mongrain, Richard L Leask, and Kevin Lachapelle. 2018. "3D printing materials and their use in medical education: a review of current technology and trends for the future." *BMJ Simulation and Technology Enhanced Learning* 4 (1):27-40. doi: 10.1136/bmjstel-2017-000234.
- Ha, Ngoc San, Guoxing Lu, and Xinmei Xiang. 2019. "Energy absorption of a bio-inspired honeycomb sandwich panel." *Journal of Materials Science* 54 (8):6286-6300. doi: 10.1007/s10853-018-3163-x.
- Hallquist, John O. 2006. "LS-DYNA theory manual." *Livermore software Technology corporation* 3:25-31.
- Hayduk, Robert J, and Tomasz Wierzbicki. 1984. "Extensional collapse modes of structural members." *Computers & structures* 18 (3):447-458.
- Heimbs, Sebastian, Sebastian Schmeer, Peter Middendorf, and Martin Maier. 2007. "Strain rate effects in phenolic composites and phenolic-impregnated honeycomb structures." *Composites Science and Technology* 67 (13):2827-2837.
- International, ASTM. 2015. *ASTM D638-14, Standard Test Method for Tensile Properties of Plastics*: ASTM International.

- Karagiozova, D., G. S. Langdon, and G. N. Nurick. 2010. "Blast attenuation in Cymat foam core sacrificial claddings." *International Journal of Mechanical Sciences* 52 (5):758-776. doi: <https://doi.org/10.1016/j.ijmecsci.2010.02.002>.
- Krzystała, Edyta, Arkadiusz Mężyk, and Sławomir Kciuk. 2016. "Minimisation of the explosion shock wave load onto the occupants inside the vehicle during trinitrotoluene charge blast." *International Journal of Injury Control and Safety Promotion* 23 (2):170-178. doi: 10.1080/17457300.2014.966118.
- Kucewicz, Michał, Paweł Baranowski, Jerzy Małachowski, Arkadiusz Popławski, and Paweł Płatek. 2018. "Modelling, and characterization of 3D printed cellular structures." *Materials & Design* 142:177-189. doi: <https://doi.org/10.1016/j.matdes.2018.01.028>.
- Lee, Woei-shyan, and Huang-Long Lin. 2003. "The Strain Rate Dependence of Deformation and Fracture Behaviour of Acrylonitrile-Butadiene-Styrene (Abs) Copolymer in Impact Test." In *European Structural Integrity Society*, edited by B. R. K. Blackman, A. Pavan and J. G. Williams, 231-240. Elsevier.
- Li, Zhejian, Wensu Chen, and Hong Hao. 2018. "Blast mitigation performance of cladding using square dome-shape kirigami folded structure as core." *International Journal of Mechanical Sciences* 145:83-95. doi: <https://doi.org/10.1016/j.ijmecsci.2018.06.035>.
- LSTC. 2007. LS-DYNA keyword user's manual. Livermore Software Technology Corporation Livermore, CA.
- Marangoni, Alexandre Luis, and Ernesto Massaroppi Junior. 2017. "Cowper-Symonds parameters estimation for ABS material using design of experiments with finite element simulation." *Polímeros* 27:220-224.
- Owolabi, Gbadebo, Alex Peterson, Ed Habtour, Jaret Riddick, Michael Coatney, Adewale Olasumboye, and Denzell Bolling. 2016. "Dynamic response of acrylonitrile butadiene styrene under impact loading." *International Journal of Mechanical and Materials Engineering* 11 (1):3. doi: 10.1186/s40712-016-0056-0.
- Popescu, Diana, Aurelian Zapciu, Catalin Amza, Florin Baci, and Rodica Marinescu. 2018. "FDM process parameters influence over the mechanical properties of polymer specimens: A review." *Polymer Testing* 69:157-166. doi: <https://doi.org/10.1016/j.polymertesting.2018.05.020>.

- Rebelo, H. B., D. Lecompte, C. Cismasiu, A. Jonet, B. Belkassem, and A. Maazoun. 2019. "Experimental and numerical investigation on 3D printed PLA sacrificial honeycomb cladding." *International Journal of Impact Engineering* 131:162-173. doi: <https://doi.org/10.1016/j.ijimpeng.2019.05.013>.
- Reithofer, Peter, and Artur Fertschej. 2016. "Failure models for thermoplastics in LSDYNA." *AIP Conference Proceedings* 1779 (1):050009. doi: 10.1063/1.4965514.
- Roth, René Romain. 1983. "The foundation of bionics." *Perspectives in biology and medicine* 26 (2):229-242.
- Rutkowski, Joseph V., and Barbara C. Levin. 1986. "Acrylonitrile–butadiene–styrene copolymers (ABS): Pyrolysis and combustion products and their toxicity—a review of the literature." *Fire and Materials* 10 (3-4):93-105. doi: 10.1002/fam.810100303.
- Sarvestani, H. Y., A. H. Akbarzadeh, H. Niknam, and K. Hermenean. 2018. "3D printed architected polymeric sandwich panels: Energy absorption and structural performance." *Composite Structures* 200:886-909. doi: 10.1016/j.compstruct.2018.04.002.
- Scarpa, F, S Blain, T Lew, D Perrott, M Ruzzene, and JR Yates. 2007. "Elastic buckling of hexagonal chiral cell honeycombs." *Composites Part A: Applied Science and Manufacturing* 38 (2):280-289.
- Schmitt, Otto H. 1969. "Some interesting and useful biomimetic transforms." Third Int. Biophysics Congress.
- Tabacu, Stefan, and Cătălin Ducu. 2018. "Experimental testing and numerical analysis of FDM multi-cell inserts and hybrid structures." *Thin-Walled Structures* 129:197-212. doi: <https://doi.org/10.1016/j.tws.2018.04.009>.
- Tasdemirci, Alper, Ali Kara, Kivanc Turan, and Selim Sahin. 2015. "Dynamic crushing and energy absorption of sandwich structures with combined geometry shell cores." *Thin-Walled Structures* 91:116-128. doi: <https://doi.org/10.1016/j.tws.2015.02.015>.
- Tasdemirci, Alper, Selim Sahin, Ali Kara, and Kivanc Turan. 2015. "Crushing and energy absorption characteristics of combined geometry shells at quasi-static and dynamic strain rates: Experimental and numerical study." *Thin-Walled Structures* 86:83-93. doi: <https://doi.org/10.1016/j.tws.2014.09.020>.

- Tsouknidas, A., M. Pantazopoulos, I. Katsoulis, D. Fasnakis, S. Maropoulos, and N. Michailidis. 2016. "Impact absorption capacity of 3D-printed components fabricated by fused deposition modelling." *Materials & Design* 102:41-44. doi: <https://doi.org/10.1016/j.matdes.2016.03.154>.
- Vairis, A., M. Petousis, N. Vidakis, and K. Savvakis. 2016. "On the Strain Rate Sensitivity of Abs and Abs Plus Fused Deposition Modeling Parts." *Journal of Materials Engineering and Performance* 25 (9):3558-3565. doi: [10.1007/s11665-016-2198-x](https://doi.org/10.1007/s11665-016-2198-x).
- Van Paepegem, W., S. Palanivelu, J. Degrieck, J. Vantomme, B. Reymen, D. Kakogiannis, D. Van Hemelrijck, and J. Wastiels. 2014. "Blast performance of a sacrificial cladding with composite tubes for protection of civil engineering structures." *Composites Part B: Engineering* 65:131-146. doi: <https://doi.org/10.1016/j.compositesb.2014.02.004>.
- Vincent, Julian F. V., Olga A. Bogatyreva, Nikolaj R. Bogatyrev, Adrian Bowyer, and Anja-Karina Pahl. 2006. "Biomimetics: its practice and theory." *Journal of the Royal Society, Interface* 3 (9):471-482. doi: [10.1098/rsif.2006.0127](https://doi.org/10.1098/rsif.2006.0127).
- Walley, SM, and JE Field. 1994. "Strain rate sensitivity of polymers in compression from low to high rates." *DYMAT j* 1 (3):211-227.
- Wu, Zhenyu, Maolin Wang, Zhiping Ying, Xiaoying Cheng, and Xudong Hu. 2019. "Influence of fabric architecture on crushing behavior of semi-hexagonal composite structures under axial loading." *Journal of Industrial Textiles* 49 (2):162-180.
- Xiang, Jinwu, and Jianxun Du. 2017. "Energy absorption characteristics of bio-inspired honeycomb structure under axial impact loading." *Materials Science and Engineering: A* 696:283-289. doi: <https://doi.org/10.1016/j.msea.2017.04.044>.
- Xu, Ming-ming, Guang-yan Huang, Shun-shan Feng, Graham McShane, and William Stronge. 2016. "Static and dynamic properties of semi-crystalline polyethylene." *Polymers* 8 (4):77.
- Zhang, Linwei, Zhonghao Bai, and Fanghua Bai. 2018. "Crashworthiness design for bio-inspired multi-cell tubes with quadrilateral, hexagonal and octagonal sections." *Thin-Walled Structures* 122:42-51. doi: <https://doi.org/10.1016/j.tws.2017.10.010>.
- Zhang, Yong, Minghao Lu, Chun H. Wang, Guangyong Sun, and Guangyao Li. 2016. "Out-of-plane crashworthiness of bio-inspired self-similar regular hierarchical

honeycombs." *Composite Structures* 144:1-13. doi:  
<https://doi.org/10.1016/j.compstruct.2016.02.014>.

Zhao, Xuan, Guohua Zhu, Chenyu Zhou, and Qiang Yu. 2019. "Crashworthiness analysis and design of composite tapered tubes under multiple load cases." *Composite Structures* 222:110920.